ABSTRACT

Title of Document: THE DYNAMIC BEHAVIOR OF POLYUREA COMPOSITES SUBJECTED TO HIGH STRAIN RATE LOADING

Mohammad Maqsud Ali
Doctor of Philosophy, 2018

Directed By: Professor Amr Baz
Department of Mechanical Engineering
University of Maryland, College Park

A comprehensive theoretical and experimental study of the characterization of Polyurea composites subjected to high strain impact loading are conducted. The composites under consideration consist of multi-layers of polyurea/aluminum arranged in one dimension configuration. Finite element models (*FEM*) are developed by describing the dynamics of the viscoelastic behavior of the polyurea using the Golla-Hughes-Mctavish (*GHM*) mini-oscillator approach. The model enables the predictions of the structural stress, strain, strain rate, relaxation modulus, loss factor of the polyurea composites for different layering arrangements. The predictions of the developed *FEM* are validated against the predictions of the commercial finite element package *ANSYS*. Also, the *FEM* predictions are validated experimentally using the Split Hopkinson Pressure Bar (*SHPB*) which is used to monitor the dynamics of the polyurea composites at different levels of strain rates. Close agreements are demonstrated between the theoretical predictions and the obtained experimental results. Bloch wave propagation

theory is used to develop an analytical model based on transfer matrix method to identify attenuation band gaps in dynamical response of periodically placed polyurea composites. The influence of various design parameters that controls the width of pass and stop-bands including multi layered periodic structures and different material configurations is compared.

The presented theoretical and experimental approaches are envisioned to provide invaluable tools for the design of polyurea composites that can be used in impact mitigation and protection of critical structures subjected to high impact and blast loading.

Keywords: Polyurea composites, dynamics under high strain loading, finite element modeling, Golla-Huges-Mctavish (*GHM*) mini-oscillators, Split Hopkinson Pressure Bar (*SHPB*), periodic structures, Bloch wave propagation theory, band gaps, transfer matrix, dispersion curves, propagation factor.

THE DYNAMIC BEHAVIOR OF POLYUREA COMPOSITES SUBJECTED TO HIGH STRAIN RATE LOADING

By

Mohammad Maqsud Ali

Dissertation submitted to the Faculty of the Graduate School of the
University of Maryland, College Park, in partial fulfillment
of the requirements for the degree of
Doctor of Philosophy
2018

Advisory Committee:
Professor Amr Baz, Chair
Professor Balakumar Balachandran
Professor Miao Yu
Assistant Professor Jin-Oh Hahn
Associate Professor Christopher Cadou (Dean's Representative)

Dedication

This work has been dedicated to the most important people in my life for their continuous inspiration, patience and support.

My Mother, *Kulsum Ali*

My Father, *Mansur Ali*

My Wife, *Lubna Maryam*

My Loving Daughters,

Zahraa,

Zainab,

Fatimah,

My Sister, *Sanjida* and Br in-law *Hadi*

My Niece *Shaila* and Nephew *Sabbir*

Acknowledgements

All Praises belong to ALLAH (SWT), The most Merciful, the most Beneficent, the most Knowledgeable, who has guided us through the ways of last Prophet Mohammad (saw) to enable me to accomplish this task.

I would like to specially thank my guide, mentor and academic advisor Professor Amr Baz, for his continuous support and guidance. This work would not have been possible without his encouragement and sincere support. Prof. Baz continuously motivated and mentored me like a father figure all these years to work hard and complete the thesis.

I would also like to thank my committee members Dr. Balakumar Balachandran, Dr. Miao Yu, Dr. Jin-Oh Hahn, and Dr. Christopher Cadou to serve as my committee members with valuable inputs during my defense. I would like to specially thank my colleagues, Yaser Al-Saffar, Yaqoub Abdullah and Muhammad Raafat for providing me support on different occasions.

Finally, and most importantly, I would like to express my gratitude to my wife Lubna. It would have been impossible for me to finish this work without her patience, encouragement and continuous support. I sincerely thank my parents whose kindness, prayers and never-ending love have been a lifetime blessing for me.

With daily Prayers and gaining Knowledge along with the Remembrance of Allah (swt), I show Gratitude to the Sustainer of the Universe, Allah (swt) for showing me the value of Serving the Humanity with Sincerity and to Propagate His Infinite Mercy and Blessings to the mankind.

Table of Contents

List of Figures

Chapter 1

INTRODUCTION

1.1 Motivation

Polyurea elastomer generally used for protective coating purpose due to its advantages such as good damping quality, fast cure time and blast resistance properties. Polyurea provides corrosion and extreme abrasion resistance. Polyurea has proven to be a fast and efficient solution for hole and patch repairs on steel. It has a Fire Class A Rating, which means that when a continuous flame is on this material, it emits no toxic gases and will not drip when burned. And, once the source of the flame is removed, the material ceases to burn. In addition, when cured, it will not leach gases, so it is ideal for coating potable water tanks. It even provides *UV* protection. Because of its enormous elasticity and abrasion resistance, it stands up to rugged treatment. It is especially suitable in harsh environments and under extreme climates, where other materials fail. Its elastic nature also provides a shock-absorbing benefit.

Polyurea has excellent mechanical properties including tensile strength, tear strength and elongation which make it very tough. Thus, its application has been extensively used to retrofit in aerospace and automotive industries, dynamic structural loading during earth quakes, high rate manufacturing process, cavitation erosion in tubing and marine propulsion, defense applications including projectile/armor, absorbing energy during structural crash and holding metal/brick fragments even after failure.

Mechanical properties of Polyurea are strongly rate dependent under high loading conditions due to its very high viscosity which makes it suitable for these applications. Polyurea

has high toughness-to-density and very good chemical resistance. This is the main reason of our motivation of the current research.

1.2 Split-Hopkinson pressure bar (*SHPB*)

Material properties such as yield stress and ultimate strength are generally obtained under quasi-static loading conditions using common testing methods. Mechanical responses of materials, their reliability, and to quantify their sensitivity under impact conditions largely depend on mechanical characterization to enhance the energy absorption and dynamic performance. Particularly, applications like shock absorbing criteria, materials especially elastomers must be characterized for large strains and over a wide range of strain rates.

Over the last five decades, Split-Hopkinson pressure bar (*SHPB*) technique has been widely used for dynamic material characterization of high strain-rate properties of many common engineering materials. One of the many benefits of employing this simple technique is that no prior knowledge of material behavior is needed as a small sample is used to establish a uniform stress and strain state in the specimen and thus avoiding detailed analysis of wave propagation.

Since soft materials possess low mechanical impedances which will increase delays in attaining dynamic equilibrium resulting transmission pulses with extremely low signal-to-noise ratios.

1.3 Literature Review

1.3.1 Split Hopkinson Pressure Bar (*SHPB*) tests: History and advancement

Split Hopkinson Pressure Bar (*SHPB*) is the most prominent techniques of analyzing mechanical properties and behavior of different materials undergoing impact loading.

In 1914, Bertram Hopkinson [1] formulated analytical expressions for the total increase in length of an impulsively loaded wire which is fixed at one end and introduced a pressure measuring method produced by a bullet like blow, thus originated the pressure bar technique after his father John Hopkinson (1872) introduced the Hopkinson bar technique while doing stress wave experiments in iron wires.

In 1923, Landon and Quinney [2] included the various effects of length, diameter and materials of the bars on the pressure wave.

Dennison Bancroft (1941) showed that velocity of longitudinal waves in cylindrical bars may be expressed as the velocity at infinite wave-length times a function of Poisson's ratio, and the ratio of the diameter of the bar to the wave-length. Velocities at very short wave-lengths were deduced and displacement variations were found as a function of the diameter. The value of Bancroft's work applied towards Hopkinson bar testing was only realized much later when computers became integral tools for fast data processing.

In 1948, Davies [3] modified the Hopkinson's technique and introduced an electrical method to find correlation between applied pressure and time involving experiments on high

pressures of short duration. He used the longitudinal displacement created by the applied pressure to change in the capacity of a condenser which is charged to a high potential and connected through a feed circuit and an amplifier to a double-beam cathode-ray oscillograph. A vertical deflection occurs with the change in capacity of the condenser while the other beam is being used for time-marking. The condenser output is proportional to strain-time relations which in turn proportional to the pressure-time relations, and thus made significant improvement in the certainties of the pressure histories through continuous record of very small displacement of the free end of the bar as introduced by Hopkinson's original method.

The name Split Hopkinson Bar was introduced by Kolsky [4] in 1949 who introduced a second pressure bar by modifying Davies's work. Detonators were used to produce large transient stresses while the specimen was sandwiched between these two parallel pressure bars. Strain histories were measured by introducing a second condenser microphone to calculate specimen properties. Different lubricants were also used to eliminate large friction effects errors and thus had fairly uniform permanent deformations to measure stress-strain behavior of materials of the order of 20 micro seconds. Kolsky tested five different material behaviors (polythene, rubber, *PMMA*, copper, and lead) with four different thickness (0.025 cm, 0.048 cm, 0.086 cm, and 0.768 cm, respectively) and produced stress-strain curves in Figure 1.1. Due to most vulnerable to dispersion effects, Kolsky omitted first two or three points on each curve. Kolsky bar technique has become the most widely used testing procedure for hard, soft and viscoelastic materials since then.

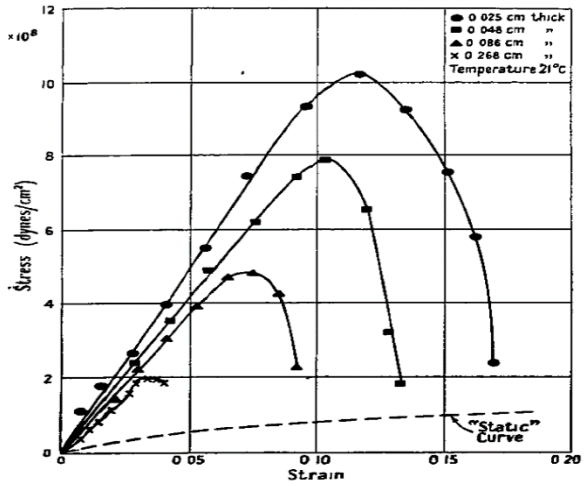

Figure 1.1: Dynamic Stress-Stain curves for ploythene (Kolsky, 1949)

In 1970, Dharan and Hauser [5], modified the approach proposed of Kolsky by discarding the input bar to allow impact to occur in specimen directly and thus achieving high stresses to get dynamic plastic properties at strain rates as high as $10^5\ sec^{-1}$. He was the first one to use the strain gauges to measure displacements.

In 2004, Gama *et al.* [6] in a critical review summarized a step by-step methodology of recent developments the Research, experimental design criteria and data analysis of a valid *SHPB* test. Summary of the critical review are as follows:

According to Kolsky, the main 1D assumptions of Hopkinson Bar technique are: *i*) the wave propagation in the bars is free of dispersion, *ii*) the effect of interface friction and inertia of the specimen is negligible, *iii*) the stress wave reverberation in the specimen is negligible, *iv*) the stress equilibrium in the specimen is achieved in π travel/characteristic time, and *v*) the specimen-bar interfaces remain planar at all time.

Finite diameter bars are prone to dispersion effects which makes assumption (*i*) not valid. However, methodologies following the solution of the Pochhammer [7] frequency equation are available to correct this problem.

Assumptions (*ii*) and (*iii*) are not sufficient conditions for displacement and stress continuities in those interfaces to be valid and higher order analysis, considering the displacement and stress continuity conditions at the bar specimen interfaces are identified to be a possible area to compensate for.

From 1D stress wave propagation theory, the dynamic deformation of specimens under *SHPB* loading conditions occurs under a non-equilibrium state of stress that makes assumption (*iv*) not generally correct. The stress non-equilibrium issues can be addressed by plotting stress-strain rate instead of stress-strain, and time averaging the non- equilibrium stress and strain rate data using a time window not less than one characteristic time of the specimen.

Assumption (*iv*) is technically valid for soft specimens but these specimens have an inherent problem of poor transmission, which is generally addressed by the use of low-impedance bars or hollow transmission bars.

In light of the validity of 1D Hopkinson bar assumptions, a step-by-step methodology of the Hopkinson Bar experiment is outlined. These steps are *a*) the calibration of the bars, *b*) the specimen design, *c*) the Hopkinson bar experiment, *d*) the dispersion correction, and e) the data representation.

1.3.2 Current areas of Research: Effects of Geometry, Inertia, and Dimension

In addition to the introduction of different experimental techniques, researchers have also put much effort on understanding the effects of specimen dimensions and geometry as well as wave propagation.

In the past, there had been no standardized test specimens with differing dimensions and geometry so to make it difficult for other researchers to compare results of different tests.

Woldesenbet and Vinson [8] performed compression tests to determine if specimen geometry has an effect on high-strain rate tests by using graphite/epoxy composites. Their experiments focused not only on varying the length-to-diameter ratio (*L/d*) of the specimen from 0.5 to 2.0, but also included the use of square/rectangular specimen geometry. In comparing the test results in multi-directions showed no statistically significant effect of either *L/d* or geometry could be found.

Kolsky eliminated the axial inertia effects by using a very thin specimen of *L/d* of 0.1. Davies and Hunter [9] concluded that *L/d* should be close to unity to minimize friction effects. Due to the importance of the uniform stress assumption, few researchers had undertaken plastic wave propagation analysis.

Frantz *et al*. [10], showed the advantage of a small dimension over a large one due to the stress within the specimen to equilibrate within the shortest possible time. He also suggested that a slow rising excitation is preferred over a steep rise.

1.3.3 Current areas of Research: Wave Propagation

A valid *SHPB* test requires a uniform stress throughout the specimen. As stress wave entering the specimen from the incident bar and thus creating the axial and radial inertia to oppose the stress equilibrium. It is essential since the tests involve propagation of elastic wave in the pressure bars and both elastic and plastic waves in the specimen.

Davies [3] analyzed wave propagation through the pressure bar by applying the mathematical solutions derived by Pochhammer [7] and Chree [11] equations governing axial vibrations in bars in 1876 and 1889 respectively. These equations were later presented by Love [12] in 1927, and solved numerically by Bancroft [13] in 1941 who plotted the ratio of actual wave speed to minimum frequency propagation speed as a function of the ratio of wavelength to bar

diameter. This gave a better idea as to how higher frequency; lower wavelength waves travel slower and result in dispersion.

Longitudinal stress wave propagation is dispersive for wavelengths with same order of magnitude as the bar diameter which caused distortion of short stress pulses and hence arising unnecessary signals registered by strain gauges. From the theoretical analysis of wave propagation, Gong *et al*. [14] showed that it is possible to reverse the effects of dispersion of moderately dispersed signals by applying appropriate phase shifts to each frequency components.

Longitudinal stress dispersion while propagating in the pressure bar distorts the pulse shape. Gorham and Wu [15] proposed for a dispersion correction method for a pressure bar derived from phase characteristics of various sized metal spheres impact stress. In this method, a measured phase characteristic automatically takes into account any mechanical arrangements as well as any dispersive effects from electronic circuitry.

1.3.4 Research Related to Polyurea and its Dynamic Characterization

Characterization of the mechanical behavior of viscoelastic materials is essential to the proper design of effective damping treatments which are suitable for attenuating structural vibrations over a particular range of operating temperatures and frequencies. The mechanical behavior of polyurea under high rate conditions is relatively unknown.

Boyce and Balizer [16] studied rate-dependent stress-strain behavior of polyurea by *SHPB* and found to have strong hysteresis, cyclic softening, and strong rate-dependence in both the quasi-static and high strain rate regimes, from $10^3 - 10^4\ s^{-1}$.

In order to perform *SHPB* tests at large strain rates, Shim and Mohr [17] modified the conventional *SHPB* striker bar with a hydraulic actuator to achieve almost infinite loading pulse durations. They used thermoplastic nylon bars along with aluminum bars to increase the total

duration of the loading pulse from $472\ \mu s\ to\ 1255\ \mu s$. The use of nylon reduced the impedance mismatch between the bars and the polyurea specimen and improved the input force measurement accuracy. It was shown that intermediate strain rate *SHPB* experiments require very long bars (>20 m) or very short bars (<0.5m) in order to achieve constant strain rate throughout the entire experiments.

Johnson *et al*. [18] employed sensitive piezoelectric strain gauges, hollow transmission bars and lower impedance polymeric pressure bars in separate experimental set up to improve characterizing polyurea at high strain rates and were able to reduce noise levels and achieved better stress-strain curves.

Naik *et al*. [19] showed that viscoelastic nature of the polymeric materials is responsible for the compressive strength increases as with strain rate to increase at high strain rate loading compared to quasi-static loading conditions. But, the rate of increase decreases. It was found that the actual behavior of the epoxy polymer in the stress-strain curve to be non-linear and a power law was used to characterize high strain rate behavior.

Fu *et al*. [20] used *SHPB* to investigate mechanical behavior under dynamic compression at high strain rates of silica aerogel consisting of silica particles coated with thin polyurea layer and used Material Point Method (*MPM*) to simulate that nearly uniform deformation occurs at compression due to the low ratio of pore size to wall thickness and random distribution of the pores. It was also shown that different porosities, obtained by varying the skeletal wall thickness, affect the local stress distribution. Eventually, simulations confirm that the stress– strain behavior of aerogels under compression follows a power-law relationship with the initial bulk density, consistent with experimental results from *SHPB* tests.

Youssef and Gupta [21] used laser-generated stress waves with 1–2 *ns* rise times and 16 ns total duration to characterize polyurea properties. The total strain in the samples was less than 3%. Because of the transient nature of the stress wave, the strain rate varied throughout the deformation history of the sample. A peak value of 1.1×105 s^{-1} was calculated. It was found that the stress-strain characteristics, determined from experimentally recorded incident and transmitted wave profiles, matched satisfactorily with those computed from a 2D wave mechanics simulation in which the polyurea was modeled as a linearly viscoelastic solid with constants derived from the quasi-static experiments. Thus, the test data conformed to the Time-Temperature Superposition (*TTS*) principle even at extremely high strain rates of our test. This then extends the previous observations of Zhao *et al*.

Bai *et al*. [22] described hyper elastic and viscoelastic behaviors of polyurea with Ogden model and Standard Linear Solids (*SLS*) model and the *K-BKZ* model. By fitting the experimental data of split Hopkinson pressure bar (*SHPB*), the *SLS* model is more appropriate to describe the viscoelastic behaviors at strain rates below $1600\ s^{-1}$, but the *K-BKZ* model performs better at strain rates over $2100\ s^{-1}$ because of the substantial increase of Young's modulus and the state of polyurea transforming from rubbery to glassy.

Joshi and Milby [23] studied the effect of various composition of polyurea with varying molecular weights using a *SHPB* arrangement equipped with titanium bars with high strain rates of 6000/s. No hardening behavior was observed with higher molecular weight composition but showed lower yield while on the other hand, the blend of 250/1000 show higher load bearing capability but lower strain hardening effects than the 600 and 1000 molecular weight amine based materials.

Golla–Hughes method (*GHM*) parameters used in the characterization of Scott double-face adhesive 3M Scotch viscoelastic material as a sandwich beam were experimentally determined and *GHM* based finite element model was presented and validated through numerical comparisons with classic formulation results by Barbosa and Farage [24]. A numerical model using the proposed finite element model was dynamically tested and the obtained results were compared with experimental results counterpart, showing good agreement. Another important point was also observed that time-domain analysis through *GHM* formulation is very simple since the stiffness matrix is constant.

Mohotti *et al*. [25] studied and quantified the behavior of polyurea coated composite aluminum plates under high velocity projectile impact and deduced the ability of multilayered composite plate systems in reducing the residual velocity of projectiles and found out that polyurea coatings have resulted in a higher residual velocity reduction per unit areal density than aluminum alloys and thus increasing the energy absorption.

Mohotti *et al*. [26] also investigated the behavior of polyurea coated composite aluminum plates subjected to rigid blunt-nosed projectile impact both numerically and experimentally and concluded that polyurea coated plates showed a considerable reduction in out-of-plane deformation when compared to the uncoated plates. By increasing the thickness of polyurea coatings from 6 mm to a 12 mm, permanent deformation of the plates can be reduced significantly and thus makes it suitable as an efficient energy absorbing/damping material against low velocity impact. Mohotti *et al*. [27] also proposed a rate dependent term in the original Mooney-Rivlin model to predict the non-linear hyper-elastic strain energy variation and stress-strain variation behavior of polyurea and were validated using high strain material data for polyurea.

Under impulsive loads in direct pressure-pulse experiments, Amini *et al*. [28] modeled the response of monolithic DH-36 steel plates and bilayer steel-polyurea plates focusing on the effects of the relative position, thickness and interface bonding strength of polyurea and found out that it improved overall performance both in terms of failure mitigation and energy absorption as long as it remains bonded to the steel layer. They also concluded that presence of polyurea on the front face aggravates the initial shock loading effect versus on the front face of a bilayer plate, due to transmitting a greater amount of the impact energy due to a better impedance matching. Tekalur *et al*. [29] validated experimentally that weight addition of layered *E*-glass vinyl ester (*EVE*) with polyurea (*PU*) increase blast resistant properties by 60% but the performance enhancement in the layered material is about 25% better (when polyurea faces the blast) and in case of sandwich composite (*EVE/PU/EVE*), the blast performance is enhanced by more than 100%.

Qiao *et al*. [30] carried out Dynamic mechanical analysis (*DMA*) (over the temperature range from 80 to 70^{o} C at five frequencies) and ultrasonic measurements (frequency range 0.5–2 *MHz* and the temperature range 60– 30^{o} C) to formulate Master curves of Young's storage and loss moduli and complex longitudinal, shear, bulk and Young's moduli. Combining these results provided an estimate of the complex bulk and Young's moduli at high frequencies and concluded that at higher frequencies polyurea become resonators and therefore contributes to higher loss. It is expected that by varying the size, properties, and by introducing of materials, the loss spectrum can be enhanced and tailored towards specific applications.

1.4 Objectives and Tasks

The objectives of the present dissertation are to develop comprehensive theoretical and experimental study of the characterization of Polyurea composites subjected to high strain impact loading. The composites under consideration consist of multi-layers of polyurea/aluminum arranged in one dimension configuration. Finite element models (*FEM*) to be developed describes the dynamics of the viscoelastic behavior of the polyurea using the Golla-Huges-Mctavish (*GHM*) mini-oscillator approach. The model is intended to enable the predictions of the structural stress, strain, strain rate, relaxation modulus, loss factor of the polyurea composites for different layering arrangements. The predictions of the developed *FEM* are to be compared to the predictions of the commercial finite element package *ANSYS*. Also, the *FEM* predictions are to be validated experimentally using the Split Hopkinson Pressure Bar (*SHPB*) which is used to monitor the dynamics of the polyurea composites at different levels of strain rates.

In order to achieve these objectives, the following tasks are set:

- Develop a finite element model (*FEM*) of the polyurea/aluminum composites using the Golla-Hughes-MacTavish (*GHM*) approach to account for the dynamics of the viscoelastic behavior of the polyurea.
- Extend the developed *FEM* to simulate the impact operation and the high strain rate loading conditions encountered when using the Split Hopkinson Pressure Bar (*SPHB*).
- Develop a finite element model (*FEM*) of the polyurea/aluminum using *ANSYS* commercial software package. In *ANSYS*, the viscoelastic characteristics of the polyurea and represented a Prony Series approach which is translates the *GHM* model to an acceptable form for *ANSYS*.
- Establish comparisons between the predictions of the *FEM/GHM* approach with those of *ANSYS*.

- Experimentally validate the predictions of the models by testing several configurations of the polyurea composites by using the Split Hopkinson Pressure Bar (*SPHB*).
- Quantify the stress-strain characteristics at different strain rate for different configurations of the polyurea composites.
- Analytically develop a model based on transfer matrix approach to identify and compare dispersion curves and pass-stop band domains for the longitudinal wave propagation in polyurea composites by using Bloch wave method.

1.5 Scope and Outline of the Dissertation

This dissertation is arranged in six chapters. In Chapter 1, a brief review of the literature of the operation of polymers, in general, and polyurea, in particular, under high strain loading conditions. In Chapter 2, a brief review of the theory of viscoelasticity is presented. The development of the finite element model of polyurea composites is presented in chapter 3 by using the Golla-Hughes-MacTavish (*GHM*) approach to account for the dynamics of the viscoelastic behavior of the polyurea. Chapter 4 summarizes the experimental effort which aims at testing several configurations of the polyurea composites using the Split Hopkinson Pressure Bar (*SPHB)* and thus producing the stress-strain characteristics at different strain rate and configurations of the polyurea composites. Chapter 5 presents the application of periodic arrangement of the polyurea composites in mitigating impact loading conditions. Chapter 6 presents a summary of major contributions, conclusions arrived with this study along with potential future directions for extending the present work.

1.6. SUMMARY

This chapter has presented a brief review of the literature of the operation of polymers, in general, and polyurea, in particular, under high strain loading conditions. The chapter has also outlined the scope of the dissertation and the contents of the individual chapters.

Chapter 2

VISCOELASTICITY

2.1 Viscoelasticity

Viscoelastic materials (*VEM*) such as polymers, ceramics, rubbers, woods etc. exhibit a time/rate dependent stress-strain relationship which implies the combined presence of deformation characteristics associated with elastic solids and viscous fluids.

The loading and unloading stress-strain path of a linear elastic material is identical and there is no dependence on the rate of loading or straining as shown in Figures. 2.1(a) and 2.1(b). This type of material returns to its original shape when the load is removed.

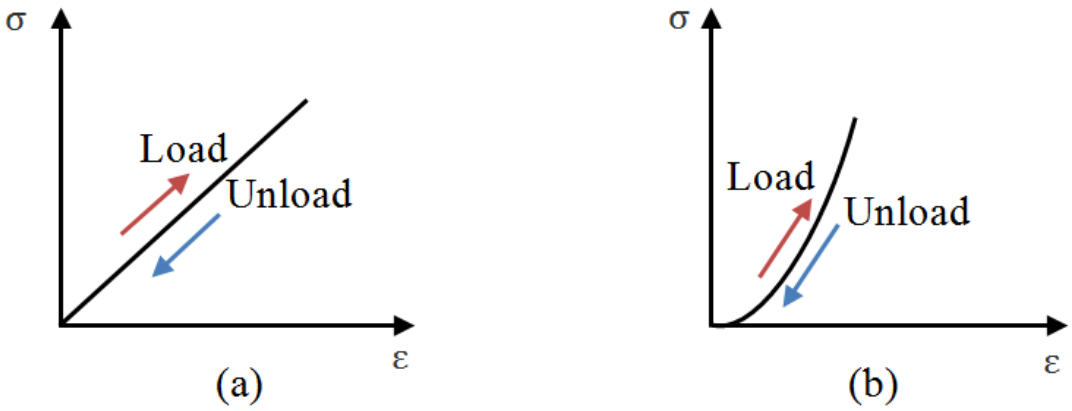

Figure 2.1: Illustration of the (a) linear (b) non-linear elastic behavior with energy recovery

The deformation behavior and the accompanying nature of the exchange of energy are quite different in the case of viscous materials. Viscoelastic materials exhibit non-constant stiffness and damping properties. The stiffness and damping can be described as frequency dependent. The

loading and unloading stress-strain curves of a viscoelastic material is not identical and there is a dependence on the rate of loading or straining as shown in Figures. 2.2(a) and 2.2(b).

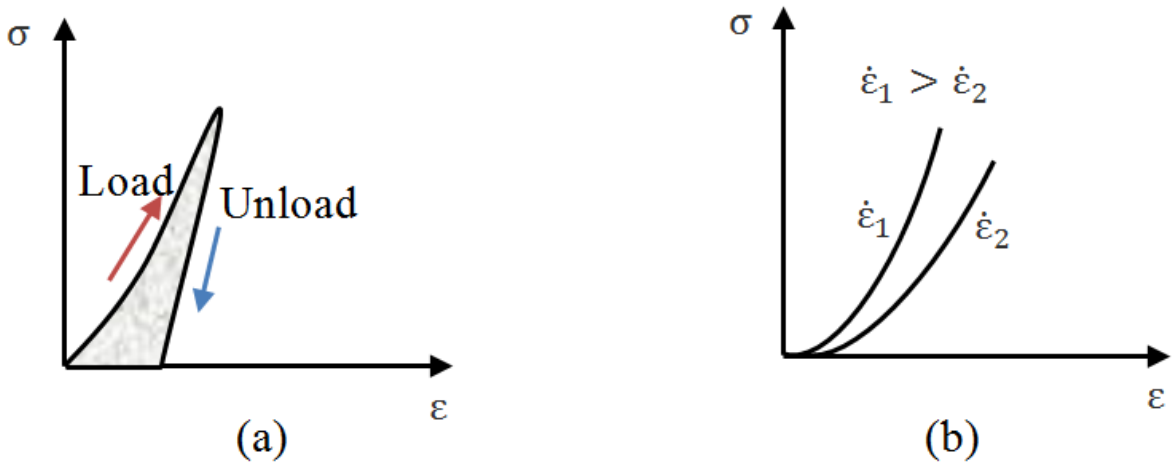

Figure 2.2: Illustration of the (a) loading and unloading with possible permanent deformation (non-zero strain at zero stress), (b) different rates of stretching

The effect of stretching shows that the viscoelastic material depends on time whereas for an elastic material with a given stress level loaded for one second or for one day, the resulting strain will be the same.

For viscoelastic materials, the relationship between stress and strain can be expressed as

$$\sigma = \sigma(\varepsilon, \dot{\varepsilon}) \tag{2.1}$$

Eqn. (2.1) shows that stress σ , is not only a function of strain ε , but is also a function of the strain rate,

$$\dot{\varepsilon} = \frac{d\varepsilon}{dt}, \qquad \text{where } t \text{ is time.}$$

It is important to note here some of the basic phenomena encountered in viscoelastic materials are:

- If the stress is held constant, the strain increases with time (creep).
- If the strain is held constant, the stress decreases with time (relaxation).
- The effective stiffness depends on the rate of load.

2.2 Properties of viscoelastic material

A strain of magnitude ε_0 is assumed suddenly applied at time $t = 0$ and held constant thereafter. Mathematically, we express such a strain history by means of the Unit step function, $H(t)$.

$$H(t) = \begin{cases} 0, & t < 0 \\ 1, & t \geq 0 \end{cases} \tag{2.2}$$

2.2.1 Creep

It is the tendency of a *VEM* to slowly move or deform permanently under the influence of constant mechanical stress. The rate of deformation is called the creep rate which is the slope of the line in a Strain vs. Time curve. In one dimension, Time dependent stress $\sigma(t)$ with a step function beginning at time zero is

$$\sigma(t) = \sigma_0 H(t) \tag{2.3}$$

The strain $\varepsilon(t)$ in a viscoelastic material will increase with time. The ratio, $J(t) = \frac{\varepsilon(t)}{\sigma_0}$ is called the "C*reep Compliance*".

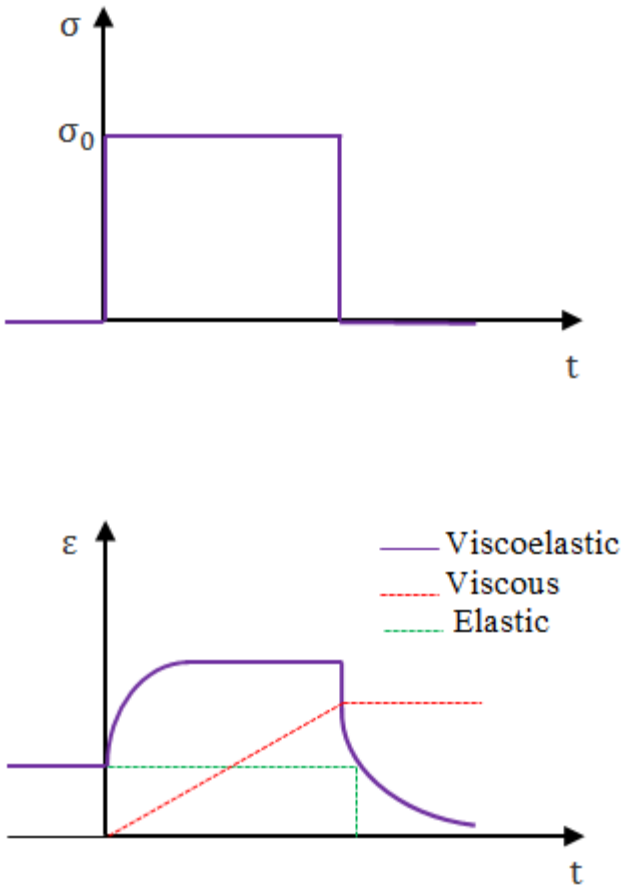

Figure 2.2: Illustration of the creep behavior

The creep response in Figure 2.2 is shown beginning at the same time as the stress history, which is the cause. If the load is released at a later time, the strain will exhibit recovery or a progressive decrease of deformation. Depending on the material, strain in recovery may or may not approach zero.

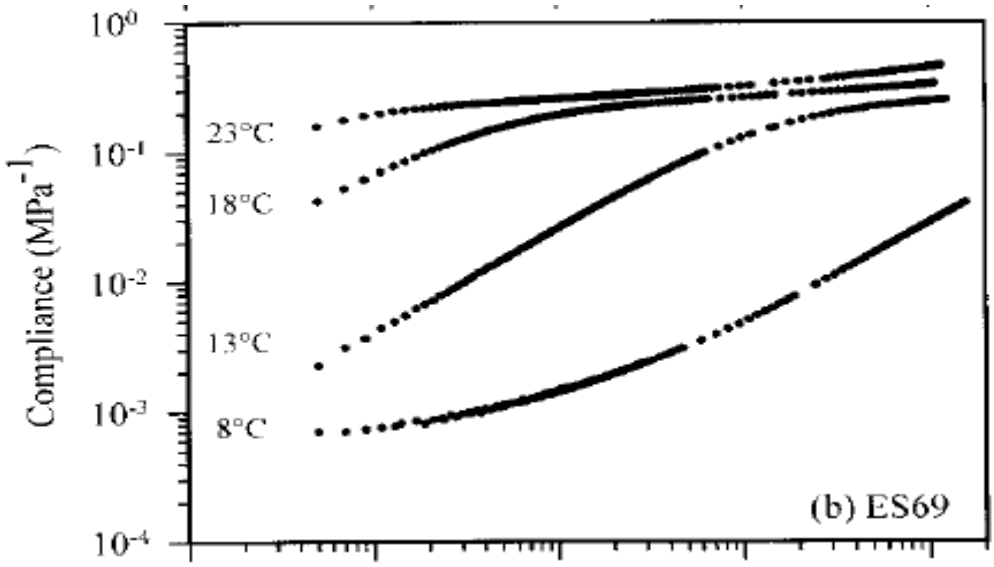

Figure 2.3: Typical creep behavior at different temperatures (Chen et al., 1999)

2.2.2 Stress Relaxation

It describes how *VEM* relieve stress under constant strain. If we suppose the strain to be a step function of magnitude beginning at time zero:

$$\varepsilon(t) = \varepsilon_0 \varepsilon(t) \tag{2.4}$$

Stress $\sigma(t)$ in a viscoelastic material will decrease as shown in Figure 2.4. The ratio,

$$E(t) = \frac{\sigma(t)}{\varepsilon_0} \tag{2.5}$$

E(*t*) is called the "*Relaxation Modulus*". In linear materials, it is independent of strain level, so $E(t)$ is a function of time alone. The symbol E for Young's modulus as stiffness in uniaxial tension.

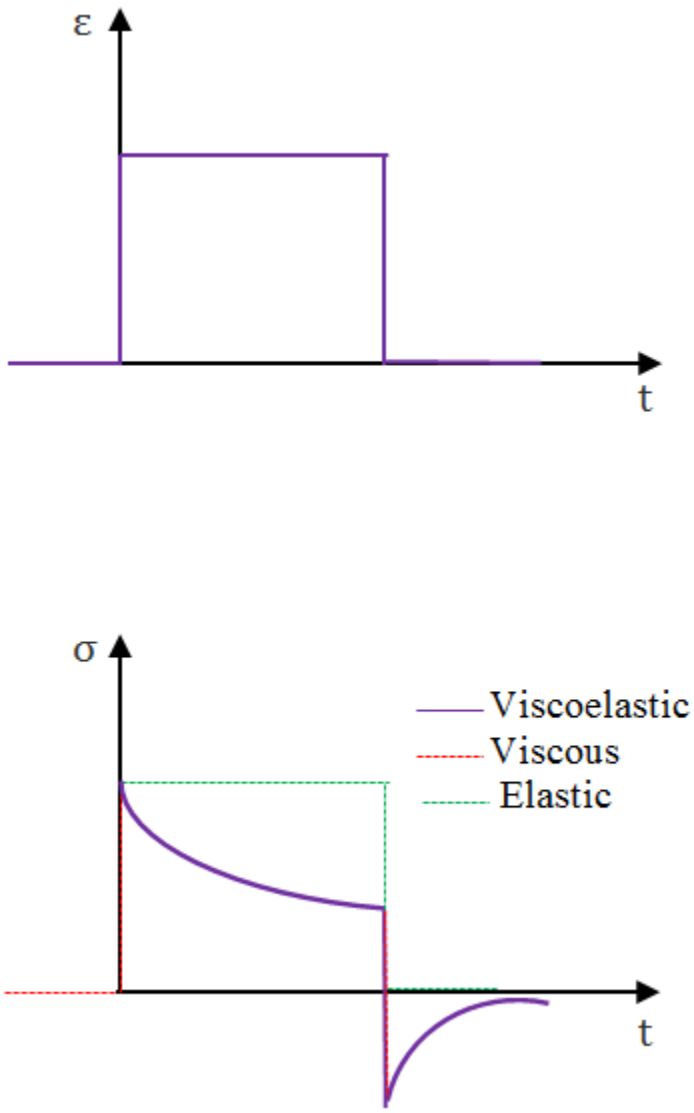

Figure 2.4: Illustration of the stress relaxation

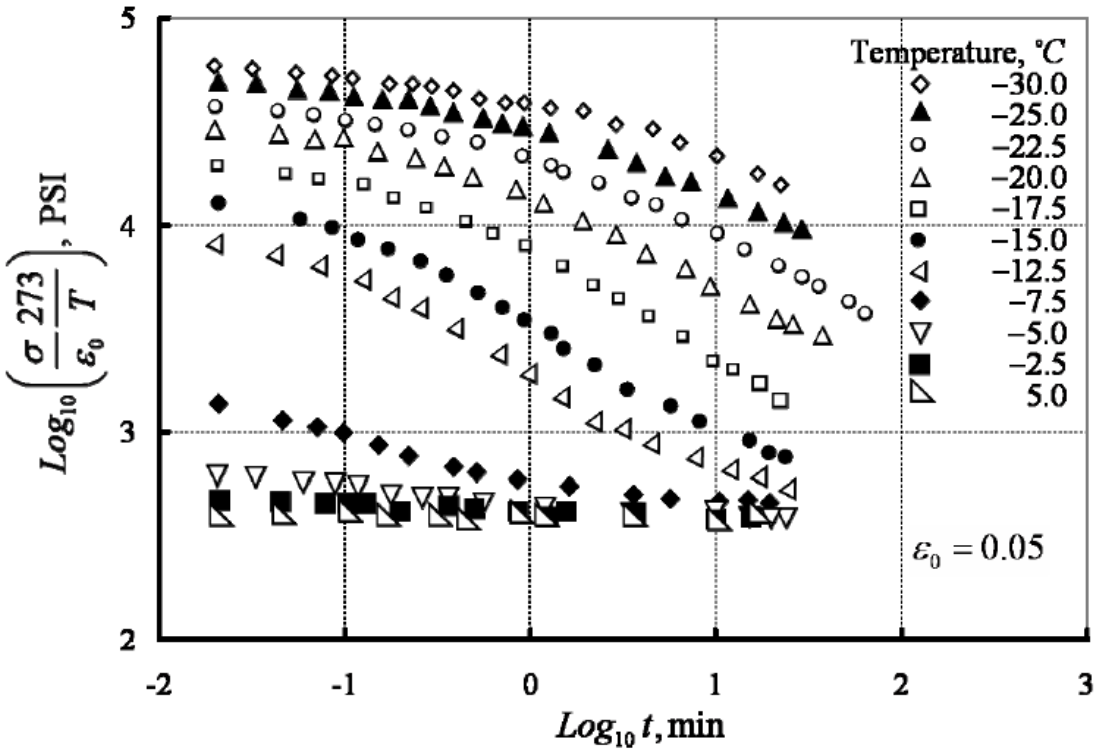

Figure 2.5: Typical relaxation behavior at different temperatures (Chae et al., 2010)

2.3 Characterization of Dynamic Behavior of *VEM*

The characterization and modeling of the mechanical behavior of viscoelastic materials is essential in proper designing and analysis of effective damping treatments which are suitable to avoid failure by attenuating structural vibrations or to ensure optimal operating conditions over a particular range of operating temperatures and frequencies. The dynamic response of viscoelastic materials to sinusoidal load is of paramount interest where applications like damping of vibration or the absorption of sound is important.

2.3.1 Response to Step Input

Considering the time histories of the creep stress applied to a *VEM* along with the resulting creep strains shown in Figure 2.6.

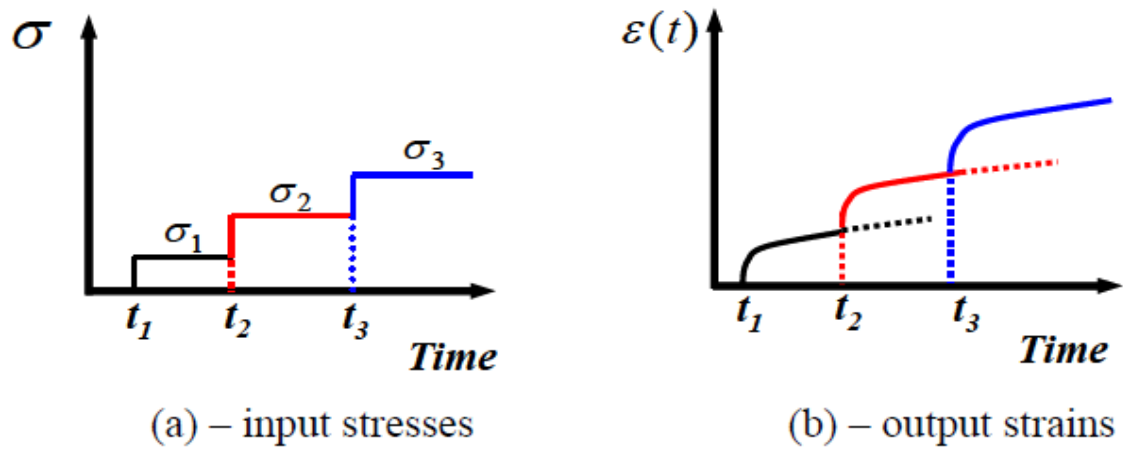

Figure 2.6: Superposition of the creep strains resulting from stepped creep stresses

Assuming the compliance is only function of time and not stress, if a constant load σ_1 is applied to a viscoelastic specimen and the time dependent strain is recorded as

$$\varepsilon_1(t) = (\sigma_1 - 0)J(t - t_1) \tag{2.6}$$

as shown in Figure 2.6 and the load is removed.

A larger stress σ_2 is applied. The time dependence of the strain ε_2 becomes:

$$\varepsilon_2(t) = (\sigma_2 - \sigma_1)J(t - t_2) \tag{2.7}$$

Then, the resulting creep response becomes:

$$\varepsilon(t) = (\sigma_1 - 0)J(t - 1) + (\sigma_2 - \sigma_1)J(t - t_2) + (\sigma_3 - \sigma_2)J(t - t_3) \ldots\ldots\ldots\ldots \tag{2.8}$$

In a compact form:

$$\varepsilon(t) = \sum_{i=-\infty}^{n} \Delta\sigma_i J(t - t_i) \tag{2.9}$$

Equation (2.9) is a mathematical representation of the discrete Boltzmann superposition principle whereby the time history of the strain is described by a superposition of the effects of the incremental stresses imposed on the *VEM*.

Writing equation (2.9) in the continuous time domain:

$$\varepsilon(t) = \int_{-\infty}^{t} \frac{\partial\sigma(\tau)}{\sigma(\tau)} J(t-\tau)d\tau \tag{2.10}$$

In a similar fashion, the effect of time varying relaxation strains on the time history of the resulting stress can be illustrated as shown in Figure 2.7.

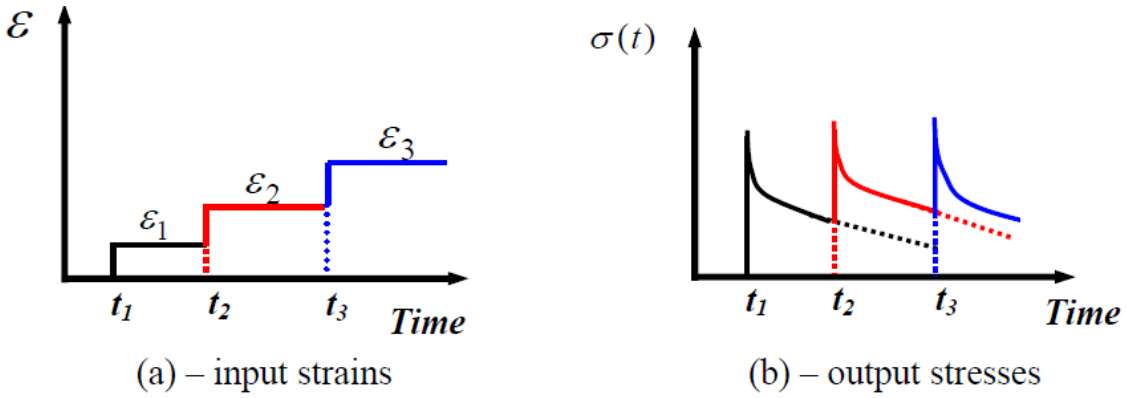

Figure 2.7: Superposition of the relaxation stresses resulting from stepped creep strains

Mathematically, the superposition of the stresses can be described, in terms of the incremental strains and the relaxation modulus $E(t)$ by:

$$\sigma(t) = \int_{-\infty}^{t} \frac{\partial\varepsilon(\tau)}{\sigma(\tau)} E(t-\tau)d\tau \tag{2.11}$$

2.3.2 Relationship between the Relaxation Modulus and Complex Modulus

Substituting $a = t - \tau$ into Equation (2.11):

$$\sigma(t) = \int_0^\infty \frac{\partial \varepsilon(t-a)}{\sigma a} E(a)da \tag{2.12}$$

If the *VEM* is subjected to sinusoidal excitation such that:

$$\varepsilon(t) = \varepsilon_0 e^{i\omega t} \tag{2.13}$$

Combining equations (2.12) and (2.13) gives:

$$\sigma(t) = \int_0^\infty \varepsilon_0 \omega i e^{i\omega(t-a)}\, E(a)da = \varepsilon_0 e^{i\omega t} \int_0^\infty \omega i e^{-i\omega a}\; E(a)da$$

$$\sigma(t) = \varepsilon \int_0^\infty \omega[\sin(\omega a) + i\cos(\omega a)]\; E(a)da = \left[E^{'} + iE^{''}\right]\varepsilon \tag{2.14}$$

Where,

$$E' = \int_0^\infty \omega[\sin(\omega a)]\, E(a)da \tag{2.15}$$

And

$$E'' = \int_0^\infty \omega[\cos(\omega a)]\, E(a)da \tag{2.16}$$

Equations (2.15) and (2.16) establish the relationship between the storage and loss moduli to the relaxation modulus. It is important here to note that as: $\sigma(t) = [E' + iE'']\varepsilon$

Then, from equations (2.13) and (2.14),

$$\sigma(t) = [E'(1 + i\eta)]\varepsilon_0 e^{i\omega t} = E'\sqrt{1+\eta^2}\,\varepsilon_0 e^{i(\omega t+\delta)} = |E^*|\varepsilon_0 e^{i(\omega t+\delta)} \tag{2.17}$$

where, $\eta = loss\ factor = \tan\delta$ and $|E^*| = E'\sqrt{1+\eta^2} = magnitude\ of\ modulus.$

with $$\sigma_0 = [E'(1 + i\eta)]\varepsilon_0 \tag{2.18}$$

Equation (2.17) indicates that the strain lags the stress by a phase angle δ as shown in Figure 2.8.

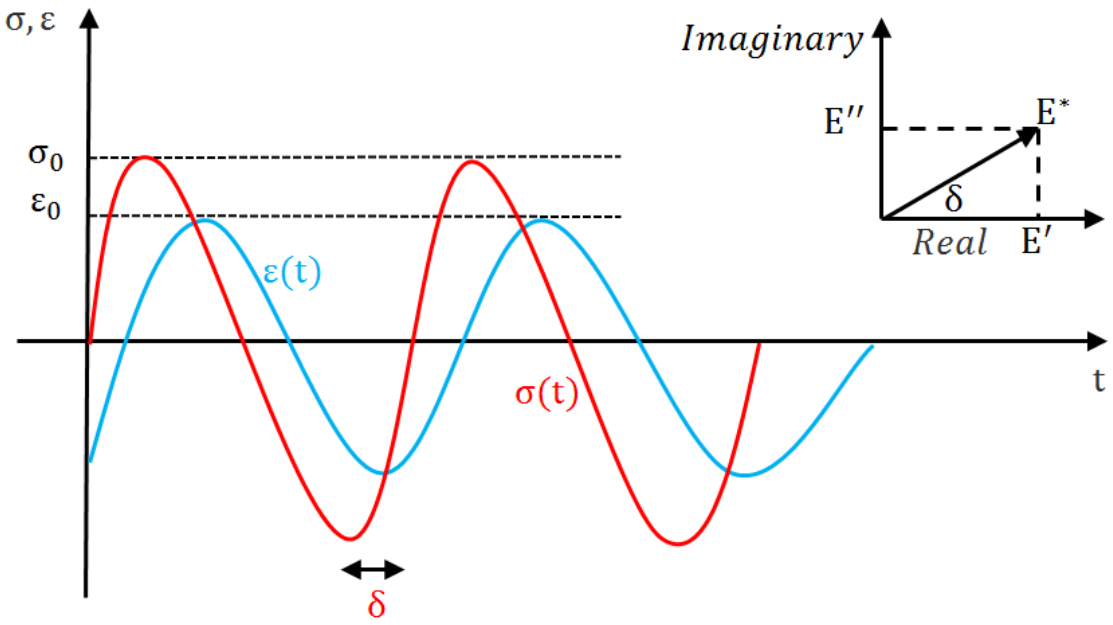

Figure 2.8: Time history of the Stress and Strain

2.4 Conversion from time and frequency domain parameters

Indirect conversion approach is a well-established approach for obtaining frequency dependent dynamic moduli from creep or relaxation measurements. In this approach, the experimental data are curve-fitted to a particular time-domain model such as the generalized Maxwell model or the generalized Kelvin-Voigt model which are shown in Figure 2.9. Subsequently, the resulting curve-fitted time-domain models are transformed to the frequency-domain using Fourier transform in order to extract the complex viscoelastic modulus.

2.5 Prony Series Representation of Linear Viscoelasticity

Linear viscoelastic behavior can be described by the generalized Maxwell model shown in Figure 2.9.

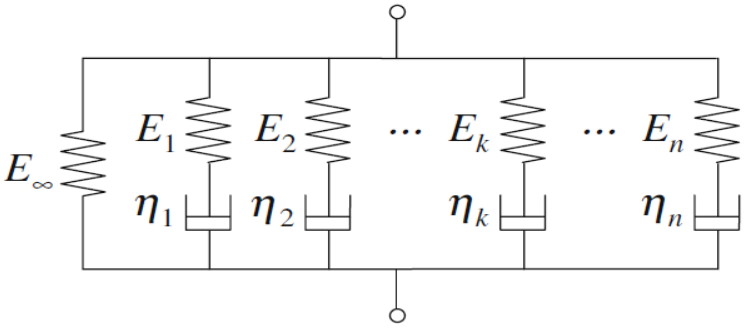

Figure 2.9: Generalized Maxwell Model (GMM)

An extra isolated spring E_∞ is added to represent arrheodictic behavior that cannot exhibit steady-state flow. The behavior of each Maxwell element, where a spring and a dashpot are connected in series, is expressed as

$$\dot{\varepsilon_k} = \frac{\dot{\sigma_k}}{E_k} + \frac{\sigma_k}{\eta_k}, k = 1, 2, \ldots . n \tag{2.19}$$

If a constant strain ϵ_0 is imposed at t = 0, the solution of Eq. (2.19) is given by

$$\sigma_k(t) = \sigma_{k,0} e^{\frac{-t}{\tau_k}} \tag{2.20}$$

where $\sigma_{k,0} = E_k \epsilon_0 = initial\ stress\ at\ t = 0$ and $\tau_j = retardation\ time\ of\ the\ k^{th}\ element$

Then, the stress is given by:

$$\sigma(t) = E_\infty \epsilon_0 + \sum_{k=1}^{n} \sigma_{k,0}\, e^{\frac{-t}{\tau_k}} = \epsilon_0 \left[E_\infty + \sum_{k=1}^{n} E_k\, e^{\frac{-t}{\tau_k}} \right] \tag{2.21}$$

The relaxation modulus $E(t)$ is defined as

$$E(t) = \frac{\sigma(t)}{\epsilon_0} = \left[E_\infty + \sum_{k=1}^{n} E_k\, e^{\frac{-t}{\tau_k}} \right] \tag{2.22}$$

which is essentially the Prony series representation. Here, E_∞ is the final (or equilibrium) modulus, and

$$E_0 = \left[E_\infty + \sum_{k=1}^{n} E_k \right]$$

is the instantaneous modulus. A pair of E_k and τ_k is referred to as a Prony pair.

The parameters $E_0, E_k, \rho_k, and\ \ \tau_k$ are all positive constants and are identified in order to optimally curve-fit the experimental data.

Once these parameters are obtained, time domain equations are transformed to the frequency domain using Fourier transform yielding complex modulus E^* as below:

$$E^*(\omega) = E_0 + \sum_{k=1}^{n} E_k \frac{i\omega\rho_k}{1 + i\omega\rho_k} \tag{2.23}$$

2.6 Time Domain Characterization Method of the Dynamic Properties of Viscoelastic Material (*VEM*) by Split Hopkinson Pressure Bar (*SHPB*)

There are two ways to characterize *VEM* properties. One way is Frequency Domain measurements in which dynamic responses are measured at multiple oscillation frequencies. Then the Storage and Loss modulus in the frequency domain can be converted into the relaxation modulus or creep in the time domain by using an appropriate conversion method. The other way is to characterize the relaxation or creep behavior directly in the time domain by applying a fixed load for certain duration of time. Time domain measurement techniques are equally as important as frequency domain measurements. Below Figure 2.10 shows Time Scale in time domain measurements.

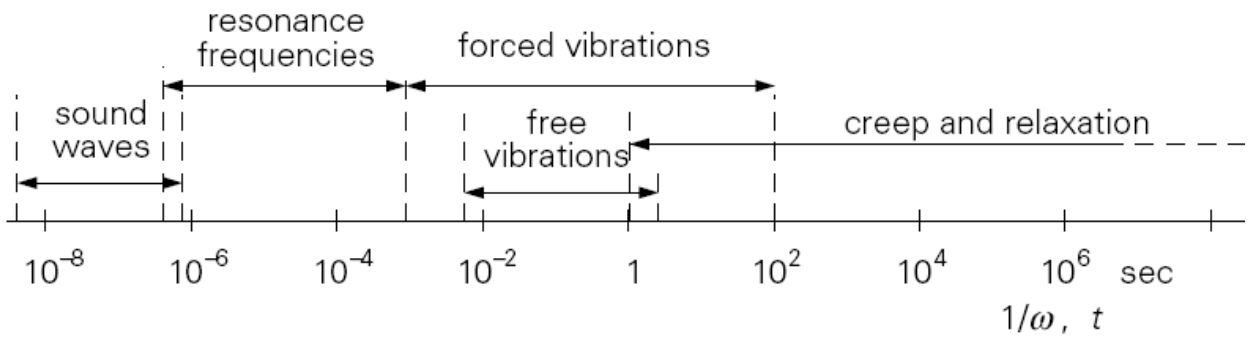

Figure 2.10: Time Scale in Time Domain measurements (Ward, 1983)

2.6.1 Fundamentals of Hopkinson Pressure Bar (*SHPB*) Testing in Time Domain

A Hopkinson bar test apparatus usually consists of the following:

- Two long symmetrical bars namely Incident and Transmitted Bars. Traditionally these bars are made of high strength structural metal because the yield strength of the material determines the maximum stress attainable within the deforming specimen.
- Bearing and alignment fixtures to allow the bars and striking projectile to move freely while retaining precise axial alignment
- Compressed gas gun for accelerating a controlled compressed pulse in the incident bar
- Strain gauges mounted on both bars to measure the stress-wave propagation in the bars
- Data acquisition system to control, record, and analyze the stress-wave data in the bars

During a *SHPB* test, the test specimen is compressed between two bars which are called the incident bar and the transmitter bar as shown in Figure 2.11. The incident bar is then impacted by a striker bar which is launched at high speed using compressed gas. The stress-strain characteristics of the specimen are determined through measurements of resulting stress waves in the two bars as measured by strain gages which are bonded to the incident bar and the transmitter bar.

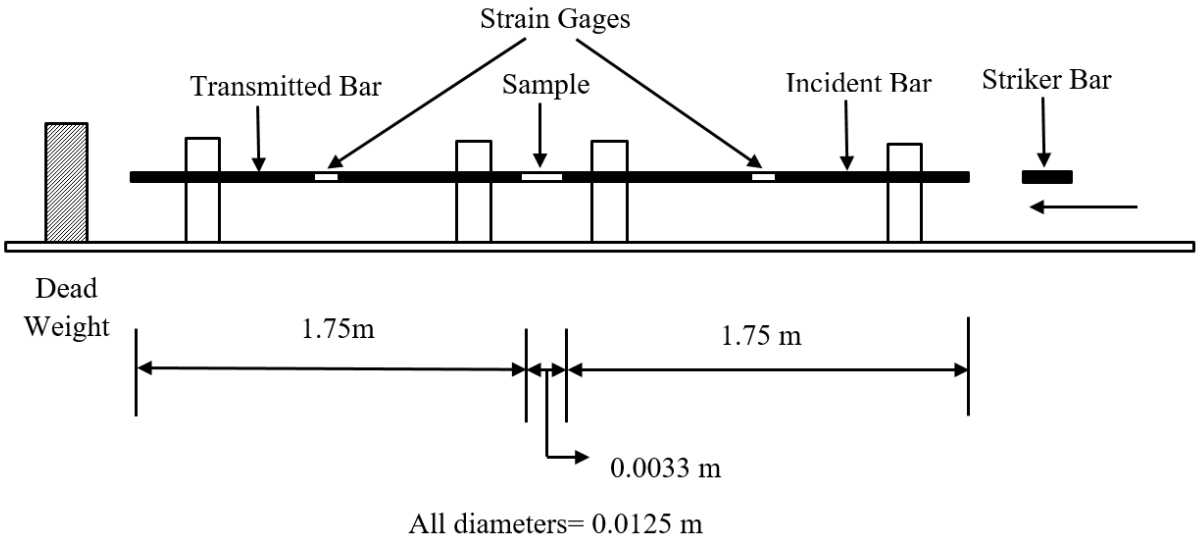

Figure 2.11: Schematic of Split Hopkinson Pressure Bar (*SHPB*) apparatus

2.6.2 Theory of Split Hopkinson Pressure Bar (*SHPB*)

Since Incident and Transmitted bars are identical to each other, it is only considered one of them in developing the equation of motion governing axial vibration. The stress-strain behavior of a *VEM* tested in a *SHPB* is based on the same Principle of 1-D wave propagation assuming bars are thin, long, linear, and dispersion free.

The theory of *SHPB* can be understood using the diagram shown in Figure 2.12.

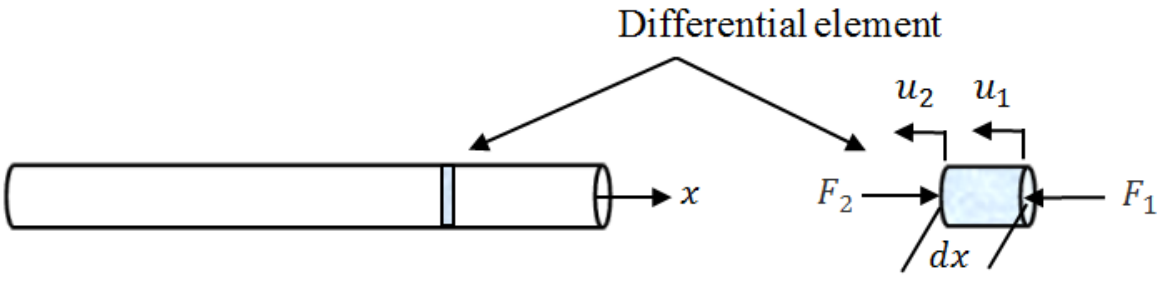

Figure 2.12: Pressure bar shown with differential element prior to deformation

where $dx = differential\ element\ length,$

$A = cross\ sectional\ area,$

$\rho = Density,$

$E = Elastic\ modulus,$

$u = displacement\ of\ the\ bar\ at\ any\ location$

Compressive forces $F_1\ and\ F_2$ are acting on both sides of the element prior to impact. Hence strains can be expressed in terms of the elemental displacements by assuming uniaxial stress. Therefore, forces,

$$F_1 = AE\frac{\partial u_1}{\partial x} \text{ and } F_2 = AE\frac{\partial u_2}{\partial x} \tag{2.24}$$

can be expressed in terms of strains of the incident, reflected and transmitted pressure bars as

$$F_1 = AE(\varepsilon_i + \varepsilon_r) = F_2 = AE\varepsilon_t \tag{2.25}$$

where, $\varepsilon_i = Incident\ strain$, $\varepsilon_r = Reflected\ strain$, and $\varepsilon_t = Transmitted\ strain.$

Considering the specimen sandwiched between the incident and the transmitted bar, the average force and stress on the specimen are found from Equation (2.25)

$$F = \frac{1}{2}\left(F_1 + F_2\right) \tag{2.26}$$

$$\sigma = \frac{F_{avg}}{A_s} = \frac{AE}{2A_s}(\varepsilon_i + \varepsilon_r + \varepsilon_t) \tag{2.27}$$

where, $A_s = Specimen\ cross\ sectional\ area$

But from the compatibility condition of deflection,

$$\varepsilon_i + \varepsilon_r = \varepsilon_t \tag{2.28}$$

substituting Equation (2.28) into Equation (2.27),

$$\sigma = \frac{AE}{A_s}\varepsilon_t \tag{2.29}$$

Now, the equation describing the motion of the pressure pulse,

$$AE\left(\frac{\partial u_1}{\partial x} - \frac{\partial u_2}{\partial x}\right) = Adx\rho\frac{\partial^2 u_1}{\partial t^2} \tag{2.30}$$

By simplifying Equation (2.30) yields the equation of motion of the bar

$$c^2\left(\frac{\partial u_1}{\partial x} - \frac{\partial u_2}{\partial x}\right) = \frac{\partial^2 u_1}{\partial t^2}dx \tag{2.31}$$

where $c = \sqrt{\frac{E}{\rho}} = sound\ speed\ in\ the\ bar$

Now assuming the rate of change of displacement of both sides of the element are equal, we can write,

$$u_2 = u_1 + \frac{\partial u_1}{\partial x}dx \tag{2.32}$$

Differentiating Equation (2.32), we get

$$\frac{\partial u_2}{\partial x} = \frac{\partial u_1}{\partial x} + \frac{\partial^2 u_1}{\partial x^2}dx \tag{2.33}$$

Substituting Equation (2.33) into Equation (2.31) gives

$$c^2\frac{\partial^2 u}{\partial x^2} = \frac{\partial^2 u}{\partial t^2} \tag{2.34}$$

$$\frac{\partial^2 u}{\partial x^2} - \frac{1}{c^2}\frac{\partial^2 u}{\partial t^2} = 0 \tag{2.35}$$

Equation (2.35) which leads to theoretical wave velocity for a wave of infinite wavelength will be used to calculate the specimen strain and strain-rate. The wave directions and idealized wave forms are shown in Figure 2.13 (a) and (b)

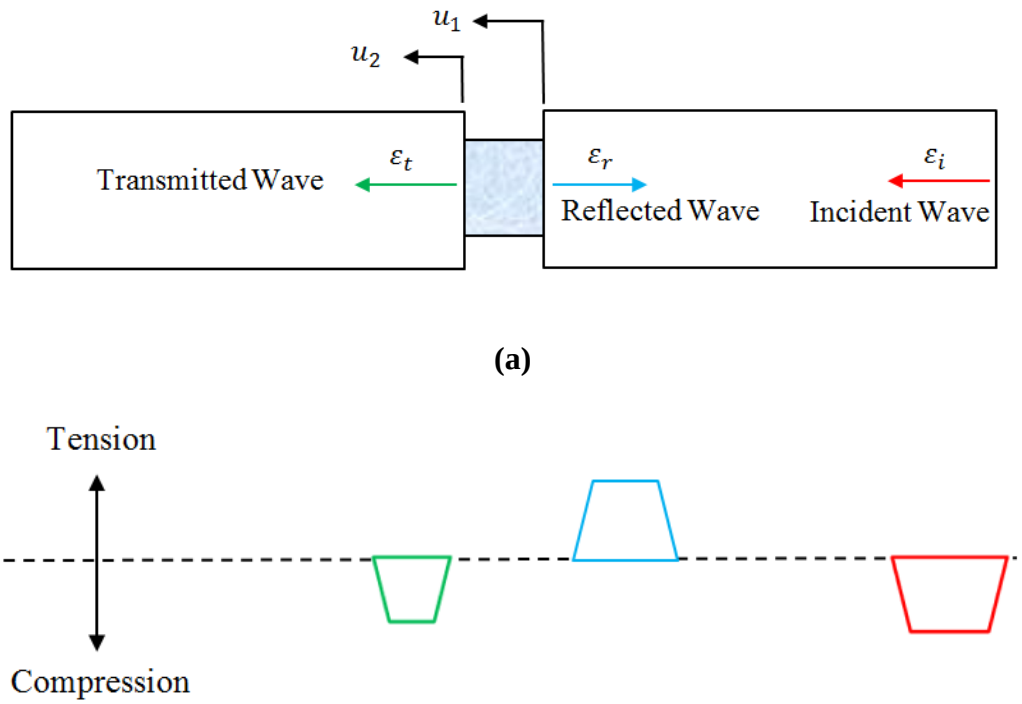

Figure 2.13: (a) Wave directions in *SHPB* (b) Idealized wave forms

Now, the strain rate is defined as change of strain of a material with respect to time and indicates displacement over time which in turn indicates velocity.

Strain rate in the specimen ($\dot{\varepsilon}_s$) is calculated from pressure bar – specimen interface velocities which in turn can be calculated from the strains in the pressure bars.

Now,

$$\frac{\partial v}{\partial t} = \frac{\partial}{\partial t}\left(\frac{\partial u}{\partial t}\right) = \frac{\partial^2 u}{\partial t^2} \tag{2.36}$$

where $v = particle\ velocity$

$$s = E\frac{\partial u}{\partial x} \tag{2.37}$$

Differentiating Equation (2.37) with respect to *x*

$$\frac{\partial s}{\partial x} = E\frac{\partial^2 u}{\partial x^2} \tag{2.38}$$

where $s = stress\ across\ the\ cross\ section$

By assuming a positive harmonic wave of the form:

$$s(x,t) = P(x)e^{i(\omega t - kx)} \tag{2.39}$$

where $P(x)$ is spatial function of *x* and $e^{i(\omega t-kx)}$ is a temporal function of the time *t* with ω denoting the frequency of oscillation of the waves and

$$k = \frac{\omega}{c} = wave\ number \tag{2.40}$$

Taking the first derivative of equation (2.39) with respect to x,

$$\frac{\partial s(x,t)}{\partial x} = -ikP(x)e^{i(\omega t-kx)} \tag{2.41}$$

Substituting Equation (2.41) into equation (2.42) and pre-multiplying the *RHS* of equation (2.34) by the heavyside operator, one attains

$$\rho i\omega v(x,t) = ikP(x)e^{i(\omega t-kx)} \tag{2.42}$$

which yields,

$$v(x,t) = \frac{kP(x)e^{i(\omega t-kx)}}{\rho\omega} \tag{2.43}$$

By substituting the values of $k\ and\ v(x,t)$ back in Equation (2.43) yields:

$$v(x,t) = \frac{s(x,t)}{\rho c} \tag{2.44}$$

Assuming pressure equivalent to stress across the bar and rewrite the particle velocity in terms of bar, we can write

$$s(x,t) = E\varepsilon(x,t) \tag{2.45}$$

Substituting Equation (2.45) into Equation (2.44) gives the velocity in terms of the bar strains

$$v(x,t) = c\varepsilon(x,t) \tag{2.46}$$

Now, the strain rate in the specimen

$$\dot{\varepsilon_s} = \frac{(\dot{u}_{1-}\dot{u}_2)}{l_s} \tag{2.47}$$

where, $l_s = instantaneous\ specimen\ length$

Also, $$\dot{u}_1 = v(x,t) = c(\varepsilon_r - \varepsilon_i) \tag{2.48}$$

and $$\dot{u}_2 = -c\varepsilon_t \tag{2.49}$$

By setting the reflected component of the wave = 0 due to the presence of an anechoic termination at the end of the transmitter bar.

Substituting these velocities back in Equation (2.47) yields,

$$\dot{\varepsilon_s} = \frac{(\dot{u}_{1-}\dot{u}_2)}{l_s} = \frac{c(\varepsilon_r - \varepsilon_i + \varepsilon_t\ )}{l_s}\dot{\varepsilon_s}$$

$$\dot{\varepsilon_s} = \frac{2c\varepsilon_r}{l_s} \tag{2.50}$$

Equation (2.50) can be integrated to get the specimen strain as

$$\varepsilon_s(t) = \frac{2c}{l_s}\int \varepsilon_r(t)dt \tag{2.51}$$

Accordingly, measuring the reflected strain ε_r and the transmitted strain ε_t can be used to calculate the strain ε_s and stress σ_s in the *VEM* as function of time. From such time histories, the stress-strain characteristics, the creep compliance, and complex modulus can be obtained.

2.7. SUMMARY

This chapter has presented a brief review of the theory of viscoelasticity and in particular the emphasis is placed on the characterization of the stress and strain characteristics of the *VEM* using the Split Hopkinson Pressure Bar (*SHPB*) whereby the material is subjected to high strain rates.

Chapter 3

FINITE ELEMENT MODELING OF POLYUREA COMPOSITES

3.1 Advanced Model to incorporate *VEM* into FEM

Classical Viscoelastic material models such as Maxwell, Kelvin-Voigt, and Zener, have limitations in modeling accurately the behavior of realistic viscoelastic materials as well as using the classical approach of the complex modulus to represent the dynamics of viscoelastic materials is limited to frequency domain analysis. Golla-Hughes and MacTavish (1985) used a Laplace-domain model called *GHM* Model of the complex modulus in which parameters are determined by curve-fitting to experimental data which makes it easy to formulate Finite elements by retaining the familiar second order differential equations, constant coefficient form, at the expense of some extra scalar degrees of freedom.

3.1.1 Golla-Hughes-McTavish (*GHM*) Model

The Golla-Hughes-MacTavish (*GHM*) model describes the shear modulus of viscoelastic materials with a second order differential equation unlike the first order differential equations used to describe the Maxwell, Kelvin-Voigt, and Zener models. Such a distinction makes it easy to incorporate the dynamics of the viscoelastic materials into finite element models of vibrating structures. Such integration is essential to the prediction of the response of these structures both in the time and frequency domains. This enables the computation of the structural response to transient, shock, as well as sinusoidal loading.

According to the *GHM* formulation, the shear modulus *G* of viscoelastic materials can be written in Laplace domain as

$$G(s) = G_0 \left[1 + \sum_{n=1}^{N} \alpha_n \frac{s^2 + 2\xi_n \omega_n s}{s^2 + 2\xi_n \omega_n s + \omega_n^2}\right] \tag{3.1}$$

This corresponds to the time-domain relaxation function as

$$G(t) = G_0 \left[1 + \sum_{n=1}^{N} \alpha_n \frac{b_{2k}\, e^{-b_{1k}t} - b_{1k}\, e^{-b_{2k}t}}{b_{2k} - b_{1k}}\right] \tag{3.2}$$

where
$$b_{1k}, b_{2k} = \omega_n \left[\pm\sqrt{\xi_n{}^2 - 1}\right] \tag{3.3}$$

G_0 =Equilibrium value of the modulus,

i.e., the final value of $G(\omega = \infty)$ and s is the Laplace domain variable.

The parameters $\alpha_n, \xi_n, \omega_n$are obtained from curve fitting the complex modulus data for a particular viscoelastic material at a given temperature. The summation may be thought of as representing the material modulus as a series of mini-oscillators (second order equations) as suggested by Golla and Hughes. These terms are representations of the internal variables necessary to describe the characteristics of the viscoelastic materials. The number of terms kept in the expansion is determined by accuracy needed to replicate the real behavior of the material and in many cases only two to four terms are necessary.

3.1.2 Motivation of the *GHM* Model

Consider a viscoelastic material described by one mini-oscillator (*i.e. n*=1) which is coupled with a mass such that the equation of motion in the Laplace domain is

$$Ms^2X(s) + K(s)X(s) = 0 \tag{3.4}$$

where *M* = mass, *K* = complex stiffness of the *VEM*

Equation (3.4) can be written as

$$Ms^2X(s) + \bar{K}\left[1 + \alpha_n \frac{s^2+2\xi_n\omega_n s}{s^2+2\xi_n\omega_n s+\omega_n^2}\right] X(s) = 0 \tag{3.5}$$

Let

$$z = \frac{{\omega_n}^2}{s^2+2\xi_n\omega_n s+\omega_n^2} x \tag{3.6}$$

Then, in the time domain, the Equation (3.6) reduces to

$$\ddot{z} + 2\xi_n\omega_n\dot{z} = {\omega_n}^2(x - z) \tag{3.7}$$

Substituting equation (3.7) into equation (3.5) gives equation of motion:

$$Ms^2x + \bar{K}x + \bar{K}\alpha_n\left[\frac{s^2+2\xi_n\omega_n s}{\omega_n^2}\right] z = 0 \tag{3.8}$$

In the time domain:

$$M\ddot{x} + \bar{K}x + \bar{K}\alpha_n\omega_n^2\left[\frac{x - z}{\omega_n^2}\right] = 0 \tag{3.9}$$

Equation (3.9) reduces to structural degrees of freedom,

$$M\ddot{x} + x(\bar{K} + \bar{K}\alpha) - \bar{K}\alpha z = 0 \tag{3.10}$$

Rewriting Equation (3.7) as follows *VEM 1 DOF:*

$$\ddot{z} - {\omega_n}^2x + 2\xi_n\omega_n\dot{z} + {\omega_n}^2z = 0 \tag{3.11}$$

Combining Equations (3.10) and (3.11) in a matrix form, gives

$$\begin{bmatrix} M & 0 \\ 0 & 1 \end{bmatrix}\begin{Bmatrix} \ddot{x} \\ \ddot{z} \end{Bmatrix} + \begin{bmatrix} 0 & 0 \\ 0 & 2\xi_n\omega_n \end{bmatrix}\begin{Bmatrix} \dot{x} \\ \dot{z} \end{Bmatrix} + \begin{bmatrix} \bar{K} + \bar{K}\alpha_n & -\bar{K}\alpha_n \\ -{\omega_n}^2 & {\omega_n}^2 \end{bmatrix}\begin{Bmatrix} x \\ z \end{Bmatrix} = 0 \tag{3.12}$$

Equation (3.12) has asymmetric stiffness matrix. However, by multiplying last row by $\bar{K}\frac{\alpha_n}{\omega_n^2}$, makes the stiffness matrix symmetric and as follows:

$$\begin{bmatrix} M & 0 \\ 0 & \bar{K}\frac{\alpha_n}{\omega_n^2} \end{bmatrix}\begin{Bmatrix} \ddot{x} \\ \ddot{z} \end{Bmatrix} + \begin{bmatrix} 0 & 0 \\ 0 & \frac{2\bar{K}\xi_n\alpha_n}{\omega_n} \end{bmatrix}\begin{Bmatrix} \dot{x} \\ \dot{z} \end{Bmatrix} + \begin{bmatrix} \bar{K}+\bar{K}\alpha_n & -\bar{K}\alpha_n \\ -\bar{K}\alpha_n & \bar{K}\alpha_n \end{bmatrix}\begin{Bmatrix} x \\ z \end{Bmatrix} = 0 \qquad (3.13)$$

Equation (3.13) governs the dynamics of the mechanical system shown in Figure 3.1. Hence, the viscoelastic material is represented by a spring-mass-damper assembly which is connected in parallel with another spring $\bar{K}$. Note that $\bar{K}$ from Equation (3.5), represents the stiffness of the viscoelastic material under static conditions (*i.e.* at zero frequency ω).

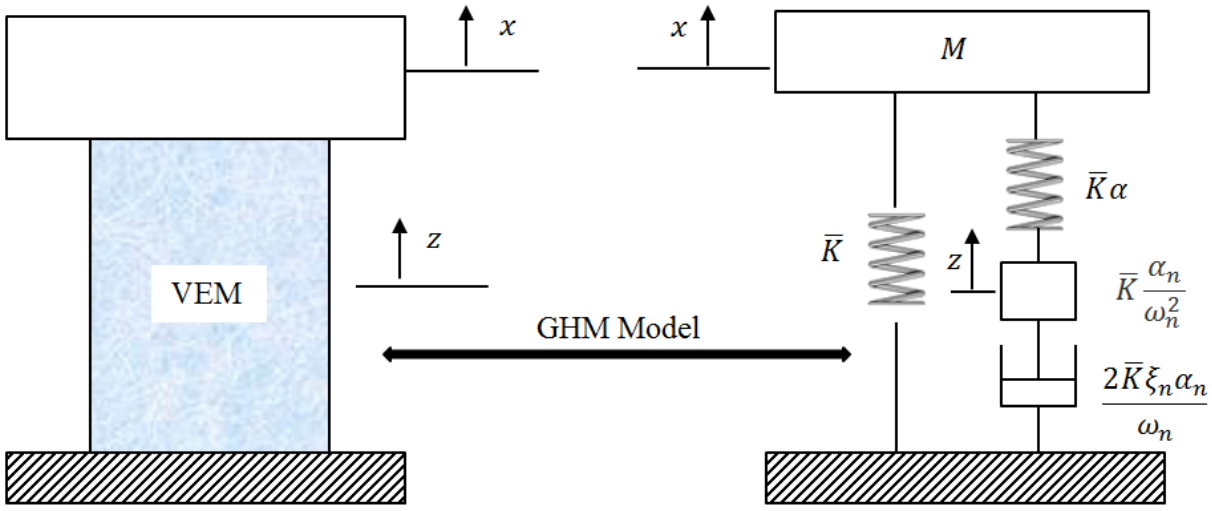

Figure 3.1: Equivalent system of the *GHM* Model

It is important here to note that *z* defines an "internal degree of freedom" (IDOF) which describes the motion of a *VEM* modeled by a single mini-oscillator. More *IDOF*s would be added when the *VEM* is modeled by *N* mini-oscillators. The addition of these damping *IDOF*s increases the size of the equations of motion of the structure considerably. Application of classical model

reduction techniques, such as Gaussian reduction, is essential to reduce the size of the structure/*VEM* model to include only the structural degrees of freedom in order to enhance the computational efficiency.

For a *VEM* which is modeled with *N* mini-oscillator, the equivalent mechanical system will be as shown in Figure 3.2.

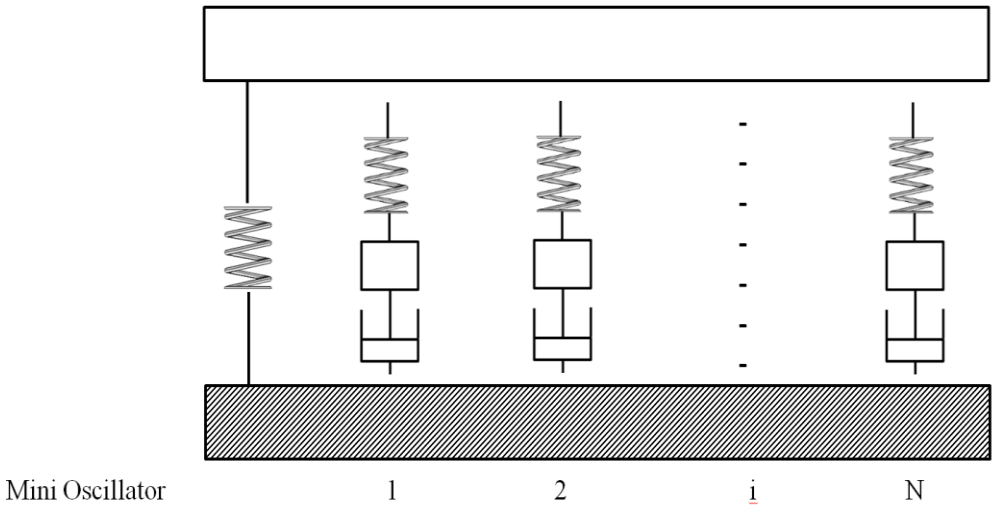

Figure 3.2: *GHM* model with N mini-oscillators

Accordingly, the equations governing a model with *N* mini-oscillators are given by:

$$Ms^2x + \bar{K}\left[1 + \alpha_1 \frac{s^2+2\xi_1\omega_1 s}{s^2+2\xi_1\omega_1 s+\omega_1^2} + \alpha_2 \frac{s^2+2\xi_2\omega_2 s}{s^2+2\xi_2\omega_2 s+\omega_2^2} + \cdots \ldots \ldots \ldots .\right] x = 0 \qquad (3.14)$$

$$\text{Let } z_1 = \frac{\omega_1^2}{s^2+2\xi_1\omega_1 s+\omega_1^2} x;\ z_2 = \frac{\omega_2^2}{s^2+2\xi_1\omega_2 s+\omega_2^2} x; \qquad (3.15)$$

Then, in matrix form with force F:

$$\begin{bmatrix} M & 0 & 0 & \dots & 0 \\ 0 & \bar{K}\frac{\alpha_1}{\omega_1^2} & 0 & \dots & 0 \\ 0 & 0 & \bar{K}\frac{\alpha_2}{\omega_2^2} & \dots & 0 \\ \dots & \dots & \dots & \dots & \dots \\ 0 & 0 & 0 & \dots & \bar{K}\frac{\alpha_N}{\omega_N^2} \end{bmatrix} \begin{Bmatrix} \ddot{x} \\ \ddot{z}_1 \\ \ddot{z}_2 \\ \dots \\ \ddot{z}_N \end{Bmatrix} +$$

$$\begin{bmatrix} 0 & 0 & 0 & \dots & 0 \\ 0 & \frac{2\bar{K}\xi_1\alpha_1}{\omega_1} & 0 & \dots & 0 \\ 0 & 0 & \frac{2\bar{K}\xi_2\alpha_2}{\omega_2} & \dots & 0 \\ \dots & \dots & \dots & \dots & \dots \\ 0 & 0 & 0 & \dots & \frac{2\bar{K}\xi_N\alpha_N}{\omega_N} \end{bmatrix} \begin{Bmatrix} \dot{x} \\ \dot{z}_1 \\ \dot{z}_2 \\ \dots \\ \dot{z}_N \end{Bmatrix} + \tag{3.16}$$

$$\begin{bmatrix} \bar{K}(1+\alpha_1+\alpha_2+\cdots) & -\bar{K}\alpha_1 & -\bar{K}\alpha_2 & \dots & -\bar{K}\alpha_N \\ -\bar{K}\alpha_1 & -\bar{K}\alpha_1 & 0 & \dots & 0 \\ -\bar{K}\alpha_2 & 0 & -\bar{K}\alpha_2 & \dots & 0 \\ \dots & \dots & \dots & \dots & \dots \\ -\bar{K}\alpha_N & 0 & 0 & 0 & -\bar{K}\alpha_N \end{bmatrix} \begin{Bmatrix} x \\ z_1 \\ z_2 \\ \dots \\ z_N \end{Bmatrix} = \begin{Bmatrix} F \\ 0 \\ 0 \\ \dots \\ 0 \end{Bmatrix}$$

3.1.3 Computation of the Parameters of the *GHM* Mini-Oscillators

The parameters $G_0\,, \alpha_{n,}, \xi_n \; and \; \omega_n$ of the *GHM* mini-oscillators are determined in such a way that replicates closely the experimental behavior of actual *VEM*. The optimal values of these parameters are selected, on a rational basis, in order to minimize the deviations between the predictions of the *GHM* model and the experimental data. The optimization problem is formulated as follows

$$Determine\; G_0\,, \alpha_{n,}, \xi_n \; and \; \omega_n$$

$$To\; minimize, \bar{F} = \left[\left(\frac{G'_{GHM-}G'_{EXP}}{G'_{EXP}}\right)^2 + \left(\frac{\eta_{GHM-}\eta_{EXP}}{\eta_{EXP}}\right)^2\right]$$

Such that $G_0\,, \alpha_{n,}, \xi_n \; and \; \omega_n > 0$ and $G_\infty = G_0\,[1 + \sum_{n=1}^{N} \alpha_n]$

where $G_0 \; and \; G_\infty \; are \; the \; storage \; moduli \; of \; the \; VEM \; at \; \omega = \; 0 \; and \; \infty \; respectively,$

$$N = Number \; of \; GHM \; mini \; oscillators$$

In the above equation, the objective function $\bar{F}$ is formulated in order to minimize the sum of the prediction error of the *GHM* model of both the storage modulus and the loss factor as computed over the entire experimental frequency range. The errors are cast in a normalized and quadratic form in order to make the optimization problem well-conditioned. Furthermore, constraints are imposed to guarantee that the parameters are all nonnegative and that the model can predict the storage modulus at large frequencies. Figure 3.3 outlined the flow chart of the optimization process.

Optimization Algorithms:

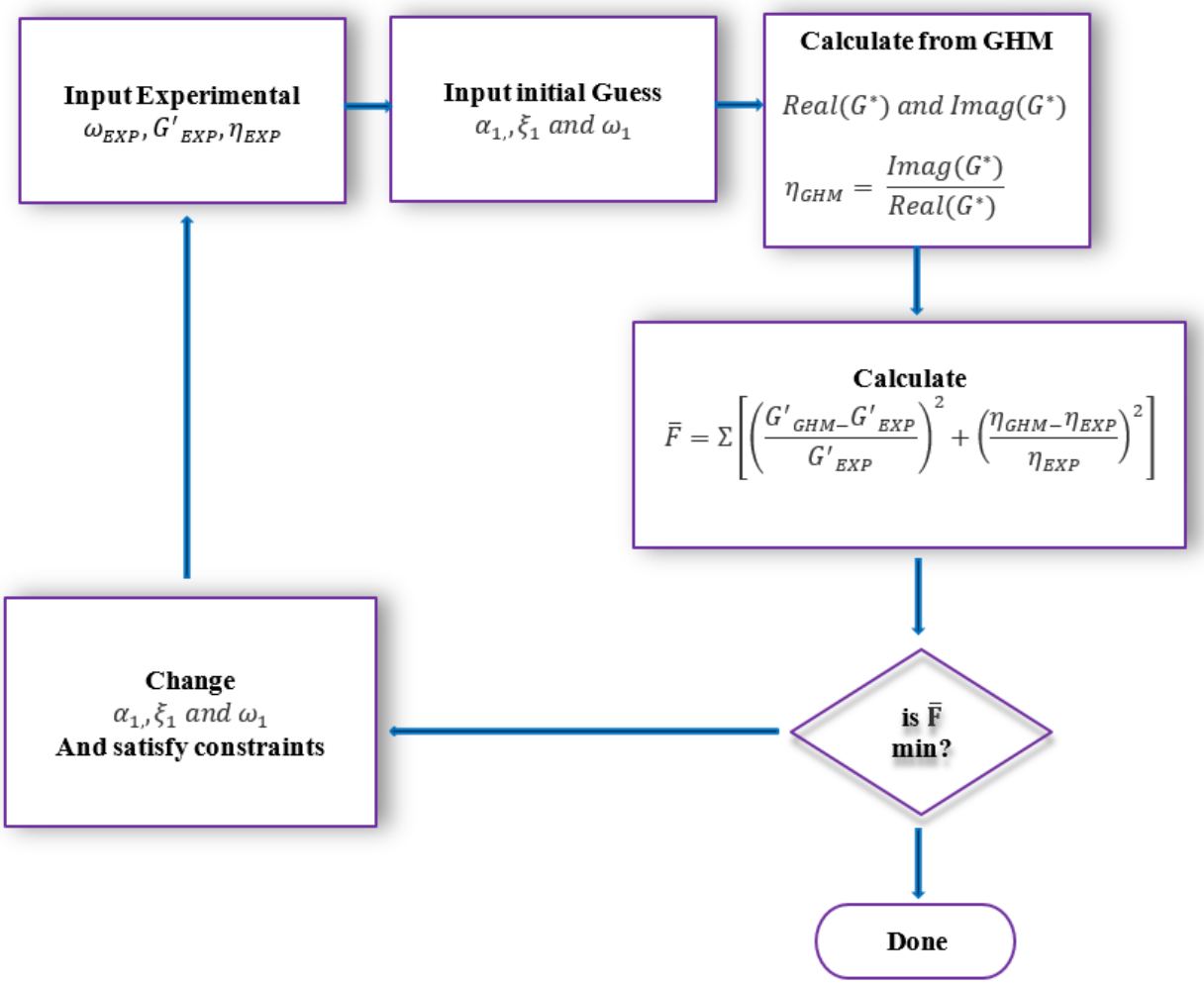

Figure 3.3: Flowchart of the optimal selection of the *GHM* parameters

3.2 *FEM* Derivation of the Rod treated with *VEM*

Figure 3.4 illustrates a Stainless Steel (Structure) rod treated with unconstrained *VEM* Polyurea layer. The structure /*VEM* is modeled by *N* one-dimensional finite elements. Each element is bounded by two nodes and each node has a single degree of freedom which is the longitudinal deflection *u*.

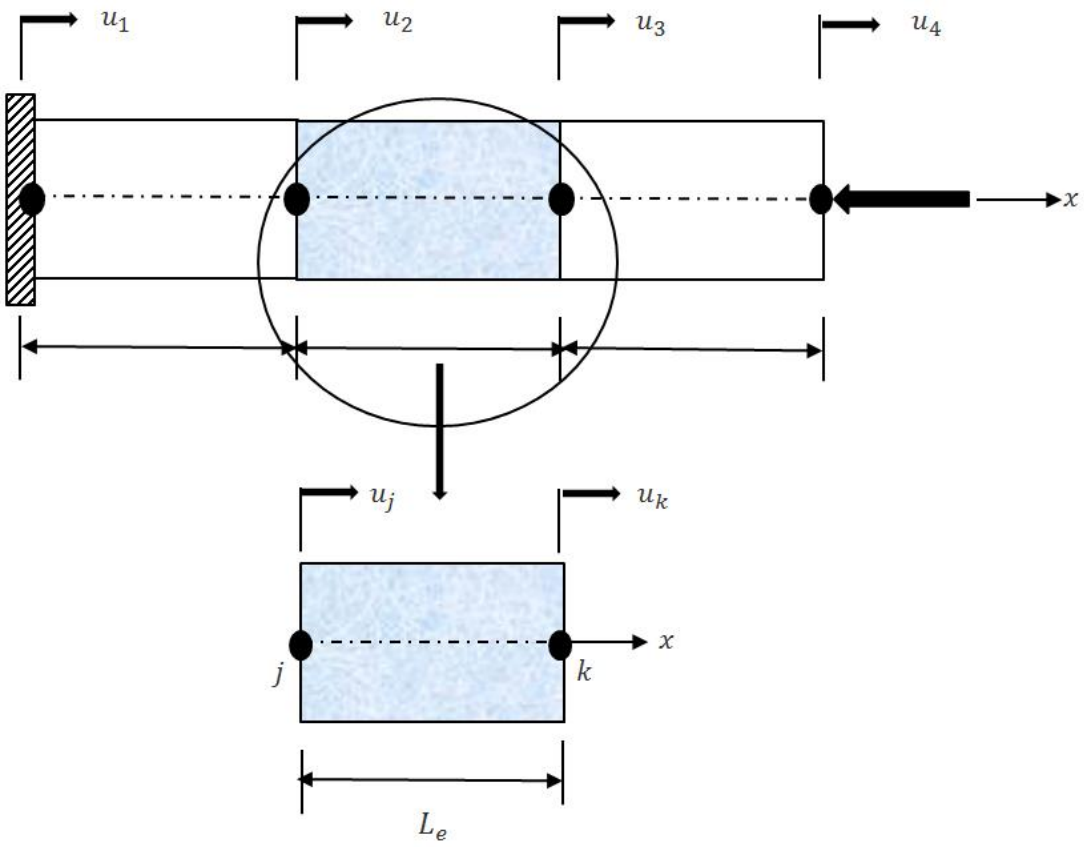

Figure 3.4: Finite element model the rod/unconstrained *VEM* assembly

Assumptions:

- Displacements and forces are measurable only at its two ends
- Rods experience longitudinal vibrations only

- All forces and displacements are axial
- Uniform cross-sectional area A^e
- Spatially uniform stress σ^e
- Linearly elastic solid with modulus E^e
- infinitesimal strains over the length L^e

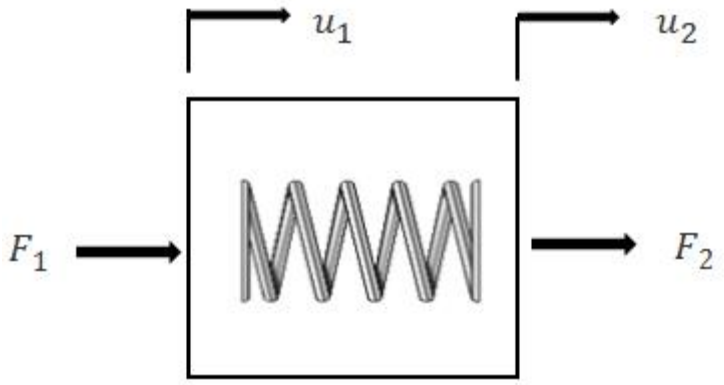

Figure 3.5: Free body diagram of forces acting on a spring

The spring forces and associated deflections as shown in Figure (3.5) are related by the following expressions:

$$F_1 = k(u_1 - u_2)$$

$$F_2 = k(u_2 - u_1)$$

For the spring to be in equilibrium (net force acting on it must be zero):

$$F_1 + F_2 = 0$$

Expressing the force balance with matrices and vectors:

$$\begin{Bmatrix} F_1 \end{Bmatrix} = k \begin{bmatrix} 1 & -1 \end{bmatrix} \begin{Bmatrix} u_1 \\ u_2 \end{Bmatrix} \tag{3.17}$$

$$\begin{Bmatrix} \\ F_2 \end{Bmatrix} = k \begin{bmatrix} & \\ -1 & 1 \end{bmatrix} \begin{Bmatrix} u_1 \\ u_2 \end{Bmatrix} \tag{3.18}$$

Combining Equations (3.17) and (3.18) yields:

$$\begin{Bmatrix} F_1 \\ F_2 \end{Bmatrix} = \begin{bmatrix} k_{11} & -k_{12} \\ -k_{21} & k_{22} \end{bmatrix} \begin{Bmatrix} u_1 \\ u_2 \end{Bmatrix} \tag{3.19}$$

$$\xrightarrow{yields} \{F^e\} = [k^e]\{u^e\}$$

$$\xrightarrow{yields} F_i^e = \sum_j k_{ij}^e \, u_j^e$$

The internal force in the Structure /*VEM* is given by,

$$F = \sigma^e A^e = E^e A^e \varepsilon^e \qquad \xrightarrow{yields} \qquad F = E^e A^e \left[\frac{u_2^e - u_1^e}{L^e}\right]$$

$$\xrightarrow{yields} \begin{Bmatrix} F_1^e \\ F_2^e \end{Bmatrix} = \frac{E^e A^e}{L^e} \begin{bmatrix} 1 & -1 \\ -1 & 1 \end{bmatrix} \begin{Bmatrix} u_1^e \\ u_2^e \end{Bmatrix}$$

This shows that $k = \frac{E^e A^e}{L^e}$.

Using a linear shape function, one can write the deflection *u* at any location *x*, in terms of the nodal deflection as follows:

$$u(x) = \sum_i^{nodes\ per\ element} N_i(x) u_i = \lceil N_1 \; N_2 \rceil \begin{Bmatrix} u_j \\ u_k \end{Bmatrix} = \lceil N \rceil \{\Delta_i\} \tag{3.20}$$

where $N_1(x) = 1 - \frac{x}{L}$ *and* $N_2(x) = \frac{x}{L}$ are interpolating vector

$$\{\Delta_i\} = \{u_j \; u_k\}^T \; ar\ nodal\ deflection\ vector\ of\ i^{th}\ Element$$

$$N_i(x_j) = \delta_{ij} = \begin{cases} 1, & i = j \\ 0, & i \neq j \end{cases}$$

Now, the Potential Energy is given by:

$$P.E = P.E_{structure} + P.E_{VEM} = \frac{1}{2}\int_0^{L_{es}} E_s A_s\, u_x^2 dx + \frac{1}{2}\int_0^{L_{ev}} E_v A_v\, u_x^2 dx \tag{3.21}$$

where, E_i and A_i are Young's modulus and the area of i^{th} layer with subscript *s* and *v* denoting the structure and the *VEM* respectively. Also, u_x denotes partial derivative of the deflection u with respect to *x*.

From equations (3.20) and (3.21), the potential energy reduces to

$$P.E = \frac{1}{2}\{\Delta_i\}^T \int_0^{L_{es}} E_s A_s \{\mathrm{N}_x\}^T\{\mathrm{N}_x\}dx\{\Delta_i\} + \frac{1}{2}\{\Delta_i\}^T \int_0^{L_{es}} E_v A_v \{\mathrm{N}_x\}^T\{\mathrm{N}_x\}dx\{\Delta_i\}$$

$$\xrightarrow{yields} = \frac{1}{2}\{\Delta_i\}^T E_s A_s \int_0^{L_e} \{\mathrm{N}_x\}^T \{\mathrm{N}_x\}dx\{\Delta_i\} + \frac{1}{2}\{\Delta_i\}^T E_v A_v \int_0^{L_e} \{\mathrm{N}_x\}^T \{\mathrm{N}_x\}dx\{\Delta_i\}$$

$$P.E = \frac{1}{2}\{\Delta_i\}^T [E_s A_s + E_v A_v] \int_0^{L_e} \{\mathrm{N}_x\}^T \{\mathrm{N}_x\}dx\{\Delta_i\} = \frac{1}{2}\{\Delta_i\}^T [K_s + K_v]\{\Delta_i\} \tag{3.22}$$

where

$$[K_s] = E_s A_s \int_0^{L_{eAl}} \{\mathrm{N}_x\}^T \{\mathrm{N}_x\}dx = \frac{E_s A_s}{L^{es}} \begin{bmatrix} 1 & -1 \\ -1 & 1 \end{bmatrix} \; and$$

$$[K_v] = E_v A_v \int_0^{L_{es}} \{\mathrm{N}_x\}^T \{\mathrm{N}_x\}dx = \frac{E_v A_v}{L^{ev}} \begin{bmatrix} 1 & -1 \\ -1 & 1 \end{bmatrix} \tag{3.23}$$

where $[K_s]$ and $[K_v]$ denote structural (steel) stiffness matrix (Real) and *VEM* stiffness matrix (Complex) as represented by the *GHM* model. Also, in equation (3.22), $\{\mathrm{N_x}\}$ denotes the partial derivative of $\{N\}$with respect to *x*.

Similarly, the Kinetic Energy:

$$K.E = K.E_{structure} + K.E_{vem} = \frac{1}{2}\int_0^{L_e} (\rho_s A_s + \rho_v A_v)\,\dot{u}^2 dx \tag{3.24}$$

where ρ_s *and* ρ_v denote the density of the structure and the *VEM* respectively.

But as, $u(x) = [N]\{\Delta_i\}$, then, $\dot{u}(x) = [N]\{\dot{\Delta}_i\}$ and equation (3.24) reduces to:

$$K.E_{structure} = \frac{1}{2}\{\dot{\Delta}_i\}^T(\rho_s A_s + \rho_v A_v)\int_0^{L_e} \{\mathrm{N}_x\}^T\{\mathrm{N}_x\}dx\{\dot{\Delta}_i\} = \frac{1}{2}\{\dot{\Delta}_i\}^T[M]\{\dot{\Delta}_i\} \tag{3.25}$$

where, $[M] = \frac{(\rho_s A_s + \rho_v A_v)L}{6}\begin{bmatrix} 2 & 1 \\ 1 & 2 \end{bmatrix}$ =mass matrix of the structure /*VEM* assembly.

From equations (3.22) and (3.25), the equation of motion of the element can be obtained using the Lagrangian dynamics as follows:

$$\frac{d}{dt}\left(\frac{\partial KE}{\partial\{\dot{\Delta}\}}\right) + \frac{\partial PE}{\partial\{\Delta_i\}} = \{\mathrm{F}_i\}$$

or
$$[M]s^2\{\Delta_i\} + [K_s + K_v]\{\Delta_i\} = \{\mathrm{F}_i\} \tag{3.26}$$

where, $\{\mathrm{F}_i\}$ is the vector of the forces acting on the i^{th}element

The equation of motion of the entire Structure /*VEM* system can then be determined by assembling the mass and stiffness matrices of the individual elements to yield:

$$[M_o]s^2\{\Delta\} + [K_{s_o} + K_{v_o}]\{\Delta\} = \{\mathrm{F}_o\} \tag{3.27}$$

where $[M_o]$, $\left[K_{s_o}\right]$ and $\left[K_{v_o}\right]$ are the overall mass matrix, overall structural stiffness matrix, and overall *VEM* stiffness matrix as below from Figure 3.4:

$$[M_o]s^2\{\Delta\} + [K_{s_o} + K_{v_o}]\{\Delta\} = \{\mathrm{F}_o\} \tag{3.28}$$

$$\text{Now, } [M_o] = M_{s_o}^{(1)} + M_v^{(2)} + M_{s_o}^{(3)}$$

$$[M_o] = \frac{(\rho_s A_s L_{e_s})}{6}\begin{bmatrix}2 & 1 & 0 & 0\\ 1 & 2 & 0 & 0\\ 0 & 0 & 0 & 0\\ 0 & 0 & 0 & 0\end{bmatrix} + \frac{(\rho_v A_v L_{e_v})}{6}\begin{bmatrix}0 & 0 & 0 & 0\\ 0 & 2 & 1 & 0\\ 0 & 1 & 2 & 0\\ 0 & 0 & 0 & 0\end{bmatrix} + \frac{(\rho_s A_s L_{e_s})}{6}\begin{bmatrix}0 & 0 & 0 & 0\\ 0 & 0 & 0 & 0\\ 0 & 0 & 2 & 1\\ 0 & 0 & 1 & 2\end{bmatrix} \tag{3.29}$$

where

$$[M_o] = \frac{(\rho_s A_s L_{e_s})}{6}\begin{bmatrix}\frac{(\rho_s A_s L_{e_s})}{3} & \frac{(\rho_s A_s L_{e_s})}{6} & 0 & 0\\ \frac{(\rho_s A_s L_{e_s})}{6} & \frac{1}{3}\left[(\rho_s A_s L_{e_s}) + (\rho_v A_v L_{e_v})\right] & \frac{(\rho_v A_v L_{e_v})}{6} & 0\\ 0 & \frac{(\rho_v A_v L_{e_v})}{6} & \frac{1}{3}\left[(\rho_s A_s L_{e_s}) + (\rho_v A_v L_{e_v})\right] & \frac{(\rho_s A_s L_{e_s})}{6}\\ 0 & 0 & \frac{(\rho_s A_s L_{e_s})}{6} & \frac{(\rho_s A_s L_{e_s})}{3}\end{bmatrix} \tag{3.30}$$

$$\left[K_{s_o}\right] = K_{s_o}^{(1)} + K_{s_o}^{(2)} + K_{s_o}^{(3)} = \frac{E_S A_S}{L_{e_S}}\begin{bmatrix}1 & -1 & 0 & 0\\ -1 & 1 & 0 & 0\\ 0 & 0 & 0 & 0\\ 0 & 0 & 0 & 0\end{bmatrix} + 0 + \frac{E_S A_S}{L_{e_S}}\begin{bmatrix}0 & 0 & 0 & 0\\ 0 & 0 & 0 & 0\\ 0 & 0 & 1 & -1\\ 0 & 0 & -1 & 1\end{bmatrix} \tag{3.31}$$

$$\left[K_{s_o}\right] = \frac{E_S A_S}{L_{e_S}}\begin{bmatrix}1 & -1 & 0 & 0\\ -1 & 1 & 0 & 0\\ 0 & 0 & 1 & -1\\ 0 & 0 & -1 & 1\end{bmatrix} \tag{3.32}$$

$$\left[K_{v_o}\right] = K_{v_o}^{(1)} + K_{v_o}^{(2)} + K_{v_o}^{(3)} = 0 + \frac{E_v A_v}{L_{e_v}}\begin{bmatrix}0 & -0 & 0 & 0\\ 0 & 1 & -1 & 0\\ 0 & -1 & 1 & 0\\ 0 & 0 & 0 & 0\end{bmatrix} + 0 = \frac{E_v A_v}{L_{e_v}}\begin{bmatrix}0 & -0 & 0 & 0\\ 0 & 1 & -1 & 0\\ 0 & -1 & 1 & 0\\ 0 & 0 & 0 & 0\end{bmatrix} \tag{3.33}$$

Also, $\{\Delta\}$ and $\{F_o\}$ denote the deflection and load vectors of the entire Structure /*VEM* assembly.

Before describing the $[K_{v_o}]$ in terms of the *GHM* model, the boundary conditions are imposed on the structure to eliminate the rigid body modes. This is essential because these modes do to not contribute any damping to the flexible body modes.

Introducing the *I-DOF z* to describe the dynamics of the *VEM*, and employing the approach outlined in Section 3.2.1, equation (3.6) reduces to:

$$[K_{v_o}] = E_{v_o} \left[1 + \alpha_1 \frac{s^2+2\xi_1\omega_1 s}{s^2+2\xi_1\omega_1 s+\omega_1^2}\right][\bar{K}_{v_o}] \tag{3.34}$$

Hence, equation (3.28) reduces to:

$$[M_T]\{\ddot{X}\} + [C_T]\{\dot{X}\} + [K_T]\{X\} = \{F_T\} \tag{3.35}$$

where,

$$[M_T] = \begin{bmatrix} [M_o] & [0] \\ [0] & \frac{\alpha_1 E_{v_o}[\bar{K}_{v_o}]}{\omega_1^2} \end{bmatrix};$$

$$[C_T] = \begin{bmatrix} [0] & [0] \\ [0] & \frac{2\xi_1\alpha_1 E_{v_o}[\bar{K}_{v_o}]}{\omega_1} \end{bmatrix};$$

$$[K_T] = \begin{bmatrix} [K_{s_o}] + E_{v_o}\,(1+\alpha_1)[\bar{K}_{v_o}] & -E_{v_o}\alpha_1\,[\bar{K}_{v_o}] \\ -E_{v_o}\alpha_1\,[\bar{K}_{v_o}] & E_{v_o}\alpha_1\,[\bar{K}_{v_o}] \end{bmatrix};$$

$$\{X\} = \begin{Bmatrix} \Delta \\ z \end{Bmatrix};$$

$$\{F_T\} = \begin{Bmatrix} \mathrm{F}_o \\ 0 \end{Bmatrix};$$

If the matrix $[\bar{K}_{v_o}]$ remains singular, then introduce the following transformation of the z *to* $\bar{z}$ IDOF such that $z = \mathrm{R}_n\bar{z}$ where, R_n is the eigenvector matrix of the non-zero eigenvalues Λ of $[\bar{K}_{v_o}]$ such that $[\bar{K}_{v_o}] = \mathrm{R}_n\Lambda R^T{}_n$ with $R_n^T\mathrm{R}_n = I$ $[\bar{K}_{v_o}]$ can also be written as:

$$[\bar{K}_{v_o}] = \mathrm{R}_n\Lambda R_n^T = [\mathrm{R}_o\ \mathrm{R}_n]\begin{bmatrix} 0 & 0 \\ 0 & \Lambda \end{bmatrix}\begin{bmatrix} R_o^T \\ R_n^T \end{bmatrix} \tag{3.36}$$

where, $R^T = \ total\ eigenvector\ matrix\ of\ [\overline{K}_{v_o}]$

which includes the eigenvector matrices for the zero and non-zero eigenvalues R_o and R_n respectively.

This yield,

$$[M_T] = \begin{bmatrix} [M_o] & [0] \\ [0] & \frac{\alpha_1 E_{v_o} \Lambda}{\omega_1^2} \end{bmatrix};$$

$$[C_T] = \begin{bmatrix} [0] & [0] \\ [0] & \frac{2\xi_1 \alpha_1 E_{v_o} \Lambda}{\omega_1} \end{bmatrix};$$

$$[K_T] = \begin{bmatrix} [K_{s_o}] + E_{v_o}\ (1+\alpha_1)[\overline{K}_{v_o}] & -E_{v_o}\alpha_1\ R_n\ \Lambda \\ -E_{v_o}\alpha_1\ \Lambda R_n^T & E_{v_o}\alpha_1\ \Lambda \end{bmatrix};$$

$$\{X\} = \begin{Bmatrix} \Delta \\ \bar{Z} \end{Bmatrix}; \qquad \text{and} \qquad \{F_T\} = \begin{Bmatrix} \mathrm{F}_o \\ 0 \end{Bmatrix}; \tag{3.37}$$

The time and frequency responses of the full order Structure/*VEM* systems can be computed from Equation (3.35). Furthermore, the natural frequencies and corresponding damping ratios can be determined by casting the homogenous parts of the two equations in a state-space.

3.3 Characterization results through *FEM/MATLAB* and *ANSYS*

3.3.1 Material Properties

The finite element model (*FEM*) developed in section 3.2 is now used to predict the dynamic behavior of the polyurea composites for different layering configurations and levels of

strain rates. The main physical and geometrical parameters of the *SHPB*, polyurea, and the inserts used to form the polyurea composite are listed in Table 3.1.

Table 3. 1: Geometric and structural properties of incident bar, transmitted bar and polyurea specimen

Geometric Specifications	**Value**
Length of Incident bar (LT_i)	1.75 m
Length of Transmitted bar (LT_t)	1.75 m
Length of PU sample (LT_s)	0.0033 m
Length of AL sample (LT_a)	0.000711 m
Diameter of Incident bar (Di)	0.0125 m
Diameter of Transmitted bar (Dt)	0.0125 m
Diameter of circular sample (Ds)	0.0125 m
Structural Properties	**Value**
Young's Modulus of Stainless steel (Ess)	200E9 Pa
Young's Modulus of Aluminum (Eal)	70E9 Pa
Young's Modulus of Polyurea (Ev)	15.3E6 Pa
Density of Stainless steel (ρ_{ss})	7700 kg/m^3
Density of Aluminum (ρ_{al})	2700 kg/m^3
Density of Polyurea (ρ_v)	1100 kg/m^3
Mass of Stainless steel (m_{ss})	0.9449 kg/m
Mass of Aluminum (m_{al})	0.3313 kg/m
Mass of Polyurea (m_v)	0.1350 $kg/$

Figure 3.6 shows the storage modulus and the loss factor of the polyurea at different temperatures and frequencies by Nouh *et al.* [31].

Table 3.2 lists the main parameters of the corresponding Generalized Maxwell model that models the viscoelastic behavior of the polyurea.

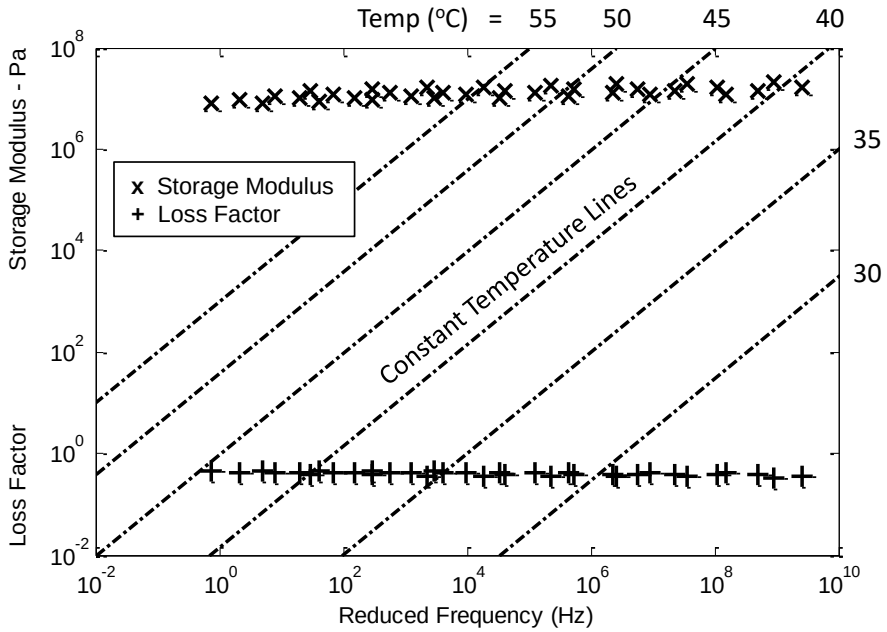

(a)

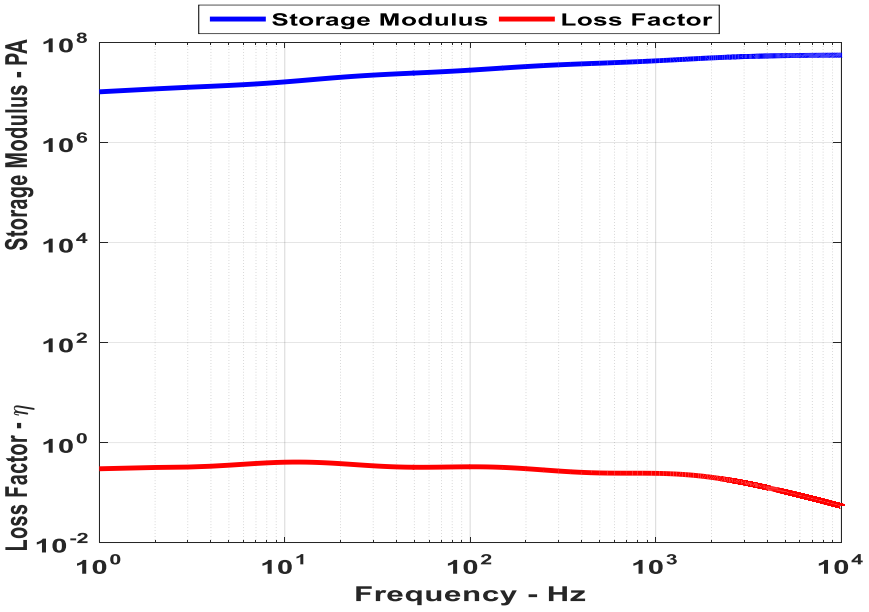

(b)

Figure 3.6: Storage Modulus and Loss Factor of polyurea at different temperatures and frequencies [(a) – experimental, (b) – Generalized Maxwell Model]

Mathematically, the *VEM* is represented by the following Generalized Maxwell model, in the time domain, as follows:

$$E(t) = E_0\left[1+\sum_{i=1}^{n}\alpha_i e^{-t/\rho_i}\right] \tag{3.38}$$

where E_0 = the equilibrium modulus, α_i = the i^{th} relative modulus, and ρ_i = the i^{th} relaxation times = η_i / E_i. Note that E_0, α_i, and ρ_i are all positive constants. Also, the summation term $\sum_{i=1}^{n}\alpha_i e^{-t/\rho_i}$ is designated as the "*Relaxation Kernel*".

In the frequency domain, equation (3.38) reduces to:

$$E^*(s) = E_0\left[1+\sum_{i=1}^{n}\alpha_i \frac{\rho_i s}{\rho_i s+1}\right] \tag{3.39}$$

where s is the Laplace complex variable. It can be seen that E_0 is the limiting value of $E(t)$ which is attained at $t = \infty$ when the *VEM* is totally relaxed. Equivalently E_0 is attained when the *VEM* operates under static conditions at $\omega = 0$.

Also, at time $t = 0$ or $\omega = \infty$, the relaxation modulus assumes a value E_∞ given by:

$$E_\infty = E_0\left[1+\sum_{i=1}^{n}\alpha_i\right] \tag{3.40}$$

where E_∞ denotes the instantaneous modulus.

$$E^*(s) = E_\infty\left[\beta_\infty+\sum_{i=1}^{n}\beta_i \frac{\rho_i s}{\rho_i s+1}\right] \tag{3.41}$$

Also, E_∞ defines the limiting value of $E(t)$ which is attained at $t = 0$ with $\beta_\infty + \sum_{i=1}^{n}\beta_i = 1$. Equivalently E_∞ is attained when the *VEM* operates at very high frequency such that $\omega = \infty$.

The relative moduli α_i and β_i are related by the following expressions:

$$\beta_\infty = E_0 / E_\infty \quad \text{and} \quad \beta_i = (E_0 / E_\infty)\ \alpha_i \tag{3.42}$$

The alternative form of the *GMM*, given by equation (3.41), is used in most of the commercial finite element codes, such as *ANSYS*, to express the behavior of the *VEM*.

Table 3.2: Parameters of the Generalized Maxwell Model (*GMM*)

($E_\infty = 1MPa$, $\beta_\infty = 0.0178$)

Term	1	2	3	4	5	6	7	8
β_i	0.3203	0.2491	0.1957	0.0712	0.0534	0.0427	0.0320	0.0178
ρ_i (s)	1E-4	1E-3	1E-2	1E-1	1E-0	1E1	1E2	1E3

Figure 3.7 shows the storage modulus and the loss factor of the polyurea at different temperatures and frequencies by Al Supie [32].

Table 3.3 lists the main parameters of the corresponding *GHM* model with one mini-oscillators that models the viscoelasticity of the polyurea.

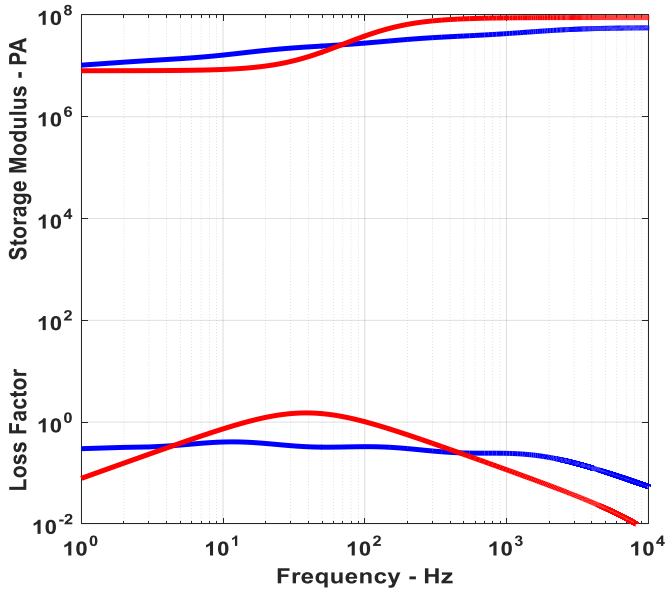

Figure 3.7: Storage Modulus and the Loss Factor of polyurea at different frequencies

(— Generalized Maxwell Model, — *GHM*)

Table 3. 2: Parameters of the Golla-Hughes-McTavish (GHM) with a single mini-oscillator

Geometric Specifications	Value
ω_1	8,000 *rad/s*
ζ_1	5
α_1	10

3.3.2. Dynamic Behavior of the Polyurea Composites

In this section, three configurations of the polyurea composites are considered. These configurations are displayed in Figure 3.8. These configurations are 1 layer of polyurea (Figure 3.8(a)), 2 layers of polyurea sandwiching an aluminum layer (Figure 3.8(b)), and 3 layers of polyurea sandwiching two aluminum layers (Figure 3.8(c)).

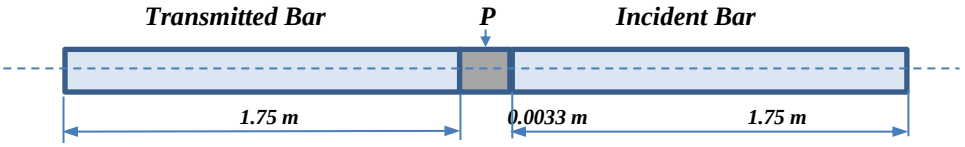

(a) - 1 layer of polyurea

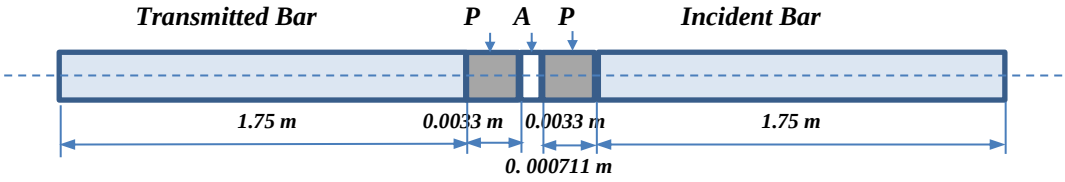

(b) – 2 Layers Polyurea/1 Layer Aluminum

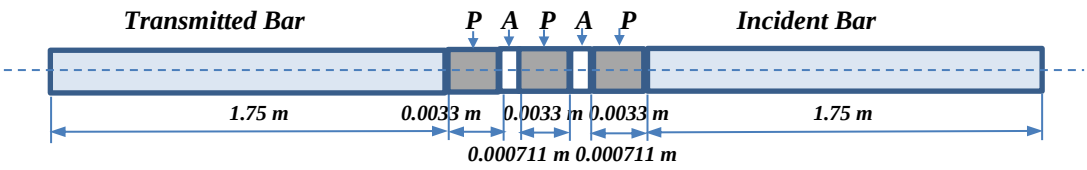

(c) – 3 Layers Polyurea/2 Layers Aluminum

Figure 3.8: Different configurations of the polyurea composites

[*P* = Polyurea (0.0033 m thick), *A* = Aluminum (0.00071 m thick)]

A. MATLAB

Configuration 1 (One Polyurea Layer)

Figure 3.9 displays the stress and strain characteristics of configuration 1. Figure 3.9(a) shows the time histories of the incident and reflected strains as well as that of the transmitted strain. The calculated equivalent strain and stress of the polyurea layer are shown in Figure 3.9(b). These characteristics are used to plot the stress-strain behavior of the polyurea as shown in Figure 3.9c.

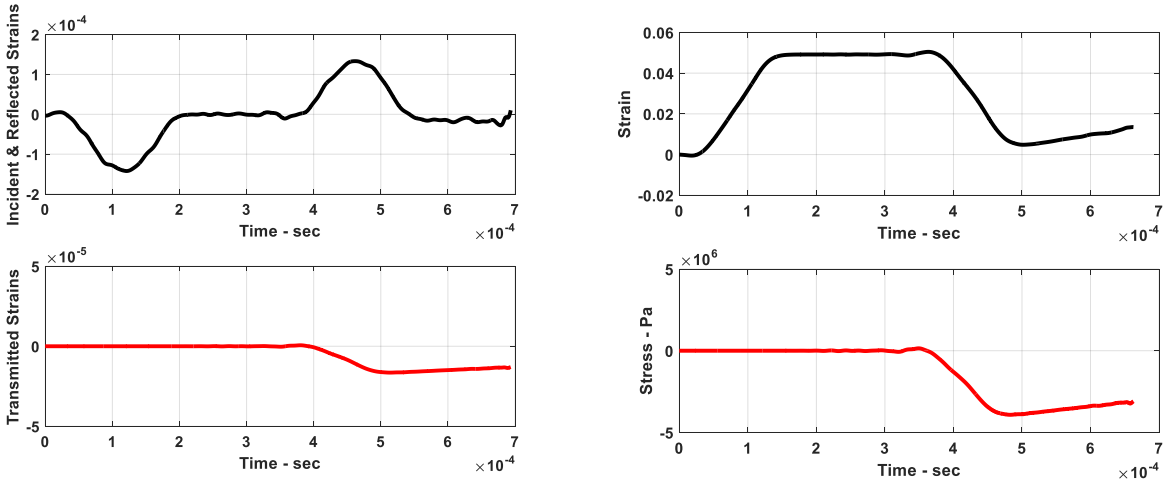

(a) (b)

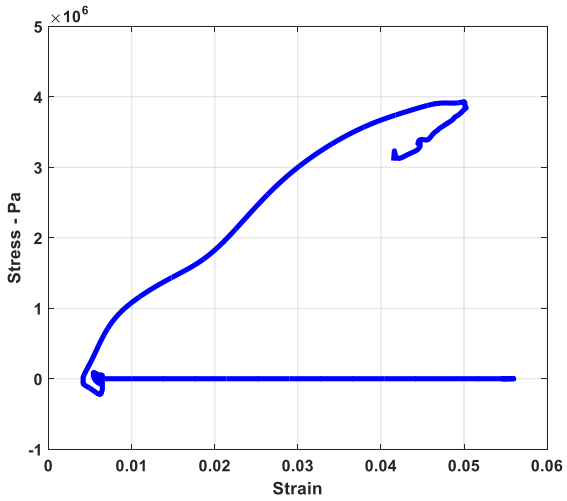

(c)

Figure 3.9: Stress and Strain characteristics of Configuration 1 of the polyurea composites

Configuration 2 (Two Polyurea Layers/One Aluminum Layer)

Figure 3.10 displays the stress and strain characteristics of configuration 2. Figure 3.10(a) shows the time histories of the incident and reflected strains as well as that of the transmitted strain. The calculated equivalent strain and stress of the polyurea layer are shown in Figure 3.10(b). These characteristics are used to plot the stress-strain behavior of the polyurea as shown in Figure 3.10(c).

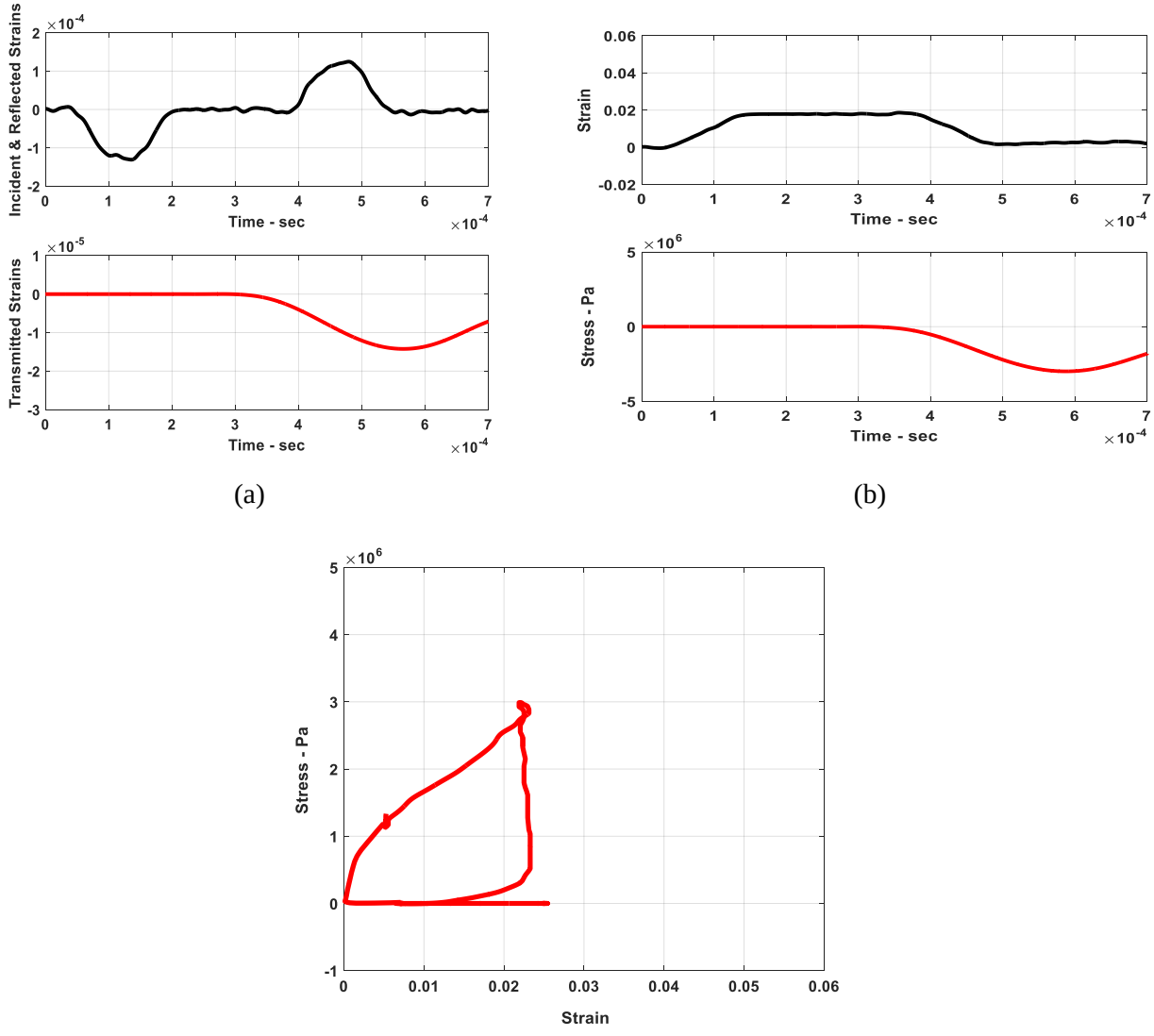

(a)

(b)

(c)

Figure 3.10: Stress and Strain characteristics of Configuration 2 of the polyurea composites

Configuration 3 (Three Polyurea Layers/Two Aluminum Layer)

Figure 3.11 displays the stress and strain characteristics of configuration 3. Figure 3.11(a) shows the time histories of the incident and reflected strains as well as that of the transmitted strain. The calculated equivalent strain and stress of the polyurea layer are shown in Figure 3.11(b). These characteristics are used to plot the stress-strain behavior of the polyurea as shown in Figure 3.11(c).

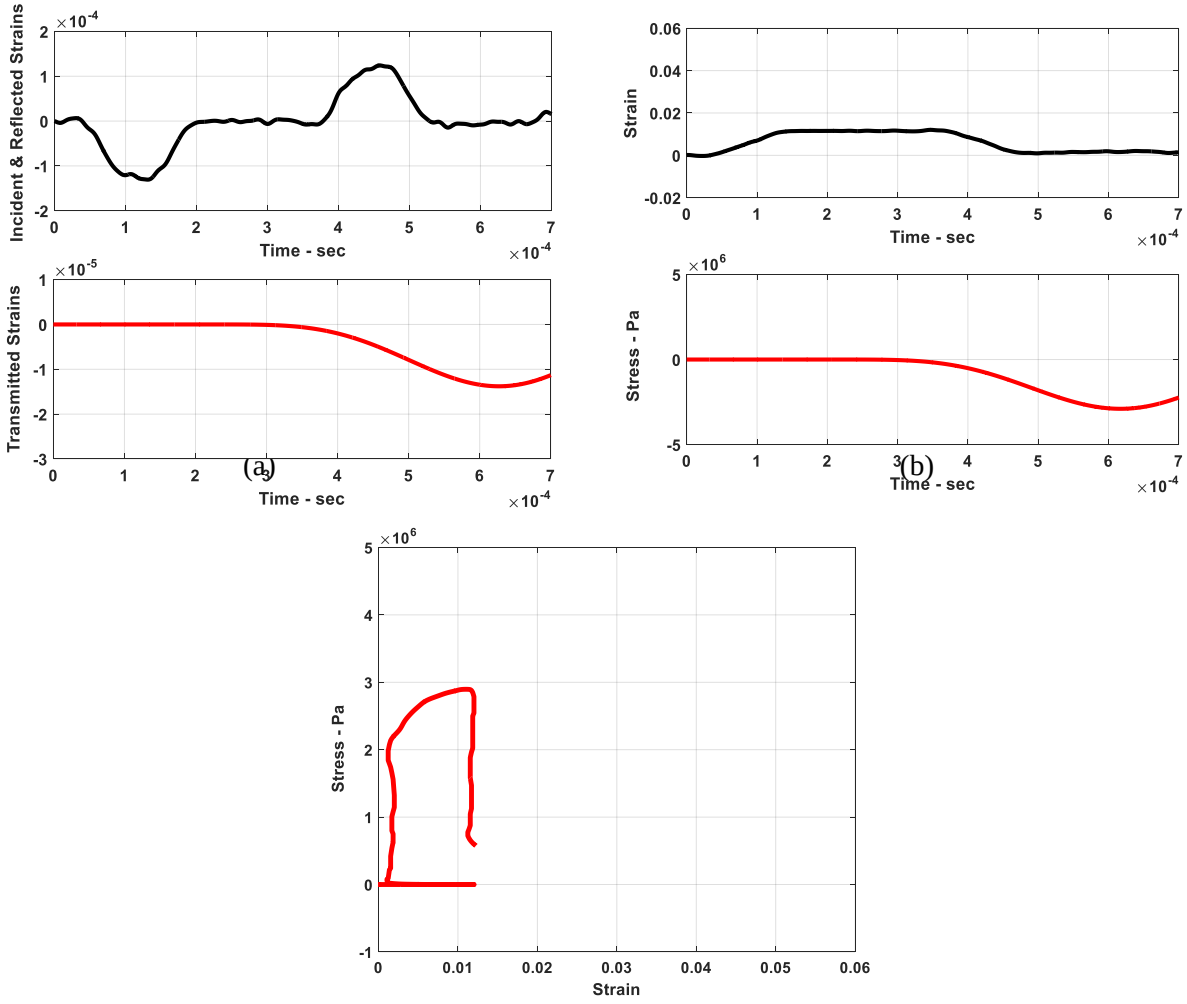

Figure 3.11: Stress and Strain characteristics of Configuration 3 of the polyurea composites

B. ANSYS

i. Model

Figures 3.12 and 3.13 display the finite element meshes of the *ANSYS* models of configurations 1 and 3. In the development of these models, axisymmetric plane elements 183 are used. These elements are higher order 2-D elements with 8 nodes with each node has two in-plane degrees of freedom (u_x and u_y). Note that the x direction is perpendicular to the longitudinal axis y of the incident and transmit bars as shown in Figures 3.12 and 3.13.

In the analysis, the deflections of the incident and transmit bars are limited only along the y direction. Hence, all the DOF's along the x direction are constrained. Furthermore, the transmit bar is assumed to be fixed at its end which is located opposite to the impact end of the incident bar. The incident bar is assumed free to move.

The incident bar is divided into 350 elements and so is the transmit bar. Each of the polyurea layers is divided into 4 elements whereas the aluminum layer is divided 1 element.

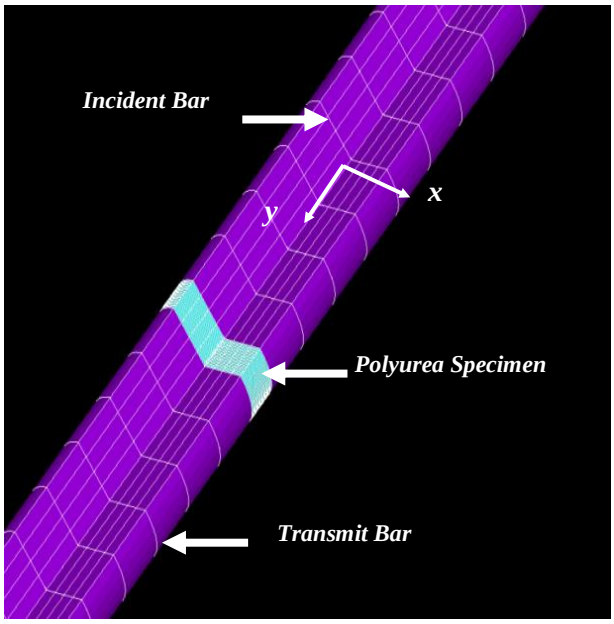

Figure 3.12: ANSYS Finite Element Model of Configuration 1 of the polyurea composites

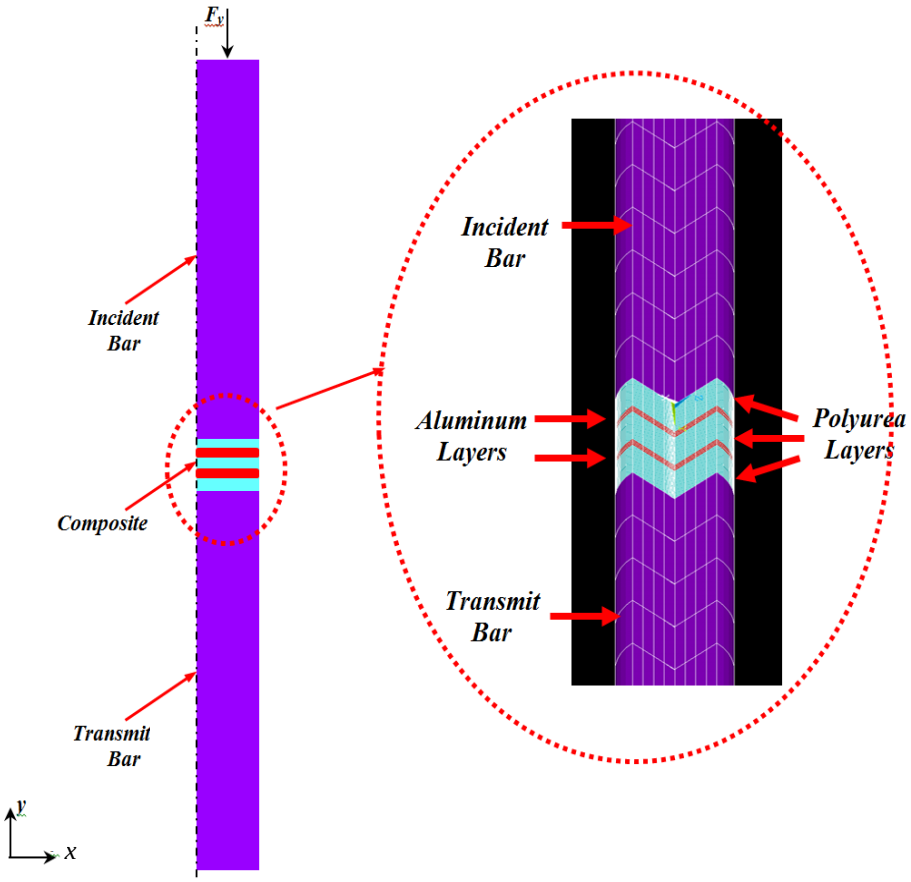

Figure 3.13: ANSYS Finite Element Model of Configuration 3 of the polyurea composites

ii. Stress-Strain Characteristics

Configuration 1 (one Polyurea Layer)

Figure 3.14 displays the stress and strain characteristics of configuration 1. Figure 3.14(a) shows the time histories of the incident and reflected strains. The corresponding transmitted strain and stress of the polyurea layer is shown in Figure 3.14(b).

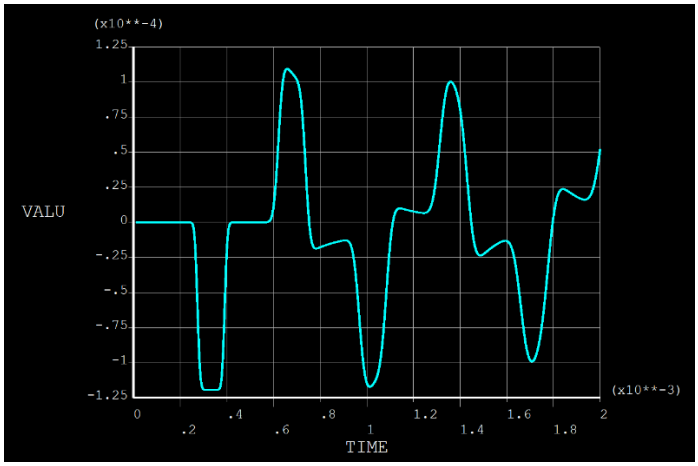

(a)

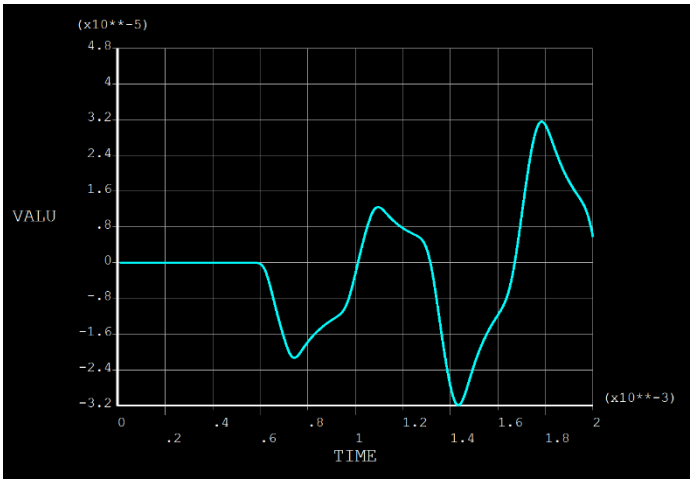

(b)

Figure 3.14 - The Incident and Transmitted Strain signals for Configuration 1 (single polyurea layer)

Configuration 2 (Two Polyurea Layers/One Aluminum Layer)

Figure 3.15 displays the stress and strain characteristics of configuration 2. Figure 3.15(a) shows the time histories of the incident and reflected strains. The corresponding transmitted strain and stress of the polyurea/aluminum composite is shown in Figure 3.15(b).

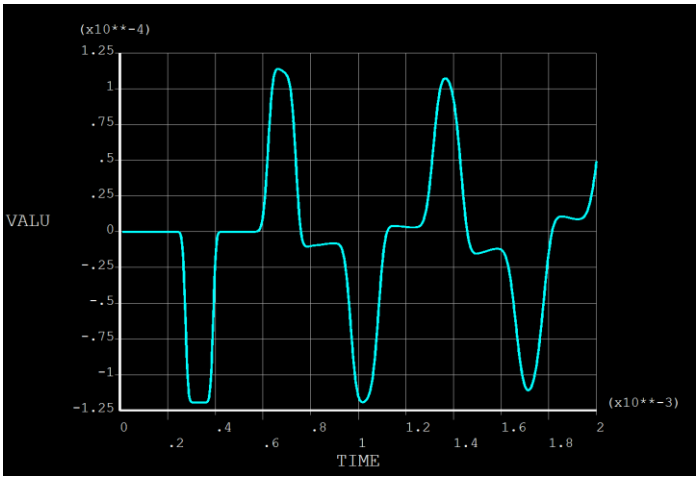

(a)

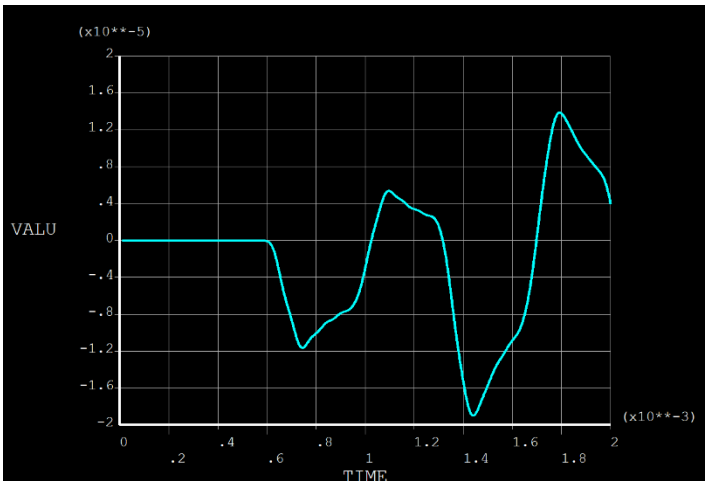

(b)

Figure 3.15 - The Incident and Transmitted Strain signals for Configuration 2 (two polyurea layers and single aluminum layer)

Configuration 3 (Three Polyurea Layers/Two Aluminum Layers)

Figure 3.16 displays the stress and strain characteristics of configuration 3. Figure 3.16(a) shows the time histories of the incident and reflected strains. The corresponding transmitted strain and stress of the polyurea/aluminum composite is shown in Figure 3.16(b).

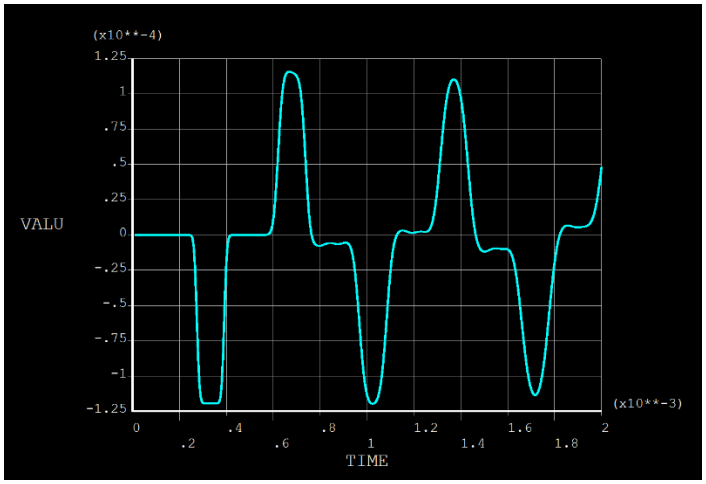

(a)

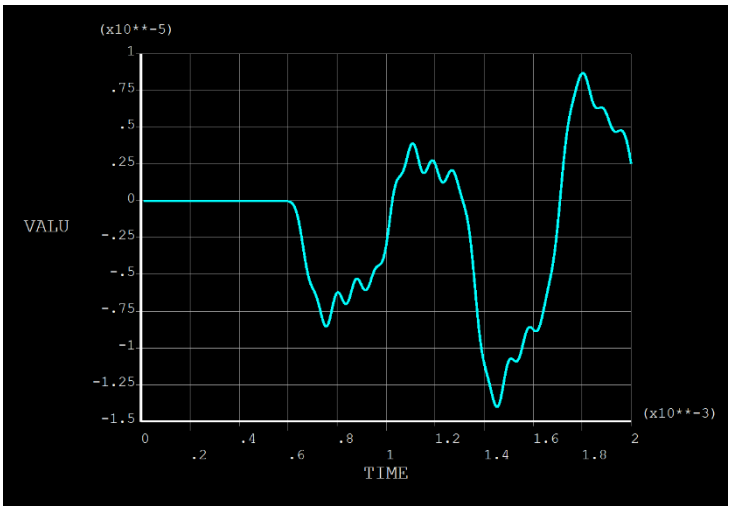

(b)

Figure 3.16 - The Incident and Transmitted Strain signals for Configuration 3 (three polyurea layers and two aluminum layers)

C. Comparison between the predictions of MATLAB FEM and ANSYS

This section presents comparisons between the predictions of the developed *MATLAB FEM* and *ANSYS*.

Configuration 1 (one Polyurea Layer)

Figure 3.17 displays the comparisons between the predictions of the stress and strain characteristics obtained by the *MATLAB FEM* and *ANSYS* for configuration 1. Figure 3.17(a) shows the characteristics predicted by *ANSYS* whereas Figure 3.17(b) displays the corresponding characteristics generated by *MATLAB FEM*. The figures indicate close agreement between the predictions of the *MATLAB FEM* and *ANSYS*.

Configuration 2 (Two Polyurea Layers/One Aluminum Layer)

Figure 3.18 displays the comparisons between the predictions of the stress and strain characteristics obtained by the *MATLAB FEM* and *ANSYS* for configuration 2. Figure 3.18(a) shows the characteristics predicted by *ANSYS* whereas Figure 3.18(b) displays the corresponding characteristics generated by *MATLAB FEM*. The figures indicate close agreement between the predictions of the *MATLAB FEM* and *ANSYS*.

Configuration 3 (Three Polyurea Layers/Two Aluminum Layers)

Figure 3.19 displays the comparisons between the predictions of the stress and strain characteristics obtained by the *MATLAB FEM* and *ANSYS* for configuration 3. Figure 3.19(a) shows the characteristics predicted by *ANSYS* whereas Figure 3.19(b) displays the corresponding characteristics generated by *MATLAB FEM*. The figures indicate close agreement between the predictions of the *MATLAB FEM* and *ANSYS*.

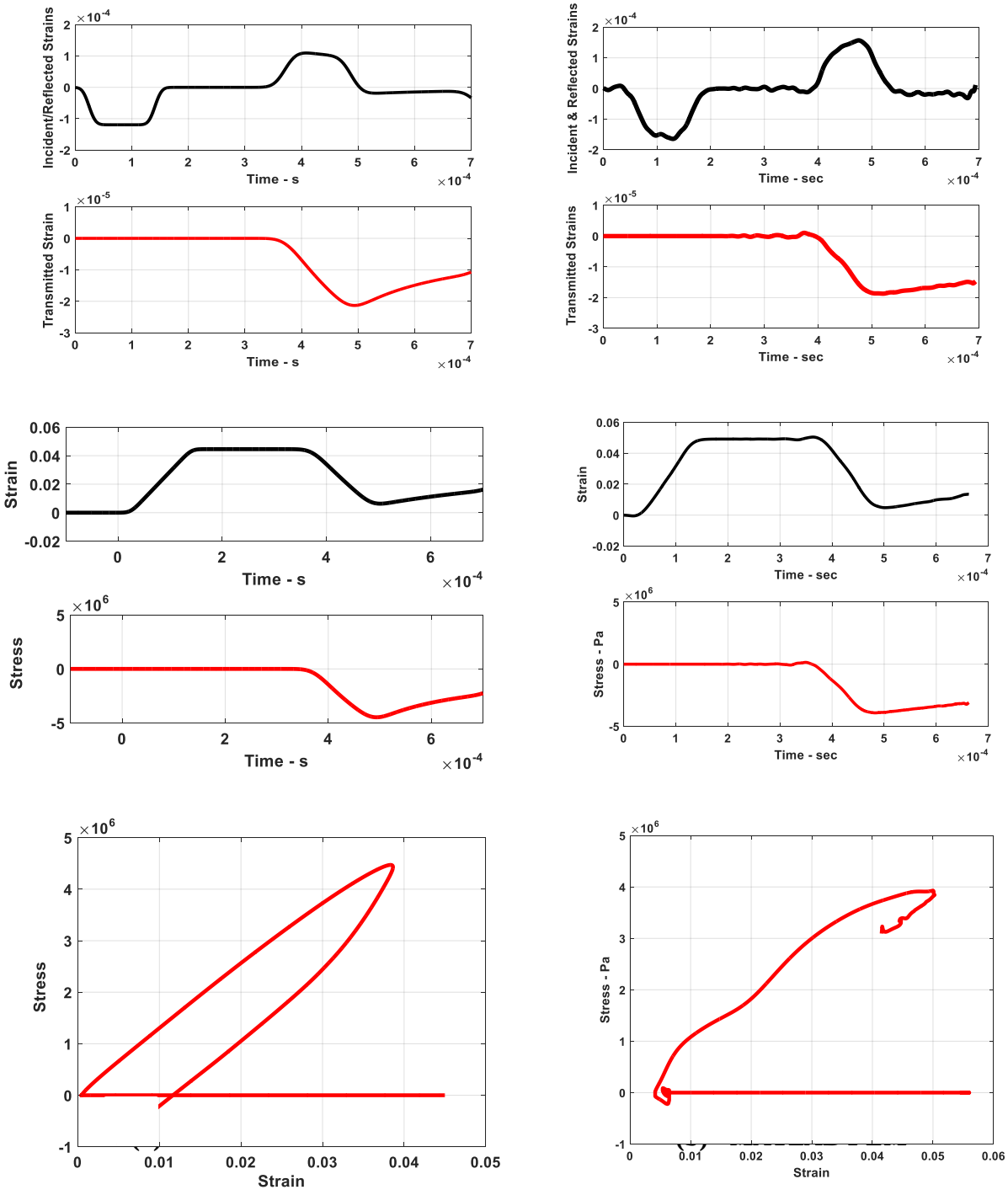

(a) – *ANSYS* (b) – *MATLAB FEM*

Figure 3.17 - Stress-Strain characteristics for Configuration 1 – ANSYS and (b) – MATLAB FEM

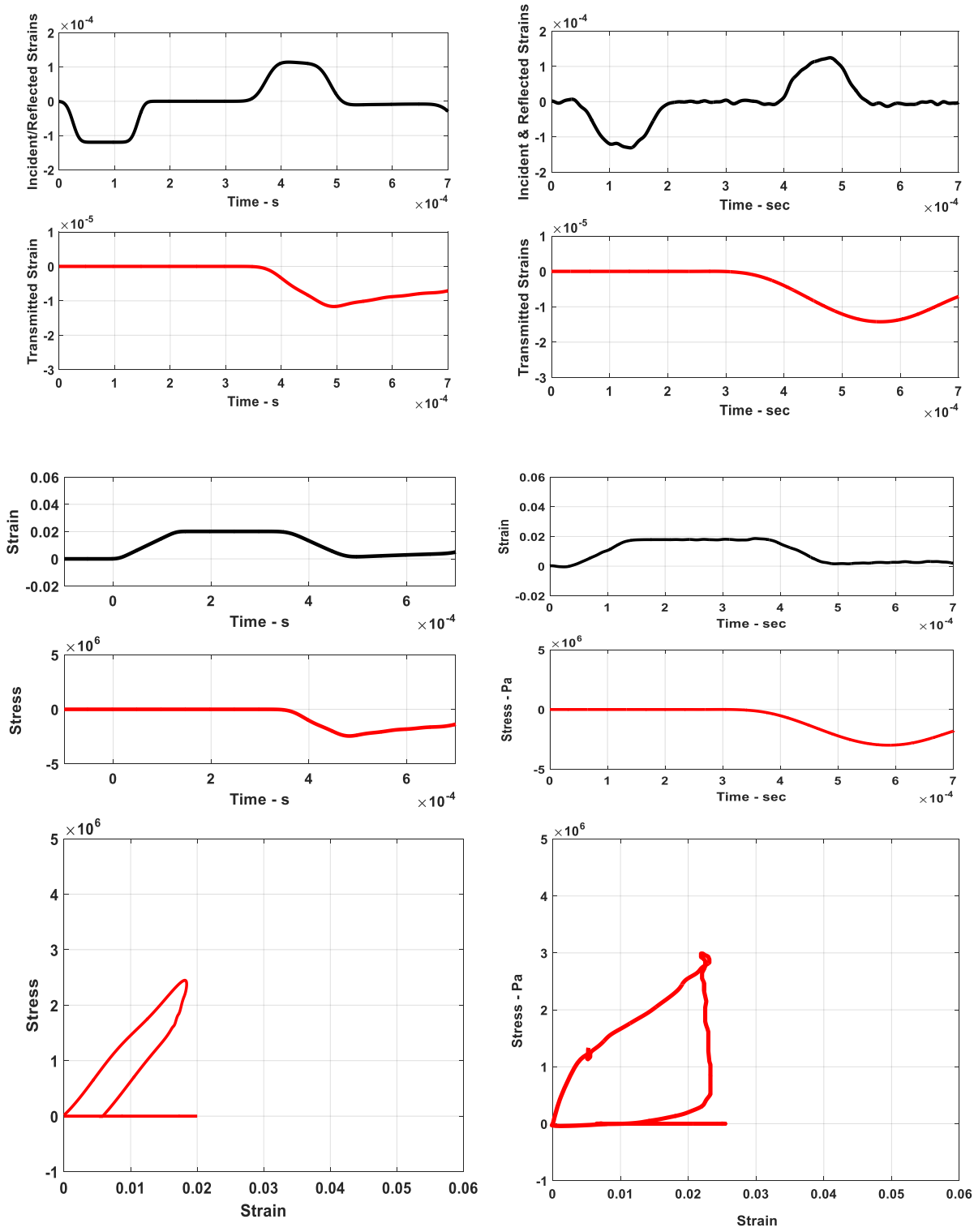

(a) – *ANSYS* (b) – *MATLAB FEM*

Figure 3.18 - Stress-Strain characteristics for Configuration 2 – ANSYS and (b) – MATLAB FEM

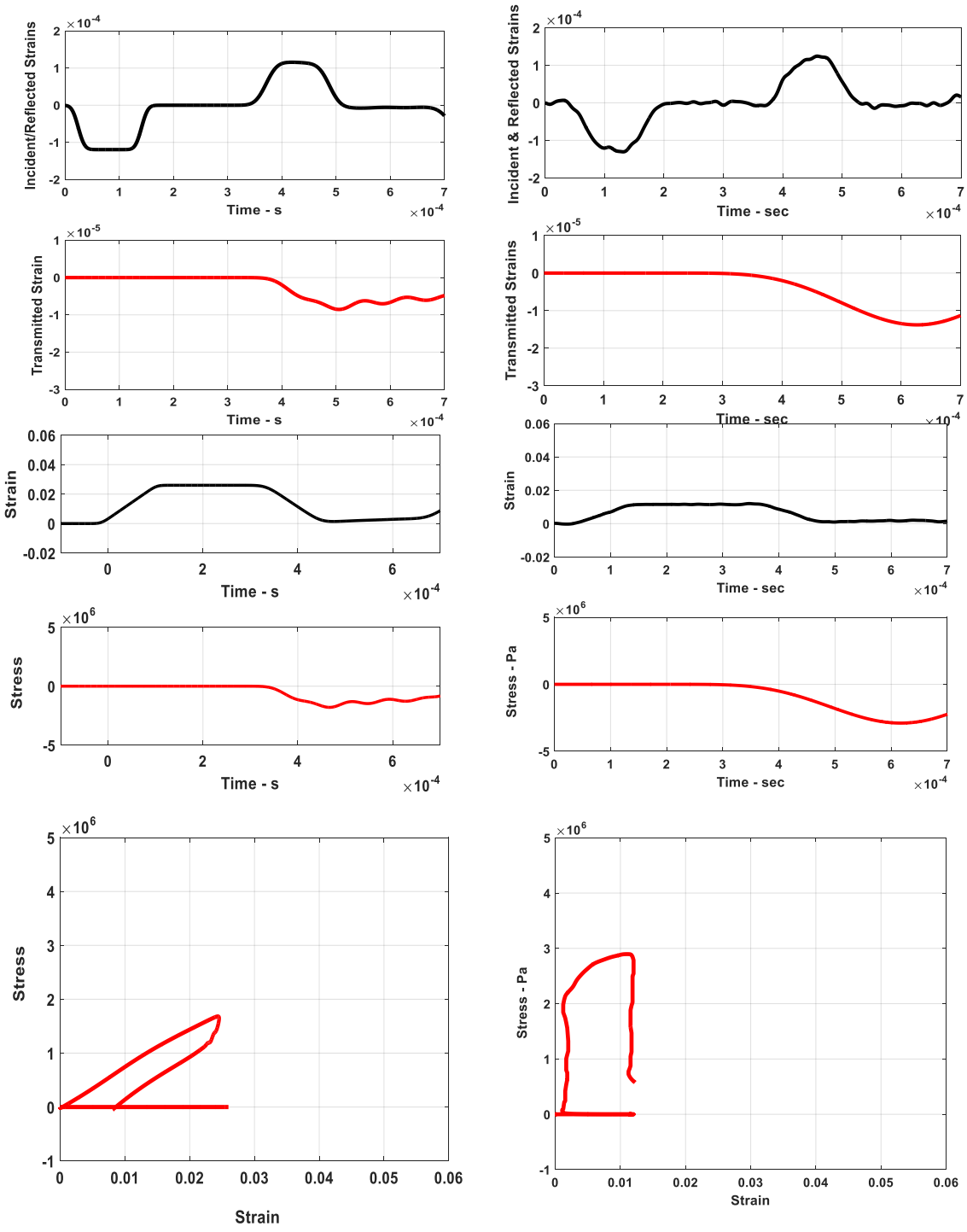

(a) – *ANSYS* (b) – *MATLAB FEM*

Figure 3.19 - Stress-Strain characteristics for Configuration 3 – ANSYS and (b) – MATLAB FEM

3.4. SUMMARY

This chapter presented modeling of the dynamics of polyurea composites when subject to high strain loading. The details of a finite element model (*FEM*) are outlined and developed in section 3.2. The predictions of the *FEM* are determined for three configurations of the polyurea composites and presented in section 3.3. The predictions of the *MATLAB FEM* are validated against the predictions of the commercial finite element package *ANSYS*.

The comparisons between the predictions of the *MATLAB FEM* and *ANSYS* are presented in section 3.3. The established comparisons indicate close agreements between these predictions.

These predictions are further validated experimentally as will be presented in Chapter 4.

Chapter 4

EXPERIMENTAL CHARACTERIZATION OF POLYUREA COMPOSITES

4.1 Experimental Setup of Split Hopkinson Pressure Bar (*SHPB*)

4.1.1 Construction of the *SHPB*

In order to understand the construction and operation of the *SHPB*, it is useful to divide the setup into three systems namely:

- The Pneumatic system
- The Mechanical system
- The Measuring system

The pneumatic system can be understood using the circuit shown in Figure (4.1).

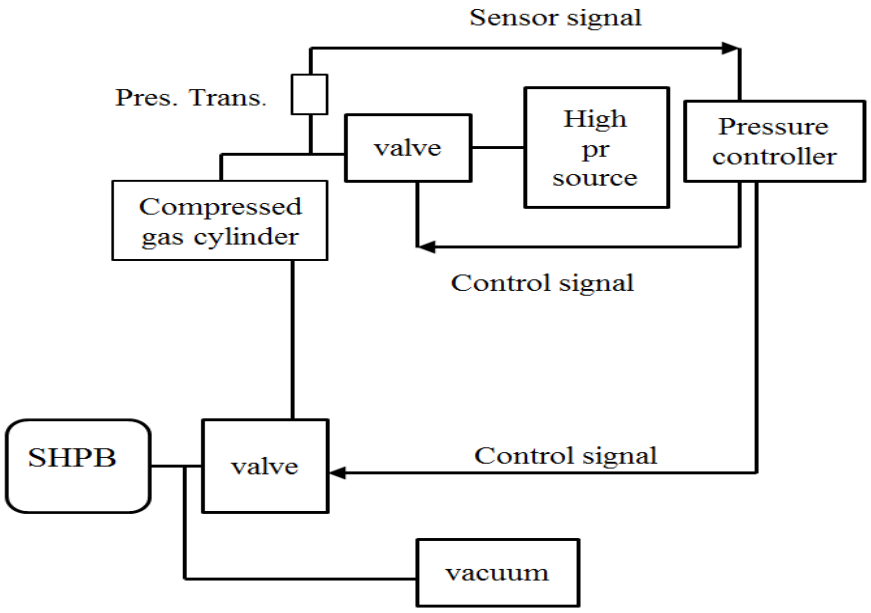

Figure 4.1: Schematic of the construction of the *SHPB*

The striking bar is pressurized shown in above circuit in order to force the bar to move with high speed.

Details of the circuit:

- Compressed air is stored in a High-pressure tank acting as a reservoir to maintain a controllable constant pressure.
- To control the pressure inside the tank there is a pressure controller.
- To measure the pressure inside the tank there is a pressure transducer that feeds the output signal to the pressure controller.
- A High-pressure source to fill in the air tank as needed when the pressure inside drops below the required value.
- A pressure controller controls a pneumatic valve to open/close the gate for the pressure source to feed in the air tank.
- The output of the air tank is connected by a pressure valve to the inlet of the *SHPB* striking bar to apply the required pressure forcing the striking bar to move with the required speed.
- A vacuum source to pull the striking bar to its original position after the specimen is hit to make it ready for the next measurement.

The Mechanical System of the *SHPB*

The mechanical system consists of the striking bar, the incident bar, the transmission bar and the back stop. The sample is mounted between both the incident and striking bar and is maintained in contact with both bar ends (trapped between both ends). The other end of the transmission bar is backed with a heavily damped weight to prevent the transmission bar from flying away with high speed. The striking bar is moving inside a hollow cylinder that acts as a

guide for proper application of load. Both the incident and transmission bars are guided through sliding bearings.

The Measuring system

The measuring system consists of two strain gauges, one attached to incident bar and the other to the transmission bar. The wiring of both strain gauges is then fed to a Wheatstone Half - Bridge for strain measurements. The circuit of the strain gauges is as illustrated in Figure 4.2.

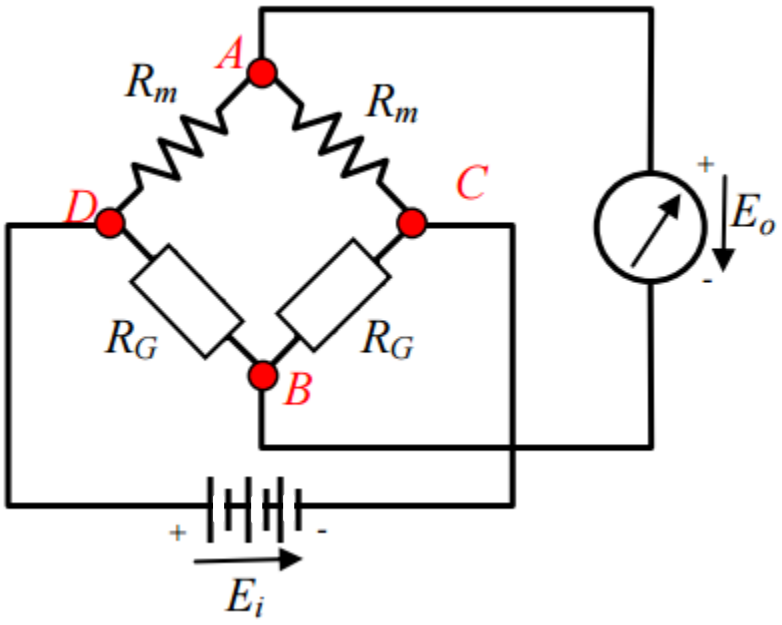

Figure 4.2: Schematic of a half-wheatstone bridge Circuit

A strain gauge produces a resistance change proportional to strain. The proportionality factor GF is called the gauge factor and depends on the strain gauge material.

$$\frac{\Delta R}{R} = G_F \frac{\Delta L}{L} = G_F \epsilon \tag{4.1}$$

We can therefore write for the resistance change in the Incident and transmitted bar strain gauges as:

$$R_2 = R_{G0} + \Delta R = R_G\,(1 + G_F\epsilon) \tag{4.2}$$

$$R_4 = R_{G0} - \Delta R = R_G\,(1 - G_F\epsilon) \tag{4.3}$$

where $R_{G0} =$ nominal (unstrained) gauge resistance and assume that R_m is the nominal value of $R_1\ and\ R_3$.

Substitution of these results into the equation for the bridge output voltage yields

$$\frac{E_0}{E_i} = \frac{R_m}{R_m + R_m} - \frac{R_{G0}\,(1 - G_F\epsilon)}{R_{G0}\,(1 + G_F\epsilon) + R_{G0}\,(1 - G_F\epsilon)} \tag{4.4}$$

or

$$\frac{E_0}{E_i} = \frac{1}{2} - \frac{1 - G_F\epsilon}{2} = \frac{G_F\epsilon}{2} \tag{4.5}$$

Equation (4.5) is linear in the strain and only depends on the gauge factor independent of the resistor values of the strain gauges or the opposing resistors.

It is very important to note that the concept of the Whetstone Bridge lies in the electrical balance of the bridge, which two arms are connected to two strain gauges forming the half bridge. Therefore, at the beginning of the experiment the output voltage of the bridge has to be zero, to ensure proper balance is there for proper measurement. This balance can be forced using one of two methods; the first is by using an externally attached potentiometer that balances the circuit. The other method is using the on-board zero-adjusting resistance. The correct balance is detected using the oscilloscope by feeding the time-signal to the oscilloscope and changing the resistances until they reach zero on the oscilloscope screen.

The oscilloscope used, is a 4-channel 1*GHz* oscilloscope with 4 inputs. Two inputs are used to measure the time signals of the strain gauges. The oscilloscope has two modes of operation (continuous run mode) and (trigger mode). In the first mode (continuous run), the oscilloscope continuously measures the signals input to its ports and plots a real-time plot of them. In the second (trigger) mode, the oscilloscope is not capturing any data unless a certain voltage level is reached at one of its selected inputs. Therefore, we set the trigger source to be the signal measured by the incident strain gauge. Once the striking bar hits the incident bar and the pressure wave moves to the sample, it causes the incident strain gauge to deflect and sends a signal to the oscilloscope. At this specific moment, when the strain gauge signal reaches a certain level, the oscilloscope starts capturing the data from all its ports and records them. Once completed, the data plots can be saved on a floppy disk to be analyzed later on a computer.

Auxiliary Measuring systems

Two additional measuring systems are to be attached to the *SHPB*; the first is a load cell and the second is a temperature controlled chamber. The load cell is from OMEGA and is as illustrated in Figure 4.5.

The load cell is to be mounted at the tip of the incident bar close to the sample. This way, not only the strain is measured but also the impact force.

4.1.2 Operation of the *SHPB*

The pressure inside the tank is controlled using the pressure controller, which has two set points (*SP1* and *SP2*), which decides the lower and upper pressure values of the pressure inside the tank. A calibration chart is used to get the required speed of the striking bar by setting *SP1* and *SP2* to a specified value. Once set, the pressure source starts feeding in air to the tank via the inlet

pneumatic valve until the pressure inside reaches the required set value (which is detected by the pressure transducer) and thus the controller closes the inlet valve maintaining a stable and constant pressure inside the tank.

A remote control is used to send a signal to feed to the controller that opens the second valve (outlet valve) causing the high pressure to flow to the striking bar and the impact takes place. Again, using the same remote control, the controller is sent a signal to close the second valve and the vacuum acts at this moment to withdraw the striking bar back to its position.

The schematic of a typical *SHPB* is as illustrated in Figure 4.3, where a high-pressure air is forcing a striker bar to accelerate and strikes the incidence bar. The strike introduces a pressure wave that propagates through the incidence bar to the transmission bar passing through the specimen to be tested.

Thus, an impact loading is applied to the specimen. In other words, high strain rate is introduced in the specimen. In order to measure the material properties, the time-dependent incident, reflected and transmitted waves must be measured simultaneously. This is achieved using two strain gauges; the first is attached to the incidence bar and the second is attached to the transmission bar. Both the signals from these two strain gauges are fed to a high sampling rate oscilloscope that captures the time domain signal of both the strain gauges.

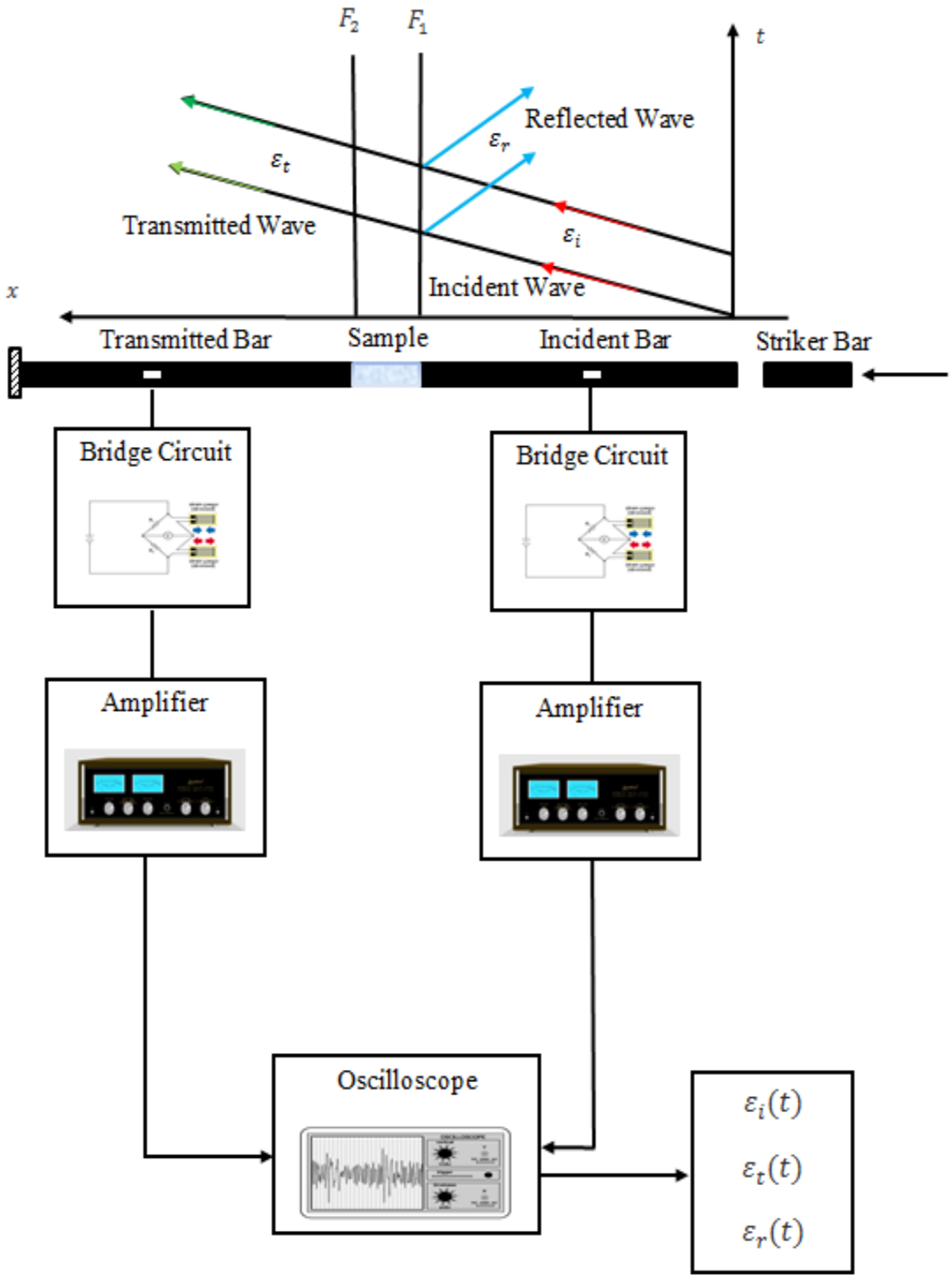

Figure 4.3: Schematic of operation of the *SHPB*

A striker bar of various lengths will produce different loading durations, *i.e.*, short striker bars impart short time duration loads as shown in Figure 4.4. The impact of the striker bar triggers data collection from the strain gages located on the incident and transmission bars. From the data collected by the strain gauges, stress, strain, and strain rate can be calculated.

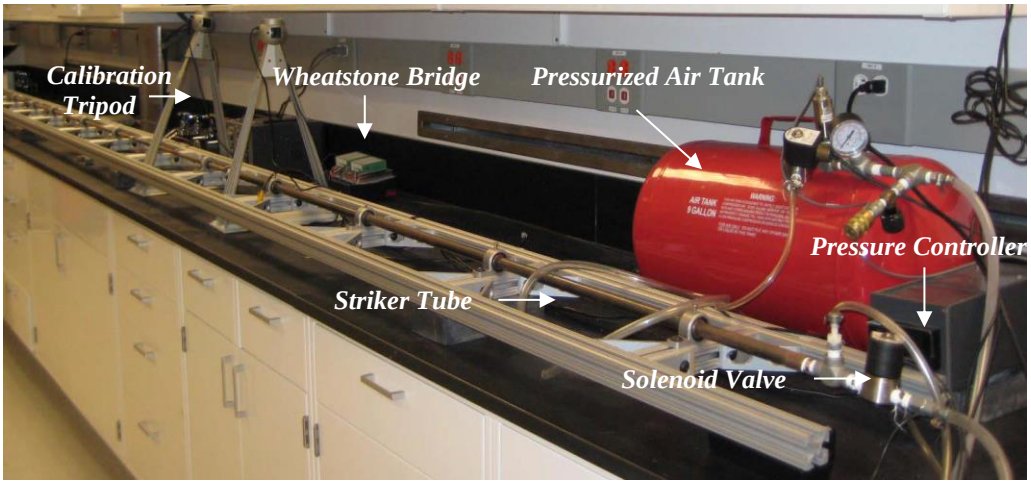

Figure 4.4: *SHPB* with gas cylinder

The striking speed is measured and calibrated for different levels of air pressure using a calibration tripod shown in Figures 4.5 and 4.6.

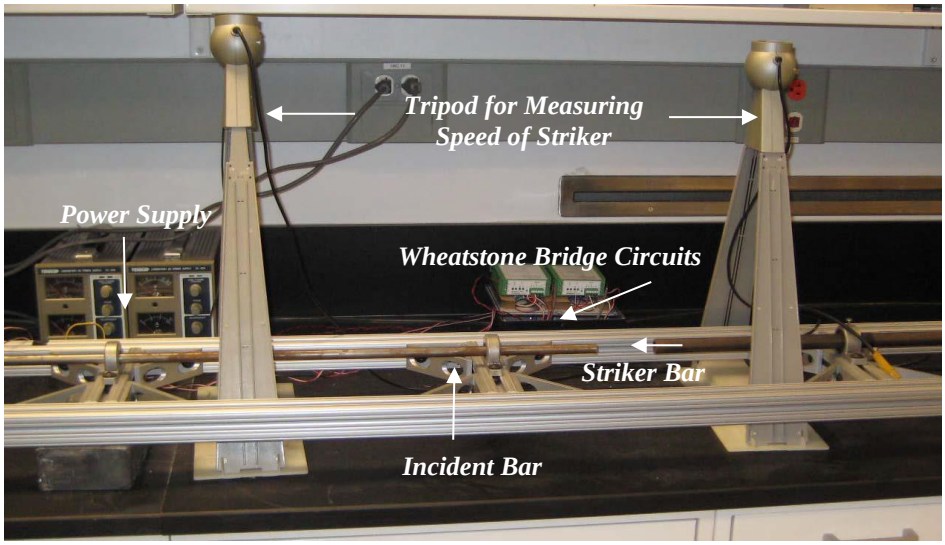

Figure 4.5: *SHPB* with wheatstone bridge circuit

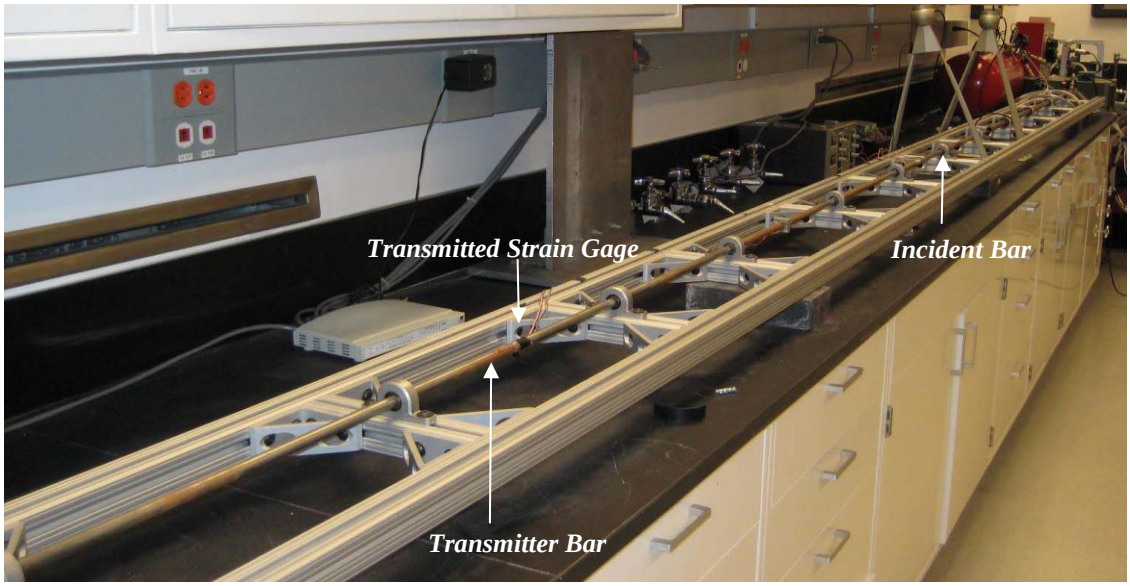

Figure 4.6: Incident and Transmitted bars of the *SHPB*

4.2 Calibration of the SHPB

Figure 4.7 displays the calibration curve of the striker speed as function of the applied air pressure.

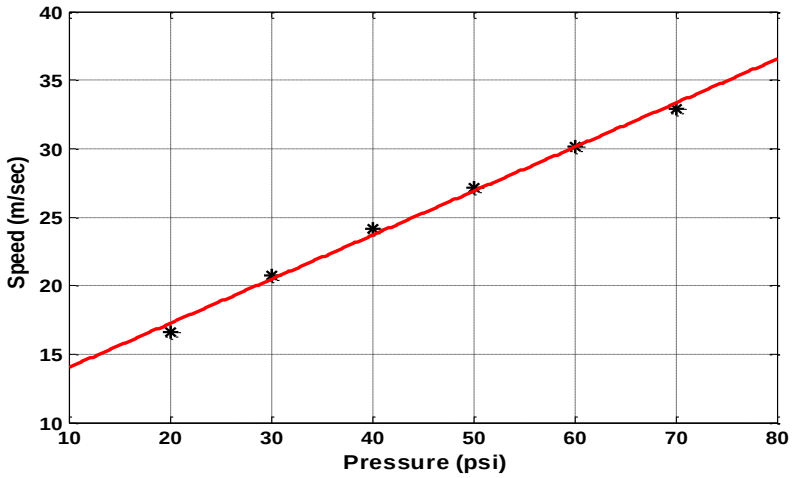

Figure 4.7: Calibration of the striker speed

Also, Figure 4.8 displays the calibration characteristics of the incident and transmitted strain gages as functions of the striking force.

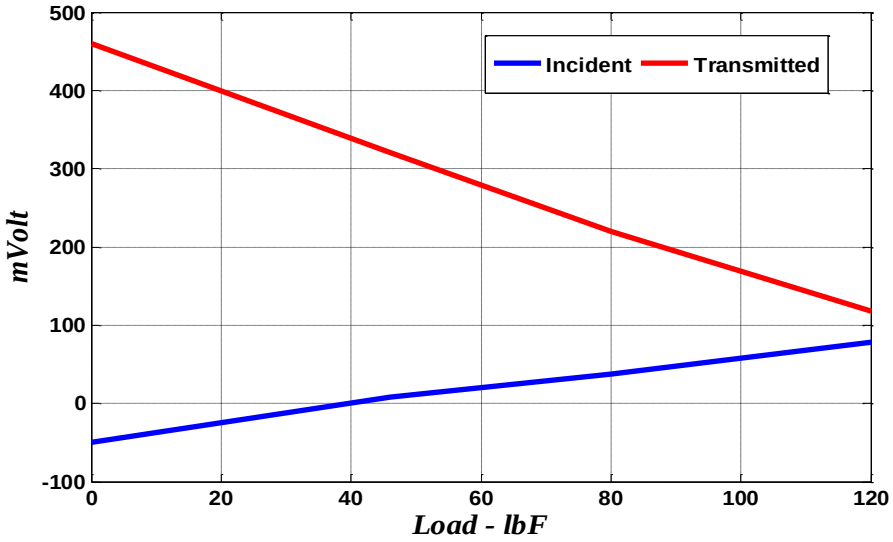

Figure 4.8: Calibration of the Incident and Transmitted Strain Gages

4.3. Experimental Results

This section summarized the main experimental results which are obtained for the three configurations of the polyurea composites shown in Figure 4.9.

Figure 4.9 indicates that the considered configurations include the configurations listed in Table 4.1. In these configurations, the polyurea layers are 0.0033 m in thickness and the aluminum layers are 0.000711 m in thickness.

Figure 4.9: Experimental Configurations of the polyurea composites

Table 4. 1– Configurations of the tested polyurea composites

Configurations	Number of Polyurea Layers	Number of Aluminum Layers
1	1	0
2	2	1
3	3	2

Figure 4.10 displays the incident and transmitted strain signals as measured for configuration 1 which is a single layer of polyurea.

Figures 4.11 and 4.12 show the corresponding characteristics of configurations 1 and 3, respectively. In configuration 2, two layers of polyurea sandwich a single layer of aluminum while in configuration 3, three layers of polyurea are used to sandwich two layers of aluminum as shown in Figure 4.9.

Configuration 1

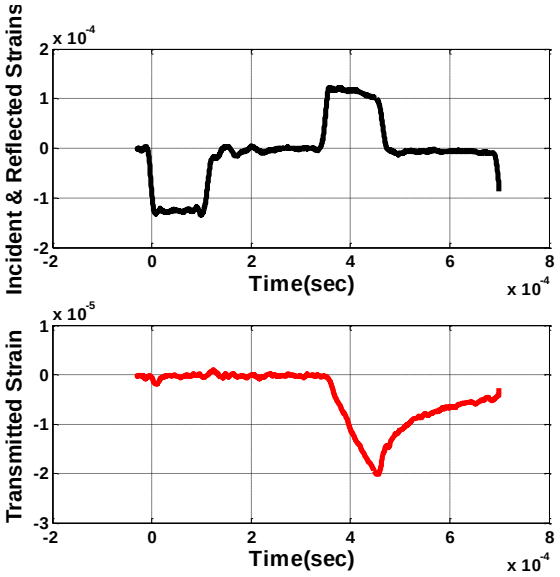

Figure 4.10 - Incident and Transmitted Strain signals for Configuration 1 (single polyurea layer)

Configuration 2

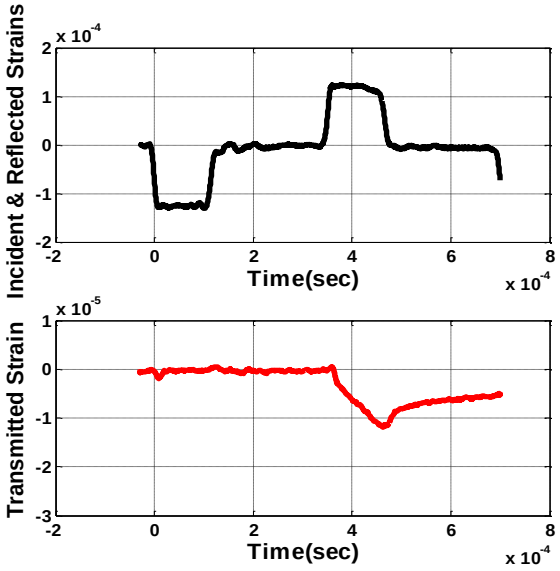

Figure 4.11 - Incident and Transmitted Strain signals for Configuration 2 (two polyurea layers and single aluminum layer)

Configuration 3

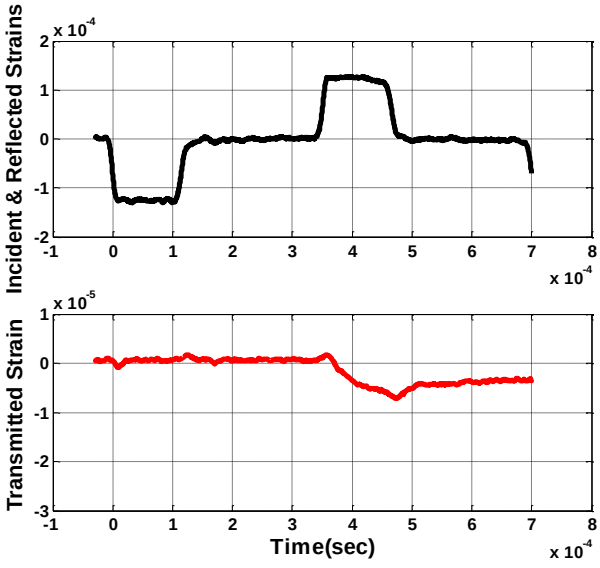

Figure 4.12 - Incident and Transmitted Strain signals for Configuration 3 (three polyurea layers and two aluminum layers)

The time histories of the incident and transmitted strains (ε_i, ε_t) are used to generate the strain and stress in the different polyurea composite configurations using the flow chart outlined in Figure 4.13.

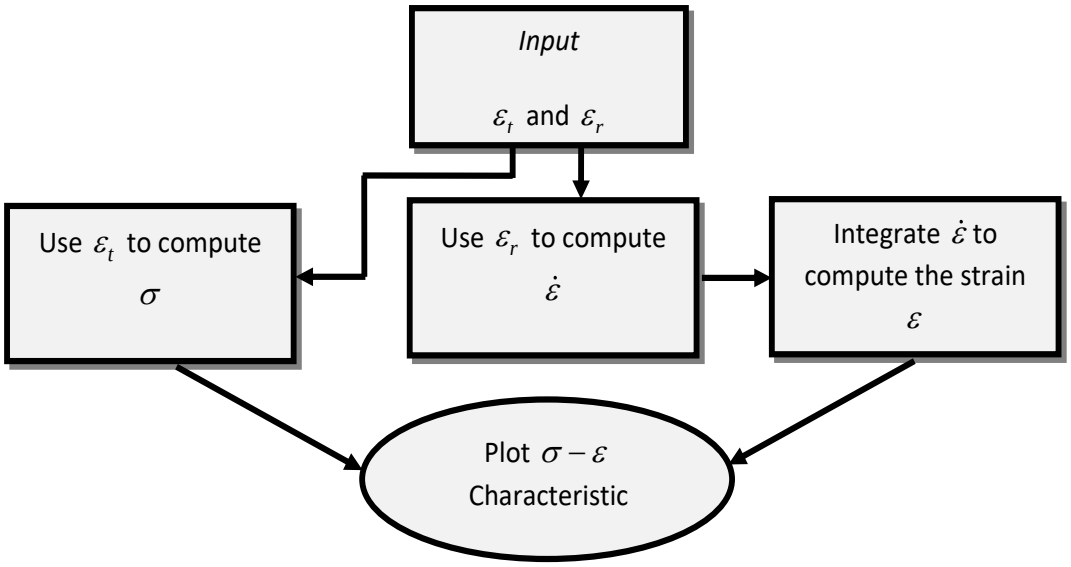

Figure 4.13 - The flow chart for calculating the strain and stress in the polyurea composites

Figures 4.14 through 4.16 display the calculated time histories of the strain and stress of configurations 1 through 3 respectively.

Configuration 1

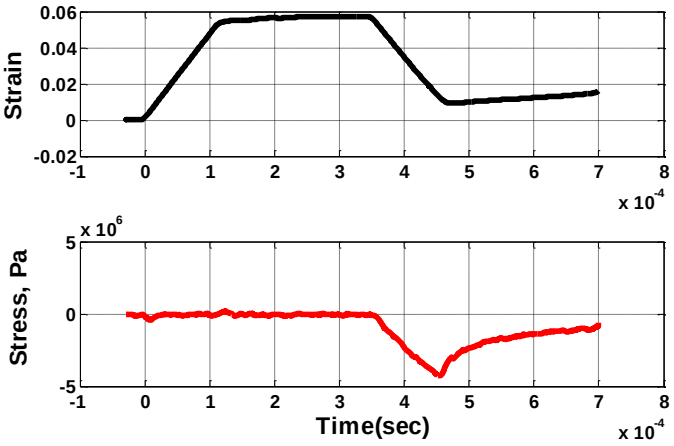

Figure 4.14 - Calculated time histories of the Strain and Stress for Configuration 1 (single polyurea layer)

Configuration 2

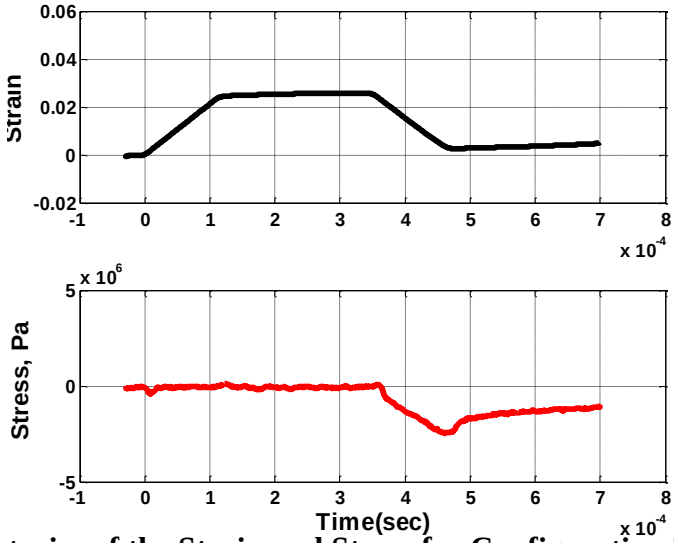

Figure 4.15 - Calculated time histories of the Strain and Stress for Configuration 2 (two polyurea layers and single aluminum layer)

Configuration 3

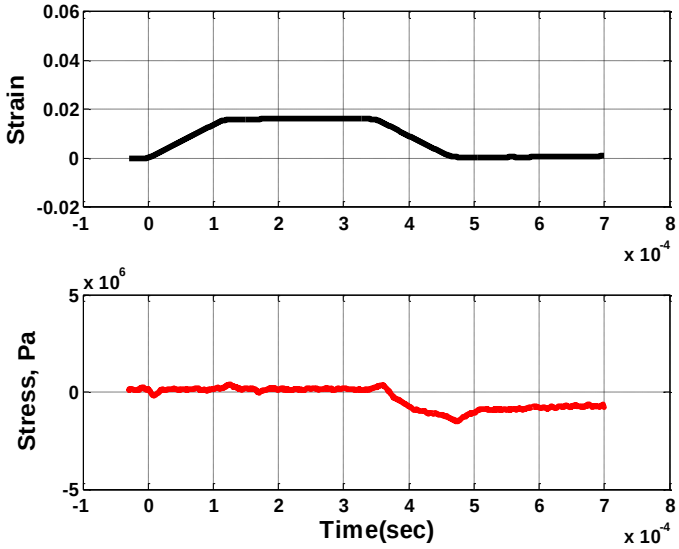

Figure 4.16 - Calculated time histories of the Strain and Stress for Configuration 3 (three polyurea layers and two aluminum layers)

Figures 4.17 through 4.19 display the stress-strain characteristics of configurations 1 through 3 respectively as obtained by eliminating the time from the time histories of Figures 4.14 through 4.16.

Configuration 1

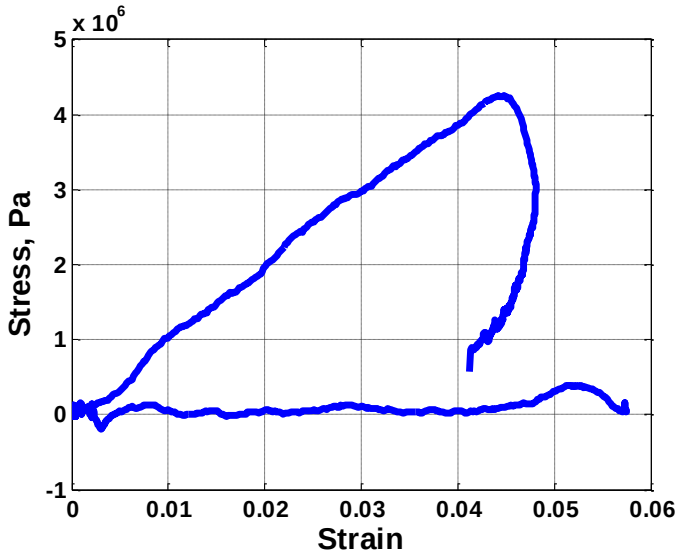

Figure 4.17 - Stress-Strain characteristics for Configuration 1

(single polyurea layer)

Configuration 2

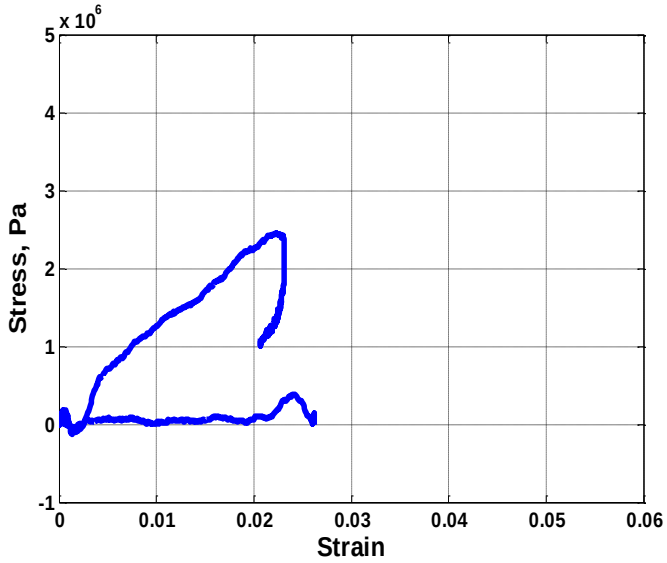

Figure 4.18 - Stress-Strain characteristics for Configuration 2

(two polyurea layers and single aluminum layer)

Configuration 3

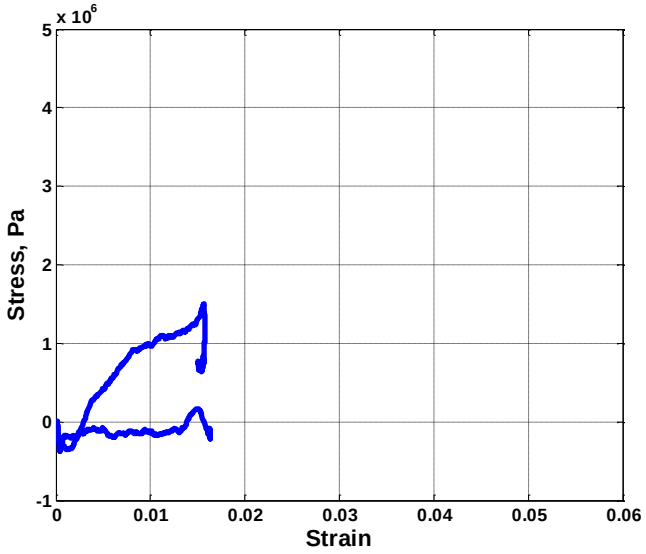

Figure 4.19 - Stress-Strain characteristics for Configuration 3

(three polyurea layers and two aluminum layers)

A better understanding of the effect of the configuration of the polyurea composite on the stress-strain characteristics can best be understood by considering the combined plots displayed in Figure 4.20.

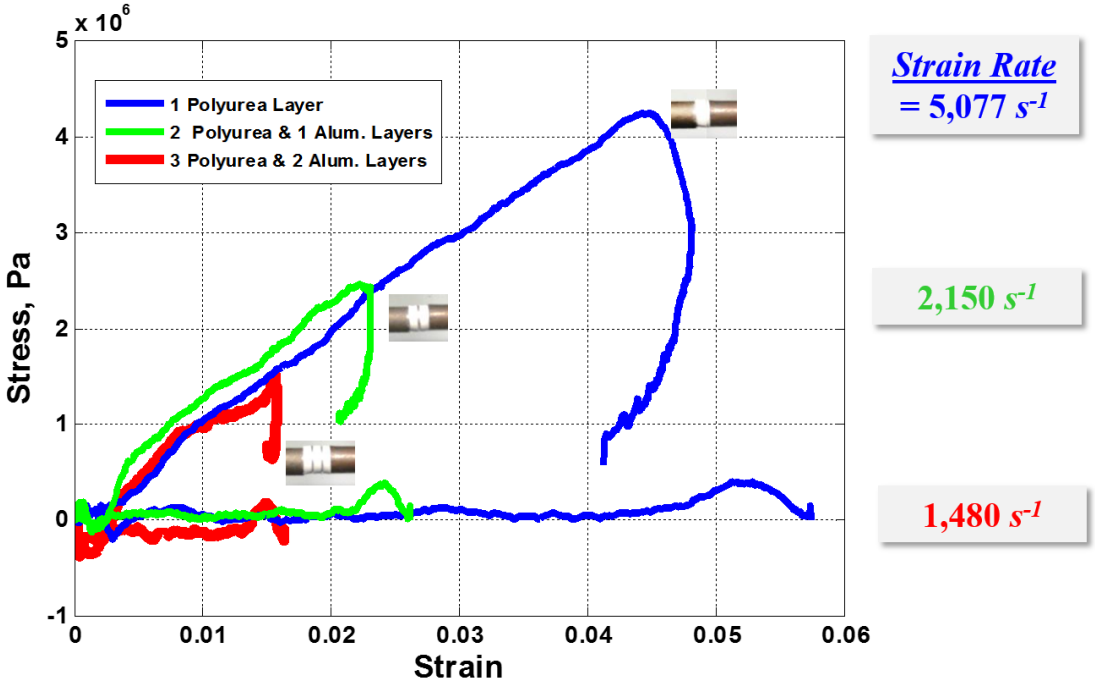

Figure 4.20 - Stress-Strain characteristics for the different Configurations of the polyurea composites

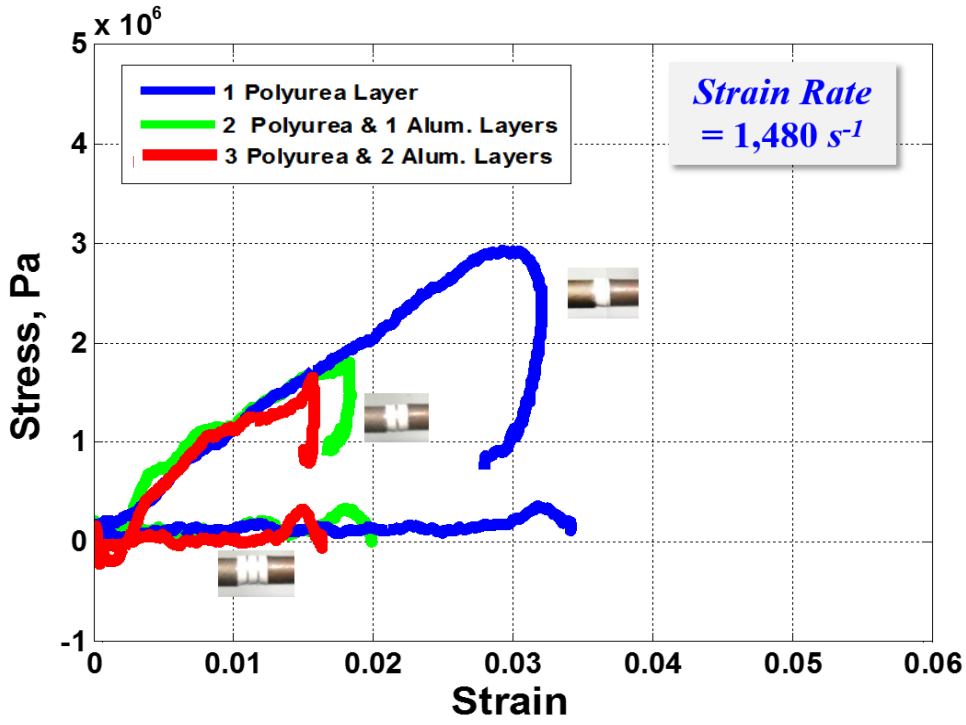

Figure 4.21 - Stress-Strain characteristics for the different Configurations of the polyurea composite at strain rate of 1,480 s^{-1}

4.5. Comparison between the Experimental Results and the Predictions of *ANSYS*

This section presents comparisons and validation of the predictions of the developed *ANSYS* model and the experimental results.

Configuration 1 (one Polyurea Layer)

Figure 4.22 displays the comparisons between the experimental results and the predictions of the stress and strain characteristics obtained by *ANSYS* for configuration 1. Figure 4.22(a) shows the characteristics predicted by *ANSYS* whereas Figure 4.22b displays the corresponding characteristics generated experimentally. The figures indicate close agreement between the experiments and the predictions of *ANSYS*.

Configuration 2 (Two Polyurea Layers/One Aluminum Layer)

Figure 4.23 displays the comparisons between the experimental results and the predictions of the stress and strain characteristics obtained by *ANSYS* for configuration 2. Figure 4.23(a) shows the characteristics predicted by *ANSYS* whereas Figure 4.23(b) displays the corresponding characteristics generated experimentally. The figures indicate close agreement between the experiments and the predictions of *ANSYS*.

Configuration 3 (Three Polyurea Layers/Two Aluminum Layers)

Figure 4.24 displays the comparisons between the experimental results and the predictions of the stress and strain characteristics obtained by *ANSYS* for configuration 3. Figure 4.24(a) shows the characteristics predicted by *ANSYS* whereas Figure 4.24(b) displays the corresponding characteristics generated experimentally. The figures indicate close agreement between the experiments and the predictions of *ANSYS*.

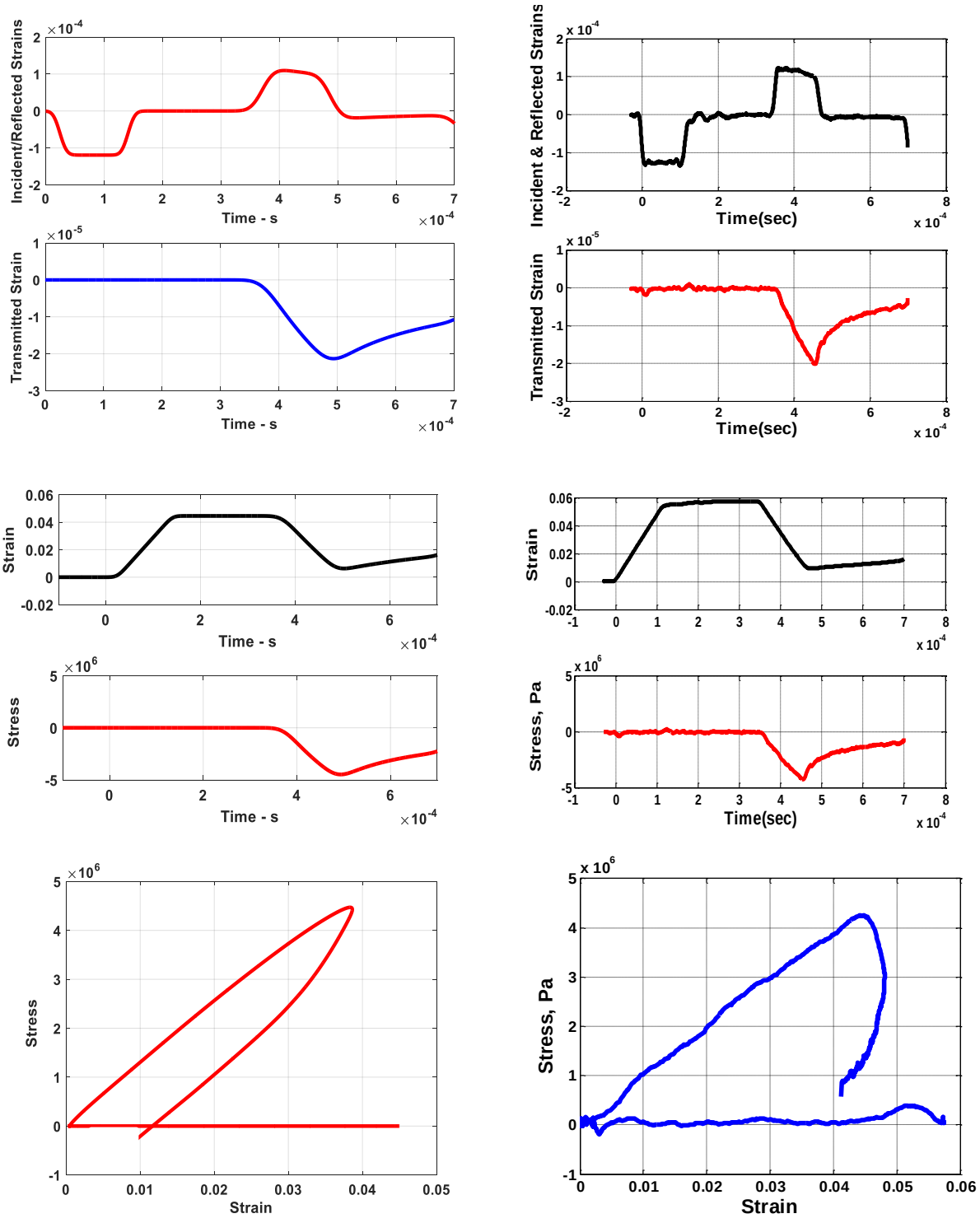

(a) – *ANSYS* (b) – *MATLAB FEM*

Figure 4.22 - Stress-Strain characteristics for Configuration 1

(a) – *ANSYS* and (b) – *Experiments*

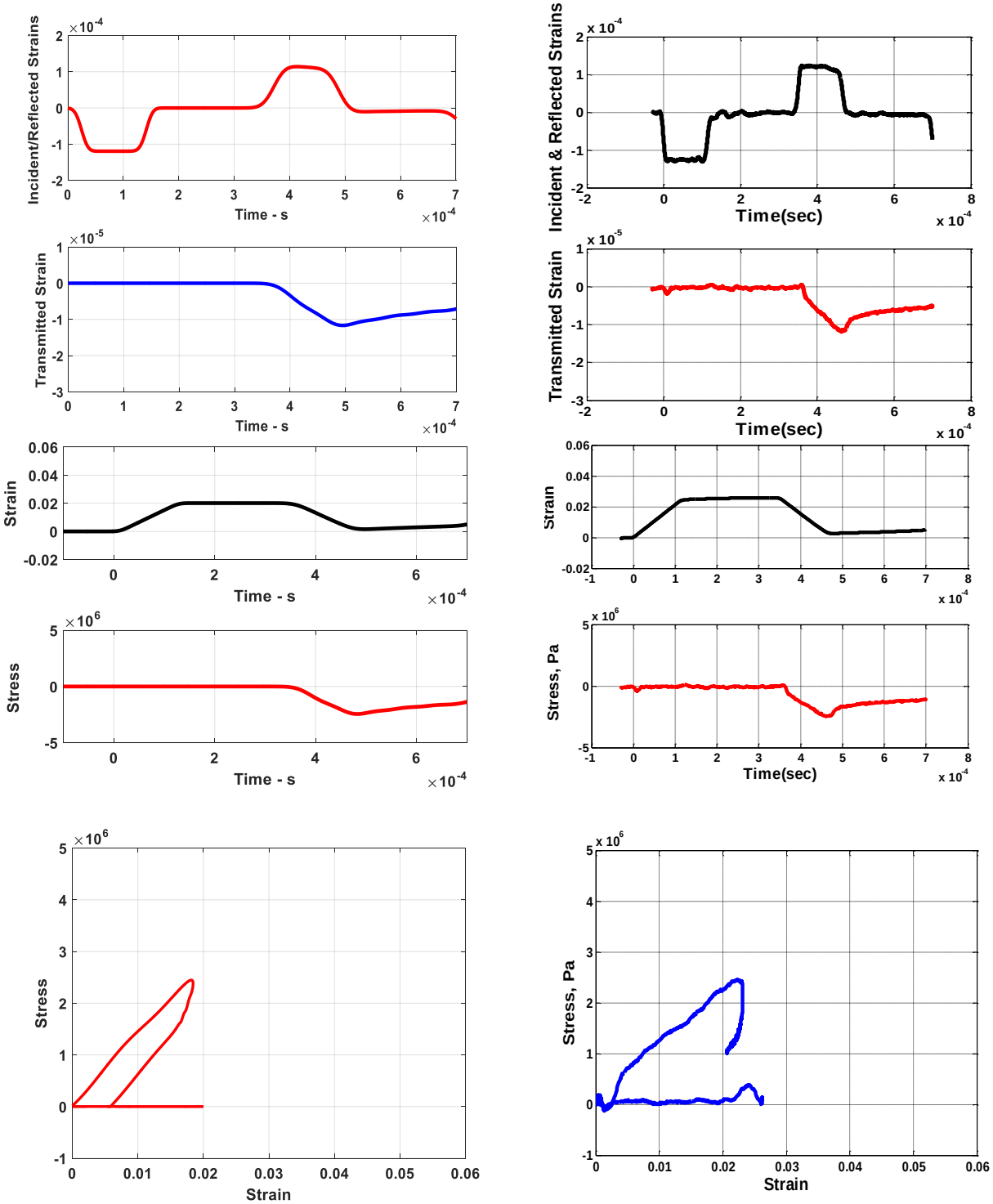

(a) – *ANSYS* (b) – *MATLAB FEM*

Figure 4.23 - Stress-Strain characteristics for Configuration 2

(a) – *ANSYS* and (b) – *Experiments*

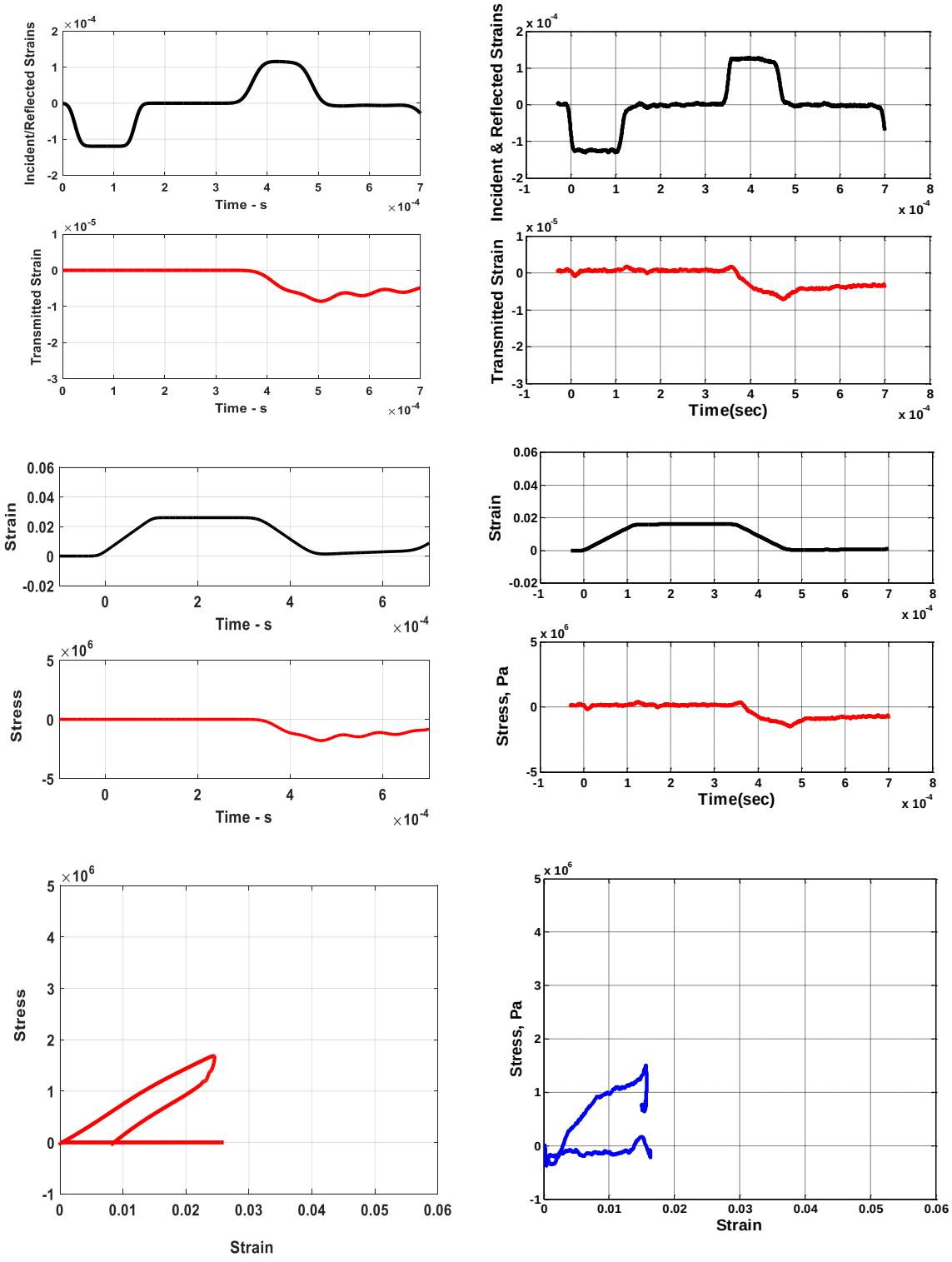

(a) – *ANSYS* (b) – *MATLAB FEM*

Figure 4.24 - Stress-Strain characteristics for Configuration 3 – ANSYS and (b) – Experiments

4.4. SUMMARY

This chapter presented the experimental dynamic characteristics of polyurea composites when subject to high strain loading using the Split Hopkinson Pressure Bar (SHPB) method. The details of experimental setup and calibration are outlined and developed in section 4.1 and 4.2. The experimental results are determined for three configurations of the polyurea composites and presented in section 4.3. These results are used to validate the predictions of the commercial finite element package *ANSYS*.

The comparisons between the predictions of *ANSYS* and the experimental are presented in section 4.4. The established comparisons indicate close agreements between the experiments and theoretical predictions.

Chapter 5

CHARACTERISTICS OF PERIODIC POLYUREA COMPOSITES

INTRODUCTION

The polyurea composites when arranged in periodic arrangements can possess unique wave propagation characteristics primarily because of their inherent design features. These features include the inclusion of the polyurea as a damping ingredient as well as sources of locally resonant substructures by virtue of the aluminum layers. Because of such features, the periodic polyurea composites will have the ability to completely block the propagation of waves over broad frequency bands called "*band gaps*". Such unique wave filtering capabilities render the periodic polyurea composites to be effective means for mitigating the effect of high strain loading such as blast wave loading.

In this chapter, the theory that govern the wave propagation characteristics in periodic polyurea composites (*PPM*) is presented. The effect of the configuration of the *PPM*, as is shown typically in Figure 5.1, on the wave propagation characteristics is investigated using the Bloch wave propagation approach.

Numerical examples are considered to demonstrate the filtering capabilities of the *PPM* for various blast wave loading conditions.

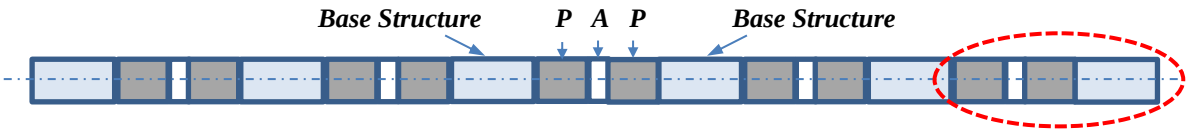

Figure 5.1: Typical periodic polyurea composite

(*P* = Polyurea, *A* = Aluminum)

5.1. Modeling of the Band Gap Characteristics of Polyurea Composites

The theory of periodic structures was originally developed for solid state applications (Brillouin, 1946) and extended, in the early seventies, to the design of mechanical structures (Mead, 1970 and Cremer *et al*., 1973). Since then, the theory has been extensively applied to a wide variety of structures such as spring-mass systems (Faulkner and Hong, 1985), periodic beams (Mead, 1971 and 1975), stiffened plates (Sen Gupta, 1970), ribbed shells (Mead and Bardell, 1987) and space structures. Apart from their unique filtering characteristics, the ability of periodic structures to transmit waves, from one location to another, within the pass bands can be greatly reduced with the ideal periodicity.

In this chapter, the theory of periodic structures will be applied to structures with periodic inserts that have built-in local sources of resonance in an attempt to shift the zones of stop bands to lower frequencies. In this regard, the wealth of the new literature will be capitalized on. Examples of such recent publications include the work of Nouh *et al.* [31].

A. Analysis of Periodic Polyurea Composites using Transfer Matrix Method

In order to develop the proposed approach, the viscoelastic damping is described in the time domain by the Golla-Hughes-McTavish model described in section 3.1.

In this case, the finite element model of a unit cell of the polyurea composites can be written as given by equation (3.35) in Section 3.2, such that:

$$[M\ ]\{\ddot{u}\} + [C\ ]\{\dot{u}\} + [K\ ]\{u\} = \{F_T\} \tag{5.1}$$

where M, C, and K denote the mass, damping, and stiffness matrices respectively. Also, F_T and u define the forcing function acting on the composite and the resulting nodal deflection vector, respectively.

The nodal deflection vector of a unit cell u is defined as:

$$u = \{u_L \quad u_i \quad u_R\}^T \tag{5.2}$$

where u_L, u_i, and u_R denote the boundary, internal, and lower deflection vectors as shown in Figure (5.2).

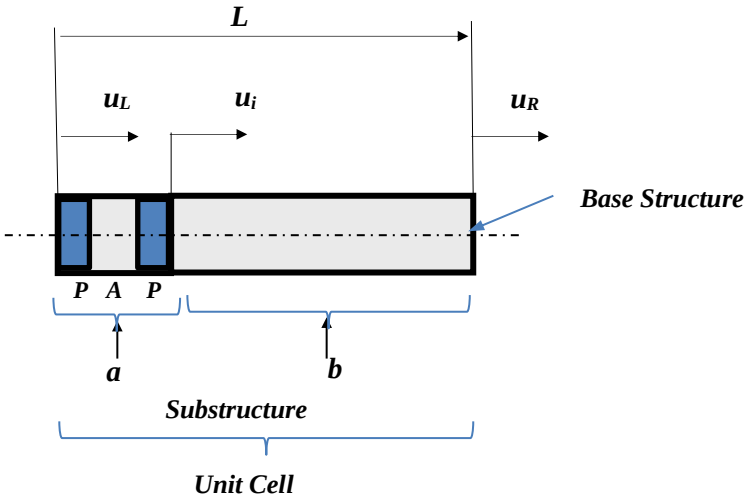

Figure 5.2 –Degrees of freedom of a unit cell of periodic polyurea composite (P = Polyurea, A = Aluminum)

This vector is condensed to support Bloch wave propagation theory. Hence, the displacements at the boundaries are related as follows:

$$u_R = e^{-ikL} u_L \tag{5.3}$$

where k and L denote the wave number and the length of the unit cell, respectively.

Hence, define an independent nodal deflection vector $\bar{u}$ such that:

$$\bar{u} = \begin{Bmatrix} u_L & u_i \end{Bmatrix}^T \tag{5.4}$$

The deflection vectors u and $\bar{u}$ are related as follows:

$$u = T\,\bar{u} \tag{5.5}$$

where T is a transformation matrix such as:

$$T = \begin{bmatrix} I & 0 & e^{-ikL}I \\ 0 & I & 0 \end{bmatrix}^T \tag{5.6}$$

Substituting equations (5.5) and (5.6) into equation (5.1), it reduces to:

$$\bar{M}\,\ddot{\bar{u}} + \bar{C}\,\dot{\bar{u}} + \bar{K}\,\bar{u} = \bar{F} \tag{5.7}$$

where $\bar{M} = T^* M T$, $\bar{C} = T^* C T$, $\bar{K} = T^* K T$, and $\bar{F} = T^* F$.

Equation (5.7) is now cast in the following state-space form (Meirovitch 2010; Hussein 2009; and Hussein and Frazier 2010):

$$\begin{bmatrix} 0 & \bar{M} \\ \bar{M} & \bar{C} \end{bmatrix} \dot{\bar{y}} + \begin{bmatrix} -\bar{M} & 0 \\ 0 & \bar{K} \end{bmatrix} \bar{y} = \begin{Bmatrix} 0 \\ \bar{F} \end{Bmatrix} \tag{5.8}$$

where $\bar{y} = \begin{Bmatrix} \dot{\bar{u}} & \bar{u} \end{Bmatrix}^T$. Assuming the state-space solution:

$$\bar{y} = e^{\lambda t}\hat{y} \tag{5.9}$$

This solution leads to the following eigenvalue problem:

$$\left(\begin{bmatrix} 0 & \bar{M} \\ \bar{M} & \bar{C} \end{bmatrix} \lambda + \begin{bmatrix} -\bar{M} & 0 \\ 0 & \bar{K} \end{bmatrix} \right) \hat{y} = 0 \tag{5.10}$$

which can be rewritten in the following compact and standard form:

$$A\hat{y} = \lambda\hat{y} \tag{5.11}$$

With the matrix A given by:

$$A = -\begin{bmatrix} 0 & \bar{M} \\ \bar{M} & \bar{C} \end{bmatrix}^{-1} \begin{bmatrix} -\bar{M} & 0 \\ 0 & \bar{K} \end{bmatrix} \tag{5.12}$$

Note that all the entries of the matrix *A* are function of the dimensionless wave number *kL*. Then, the eigenvalues of the matrix *A* can be determined for different values of the wave number *kL*. The eigenvalues λ_s are complex and generally assume the following form:

$$\lambda_s(kL) = -\zeta_s \omega_{rs} \pm i\omega_{ds} \qquad s = 1..., n \tag{5.12}$$

With ζ_s, ω_{rs}, and ω_{ds} denote the damping ratio, undamped resonant frequency, and damped resonant frequency, respectively.

Hence, damped resonant frequency and the damping ratio can be extracted as follows:

$$\omega_{ds} = imag\left(\lambda_s(kL)\right) \tag{5.13}$$

and

$$\zeta_s = -\frac{real\left(\lambda_s(kL)\right)}{\left|\lambda_s(kL)\right|} \tag{5.14}$$

Plotting the resonant frequency ω_{ds} against the wave number *kL*, gives the dispersion characteristics of the unit cell of the periodic polyurea. It further defines the zones of stop and pass bands as will be illustrated.

B. Numerical Examples

Figure 5.3 displays a typical blast wave form with a maximum normal force defined as F_{max} = 1000 *N*. The blast wave is assumed to be represented as follows (Barnhart IV, 2016):

$$F = F_{\max} e^{-\left(\frac{t-t_0}{t_d}\right)} \tag{5.15}$$

where t_0 = 0.5 *ms*, and t_d = 0.2 *ms*.

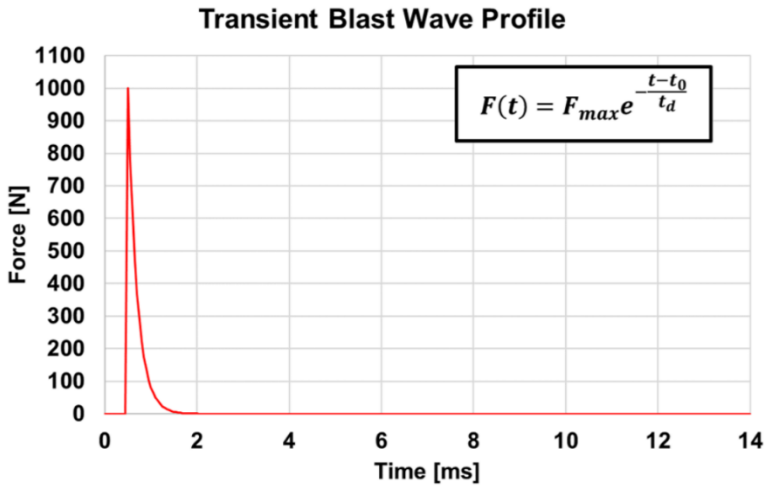

Figure 5.3 – Form of a typical blast wave form

5.2. Dispersion Curves

Determinant of matrix *A* can be set to zero to get the characteristics equation whose roots will give the propagation constant μ for any frequency ω .

Equation (2.35) can be written in the following state-space form:

$$\frac{d}{dx}\begin{Bmatrix} U \\ U_x \end{Bmatrix} = \begin{bmatrix} 0 & 1 \\ -k^2 & 0 \end{bmatrix} = A \begin{Bmatrix} U \\ U_x \end{Bmatrix}$$

Which has a solution:

$$\begin{Bmatrix} U \\ U_x \end{Bmatrix}_x = e^{Ax} \begin{Bmatrix} U \\ U_x \end{Bmatrix}$$

The above solution can be put in a transfer matrix form by setting $U_x = \frac{F}{EA}$ and extracting e^{Ax} using symbolic manipulation software to give:

$$\begin{Bmatrix} U \\ F/EA \end{Bmatrix}_x = \begin{bmatrix} \dfrac{1+e^{-2ikx}}{2e^{-ikx}} & \dfrac{1-e^{-2ikx}}{2ike^{-ikx}} \\ \dfrac{ik(1-e^{-2ikx})}{2ke^{-ikx}} & \dfrac{1+e^{-2ikx}}{2e^{-ikx}} \end{bmatrix} \begin{Bmatrix} U \\ F/EA \end{Bmatrix}$$

$$\begin{Bmatrix} U \\ F \end{Bmatrix}_x = \begin{bmatrix} \dfrac{1+e^{-2ikx}}{2e^{-ikx}} & \dfrac{1}{EA}\dfrac{1-e^{-2ikx}}{2ike^{-ikx}} \\ EA\dfrac{ik(1-e^{-2ikx})}{2ke^{-ikx}} & \dfrac{1+e^{-2ikx}}{2e^{-ikx}} \end{bmatrix} \begin{Bmatrix} U \\ F \end{Bmatrix} = [T] \begin{Bmatrix} U \\ F \end{Bmatrix}$$

Accordingly, the transfer matrix $[T]$ is given by in a more compact form as:

$$[T] = \begin{bmatrix} \cos(kx) & \dfrac{1}{z\omega}\sin(kx) \\ -z\omega sin(kx) & \cos(kx) \end{bmatrix}$$

$$where, z = A\sqrt{E\rho} = impedence\ of\ the\ bar$$

$[T]$ has the following two eigenvalues: $\lambda_1 = e^{-ikx}$ and $\lambda_2 = e^{ikx} = \lambda^{-1}$

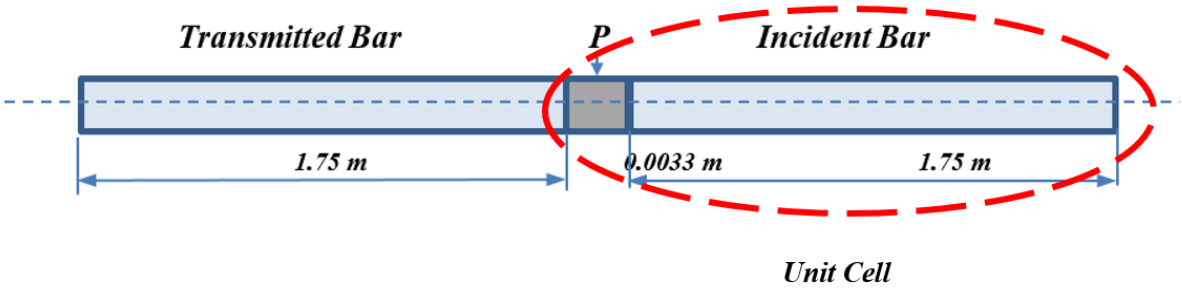

Figure 5.4 – Configuration I with Unit Cell

$$[T_s] = \begin{bmatrix} \cos(k_s L_s) & \dfrac{1}{z_s\omega}\sin(k_s L_s) \\ -z_s\omega sin\,(k_s L_s) & \cos(k_s L_s) \end{bmatrix} with\ s = Incident\ bar, Polyurea$$

Combining the transfer matrices of the substructures of Incident Bar (IB) and Polyurea (P) for Configuration I, yields the transfer matrix $[T]$ for the unit cell as follows:

$$[T_{cell}] = [T_P][T_{IB}]$$

and for the complete rod $[T_{rod}] = [T_{cell}]^{N_{cell}}$

$$where\ N_{cell} = Number\ of\ cells\ in\ the\ structure$$

From the eigenvalue problem (5.10), we can determine the propagation parameter, μ, which is related to the eigenvalue by $\lambda = e^{\mu}$.

By definition of the hyperbolic cosine,

$$e^{\mu} + e^{-\mu} = 2\cosh\mu$$

Thus, solving for μ leads to

$$\mu = Arc\cosh\left[\frac{e^{\mu}+e^{-\mu}}{2}\right] = Arc\cosh\left[\frac{\lambda+\lambda^{-1}}{2}\right] = \alpha + i\beta$$

where, $\mu = Propagation\ Constant$

$$\alpha = The\ logarithmic\ decay$$

$$\beta = Phase\ difference\ between\ the\ Adjacent\ Cells$$

5.3. Pass-band and Stop-band Mapping

An efficient way for representing the geometrical and physical characteristics of the Polyurea composites on the width of the stop and pass bands are presented. The contours of the stop and pass bands are plotted for different values of frequency.

5.4. Analysis of Dispersion curves and Pass-band and Stop-band Mapping

From Figure 5.5 through 5.13 we notice that the eigenvalues of the transfer matrix appear as complex conjugate for all frequencies below the cut-off frequency of the cell. From frequencies above the cut-off frequency, the eigenvalues appear in real reciprocal pairs.

Further, we may notice that the imaginary part varies from 0 to π then it stays constant for the frequency values at which the real part is non-zero. It indicates the presence of damping in the periodic rod that has resulted in eliminating the pass bands completely and extended the stop band over the higher frequency band (greater than 2900 Hz for configuration I).

Note that the width and location of the stop and pass bands depends primarily on the physical and geometrical properties of the periodic rod.

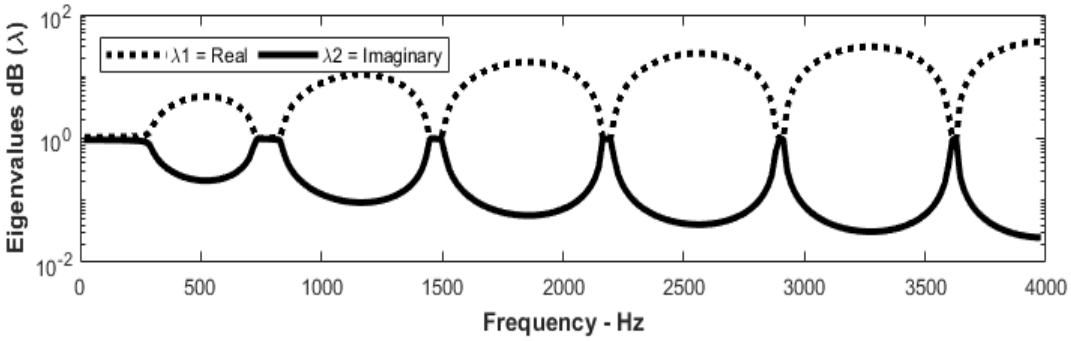

Figure 5.5 – Pass and Stop Bands-Configuration I [$N_{cell} = 1$]

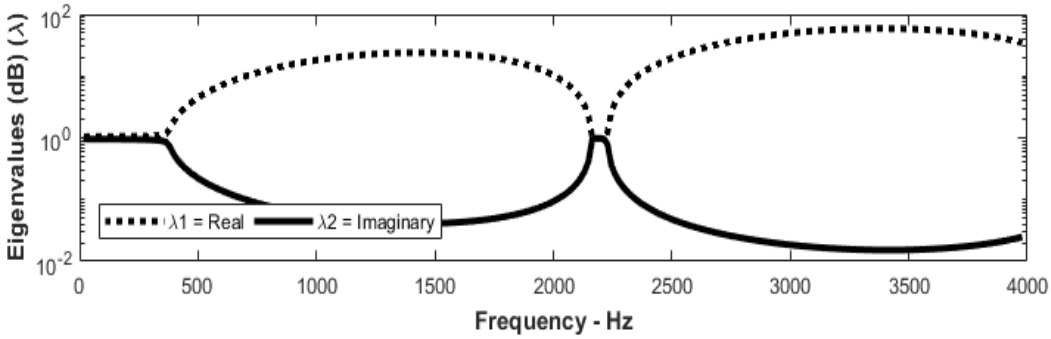

Figure 5.6 – Pass and Stop Bands-Configuration II [$N_{cell} = 1$]

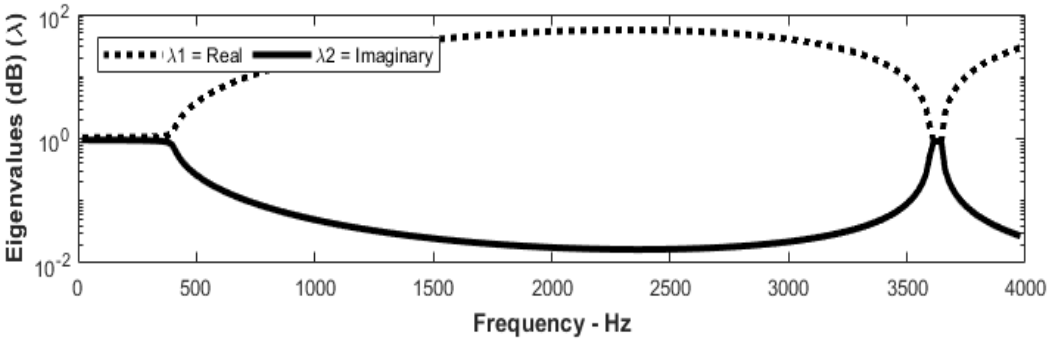

Figure 5.7 –Pass and Stop Bands-Configuration III [$N_{cell} = 1$]

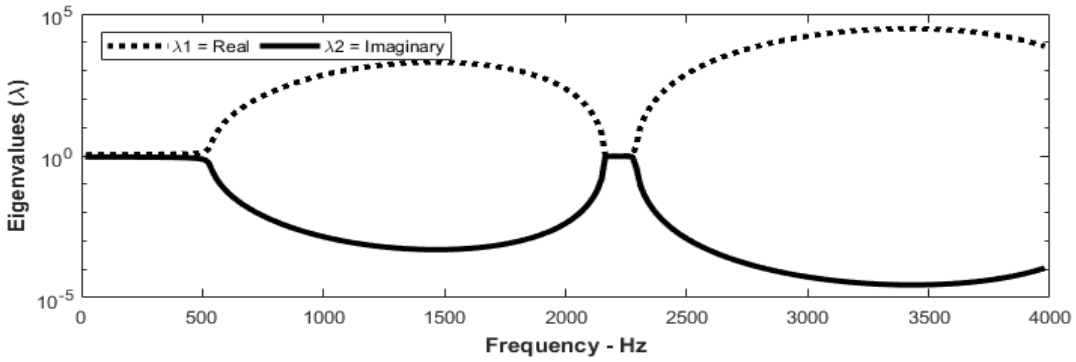

Figure 5.8 –Pass and Stop Bands-Configuration I [$N_{cell} = 2$]

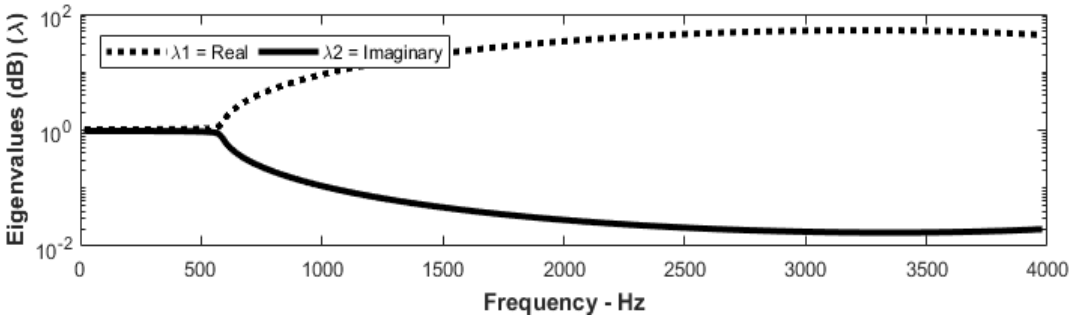

Figure 5.9 –Pass and Stop Bands-Configuration II [$N_{cell} = 2$]

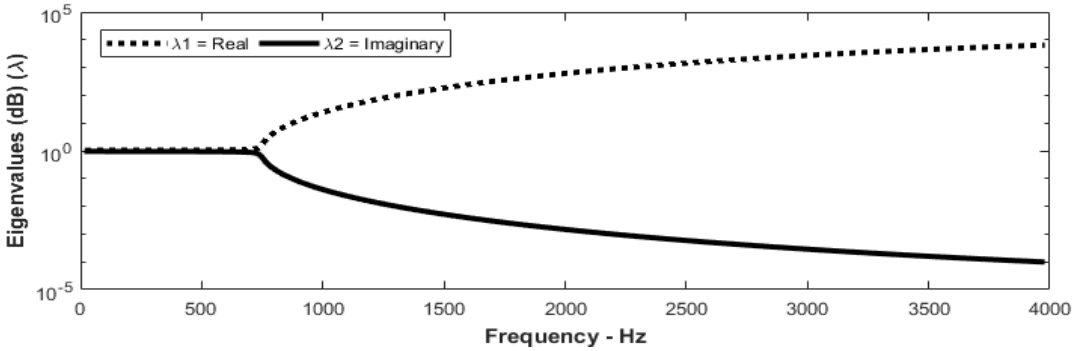

Figure 5.10 –Pass and Stop Bands-Configuration III [$N_{cell} = 2$]

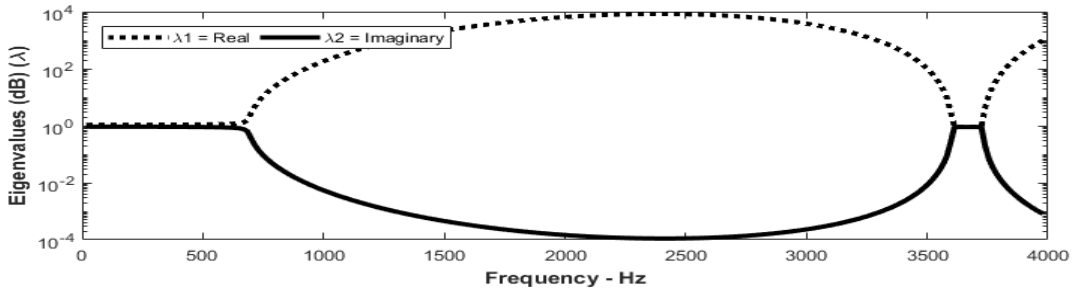

Figure 5.11 –Pass and Stop Bands-Configuration I [$N_{cell} = 3$]

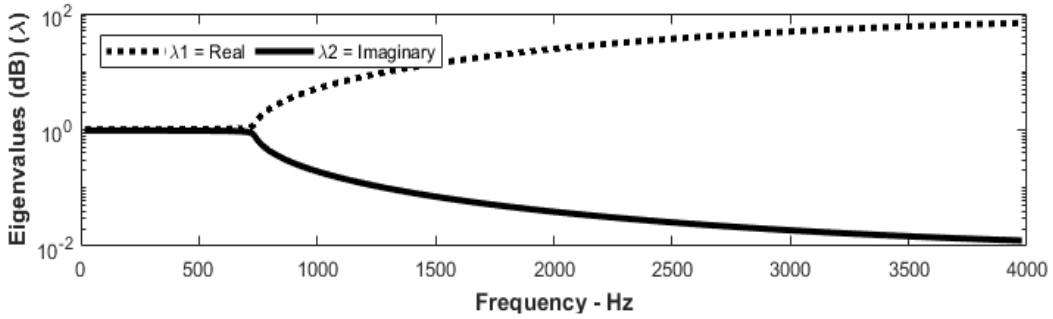

Figure 5.12 –Pass and Stop Bands-Configuration II [$N_{cell} = 3$]

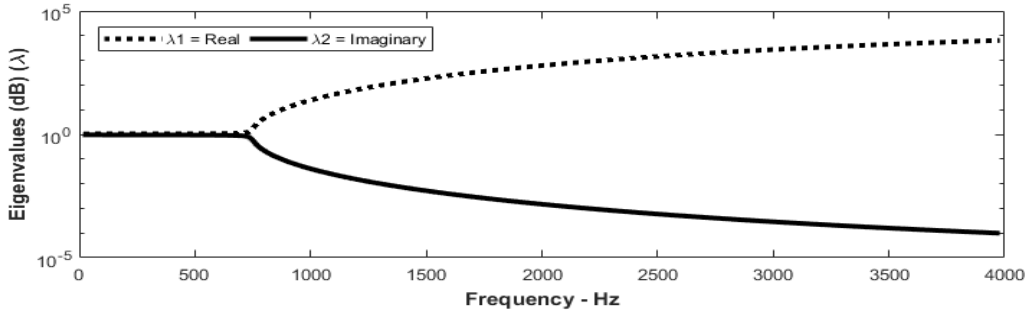

Figure 5.13 –Pass and Stop Bands-Configuration III [$N_{cell} = 3$]

Figures 5.14 through 5.16 show the comparison of magnitude of the eigenvalues of the transfer matrix as function of the frequency for Configurations I, II and III with increased periodic cells from 1 to 3. Figure 5.14 shows for only a single periodic cell for configuration I, the passive system

has a pass band for frequency less than 270 Hz, and a stop band for frequency greater than 270 Hz. In other words, the system acts as a "low pass" filter with a cut-off frequency of 270 Hz. The pass and stop band frequencies are being shifted to a higher value as we increase the number of periodic cells in figure 5.15 and figure 5.16 for all three configurations.

It also shows the increase of the stop bands as we increase the layers of polyurea and aluminum and a decrease in pass bands in higher frequencies.

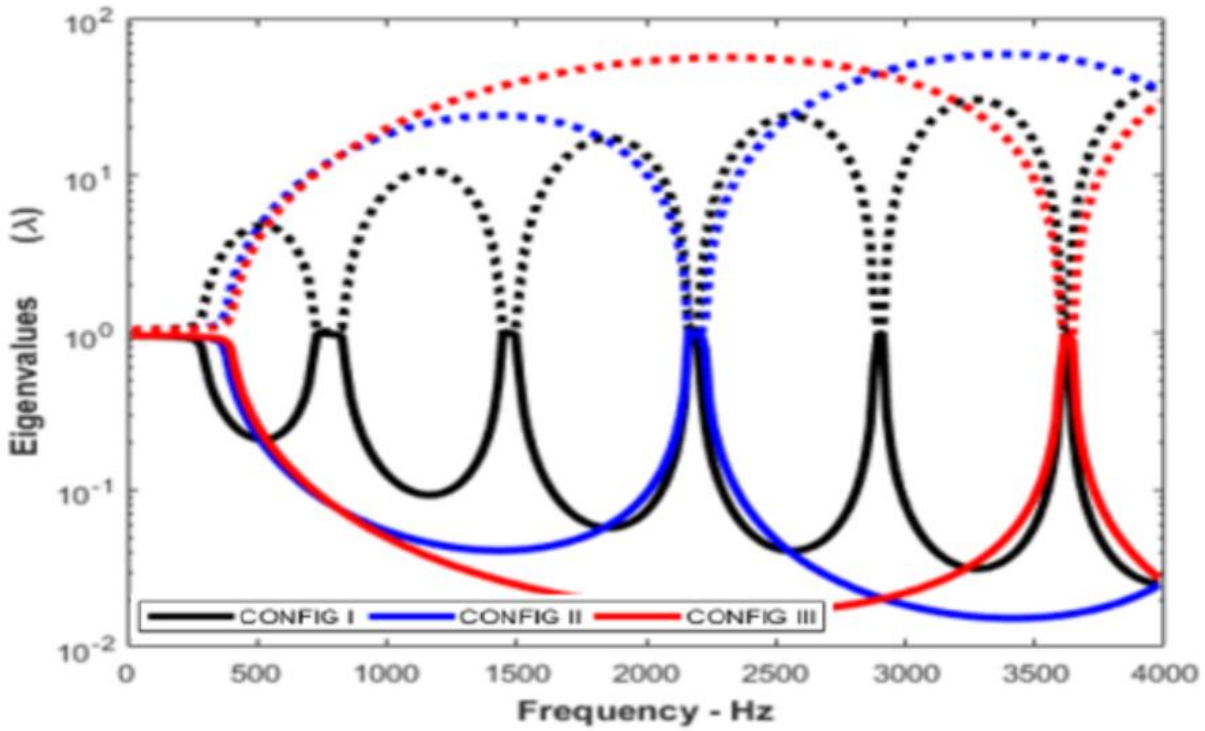

Figure 5.14 –Comparison of Pass and Stop Bands-Configuration I, II and III [$N_{cell} = 1$]

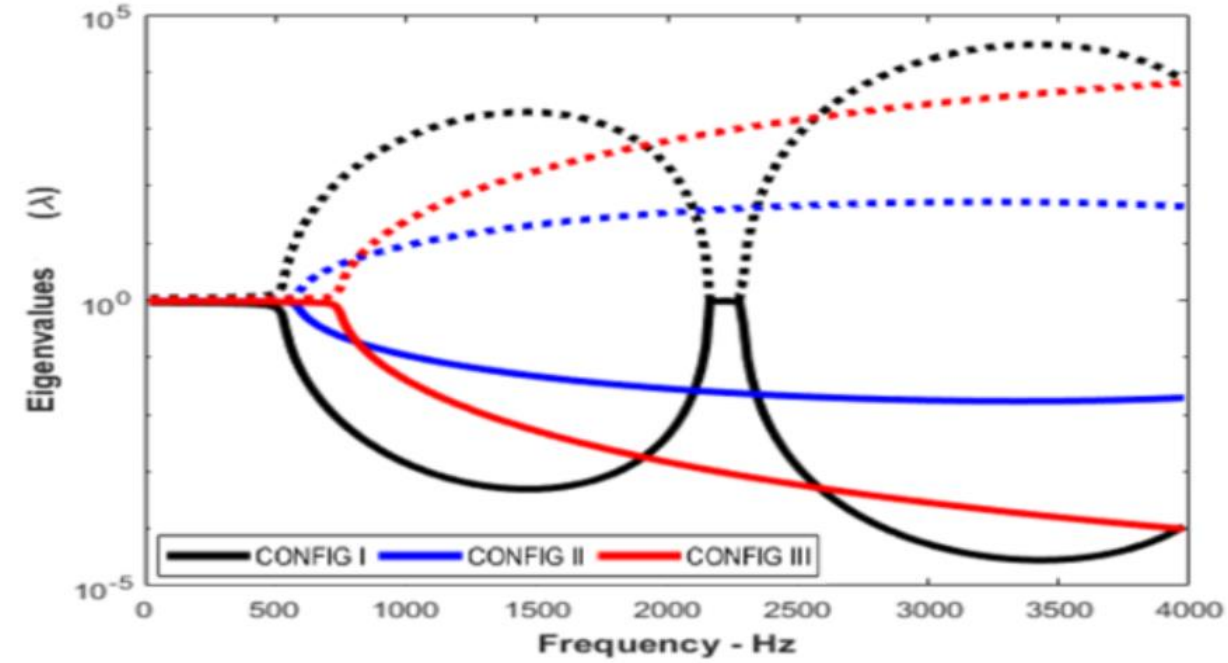

Figure 5.15 –Comparison of Pass and Stop Bands-Configuration I, II and III [$N_{cell} = 2$]

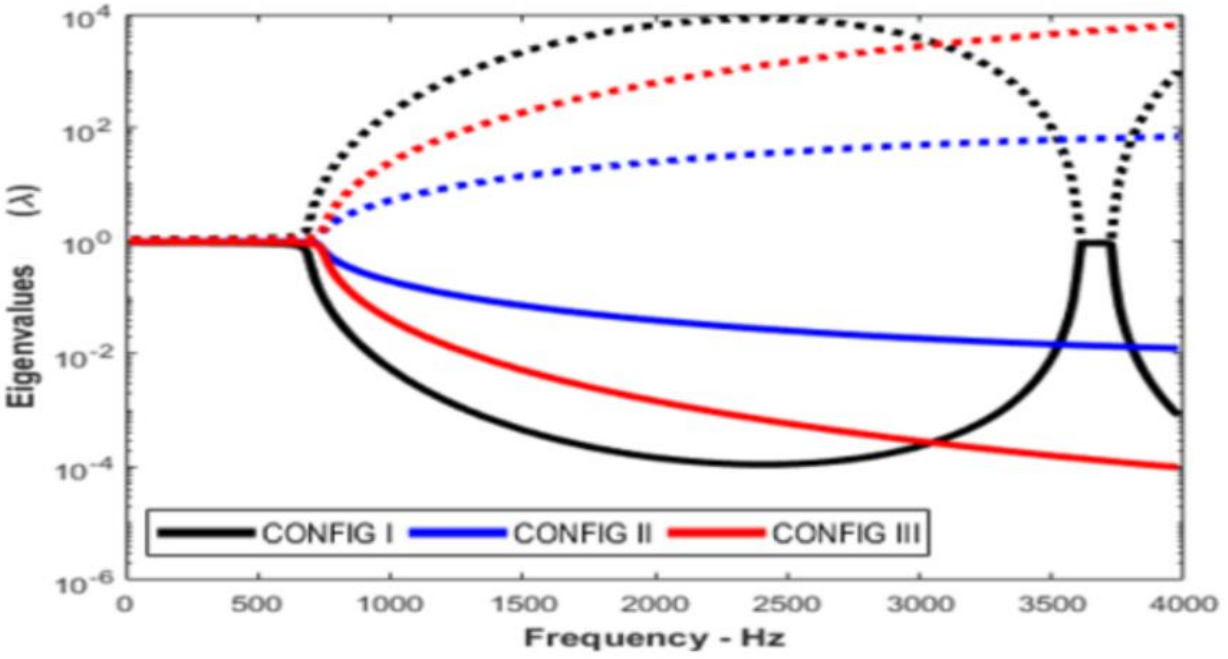

Figure 5.16 –Comparison of Pass and Stop Bands - Configuration I, II and III [$N_{cell} = 3$]

Figure 5.17 through 5.25 presents plot for the variation of the real and imaginary parts of the propagation factor μ. Here the real part of the propagation factor is equal to zero for all frequency values below the cut-off frequency and continuous curve corresponds to the imaginary wavenumbers that are associated with waves that propagate or pass band modes. The dashed black line corresponds to the purely real wavenumbers, which do not propagate. The black solid curve corresponds to the imaginary wavenumbers that are associated with waves that propagate or pass band modes. The non-linearity of the curves indicates that the medium is dispersive for frequency values that make the wavenumber complex, the amplitude of the displacement is attenuated exponentially.

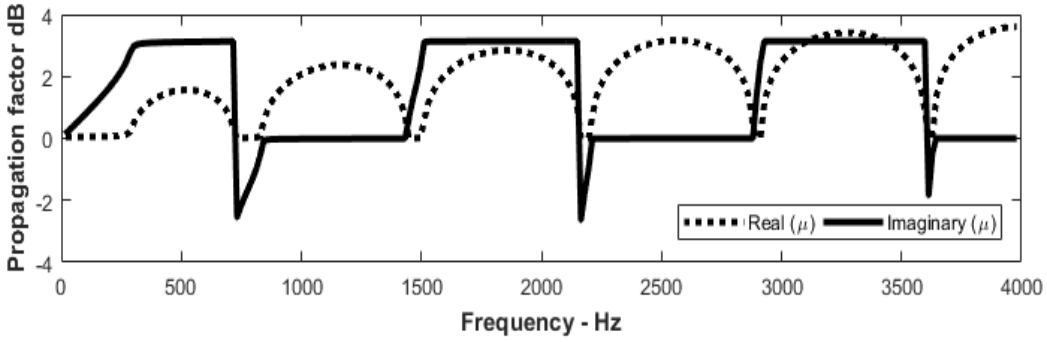

Figure 5.17 – Propagation Factor- Configuration I [$N_{cell} = 1$]

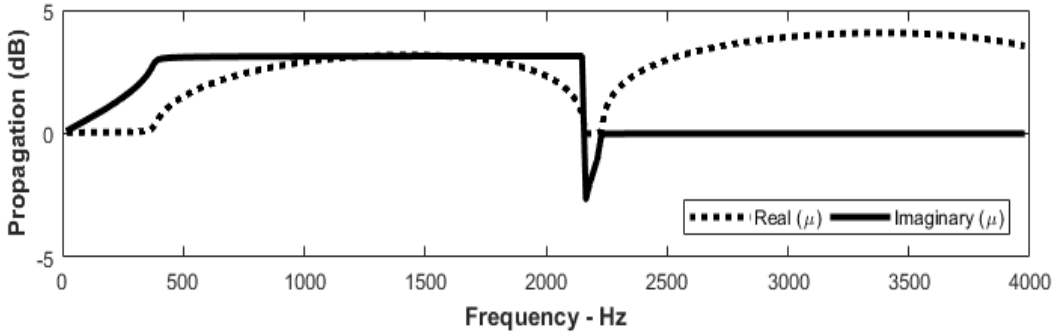

Figure 5.18 –Propagation Factor- Configuration II [$N_{cell} = 1$]

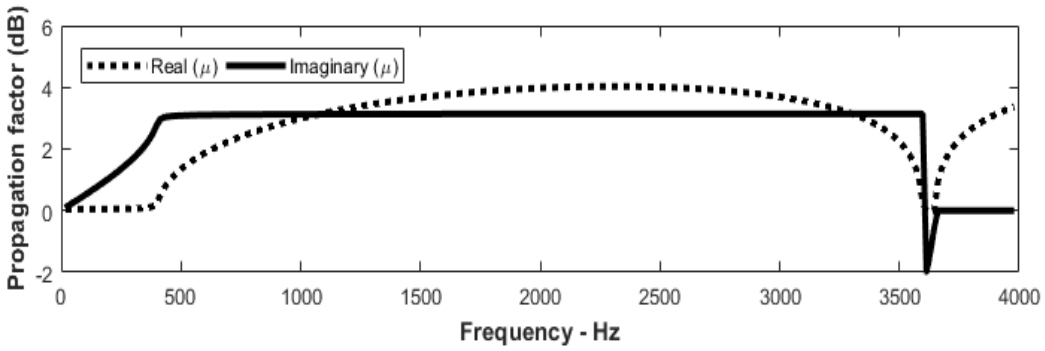

Figure 5.19 –Propagation Factor- Configuration III [$N_{cell} = 1$]

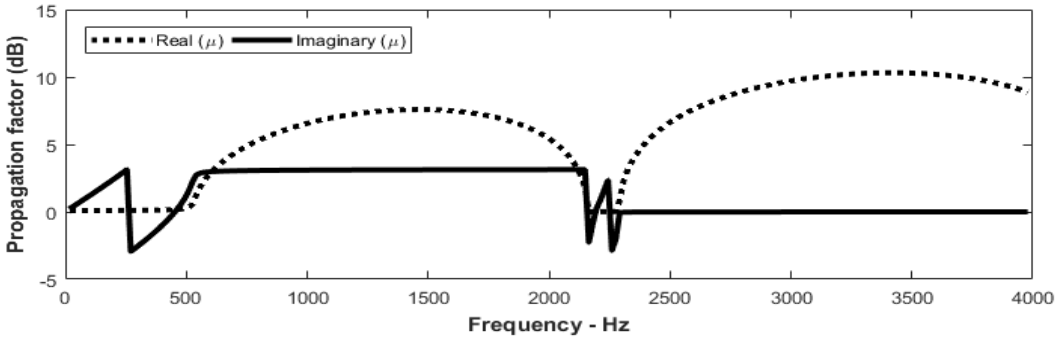

Figure 5.20 –Propagation Factor- Configuration I [$N_{cell} = 2$]

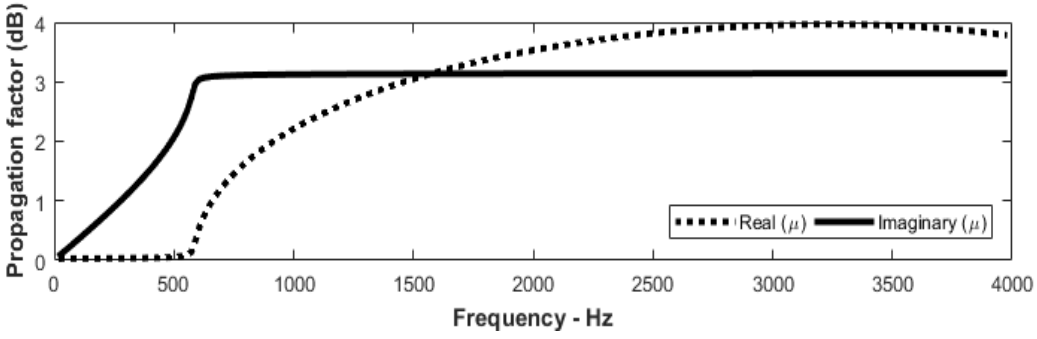

Figure 5.21 –Propagation Factor- Configuration II [$N_{cell} = 2$]

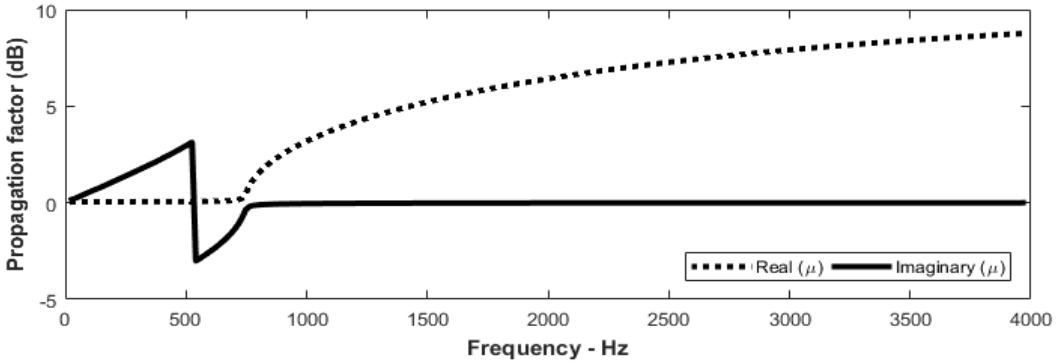

Figure 5.22 –Propagation Factor- Configuration III [$N_{cell} = 2$]

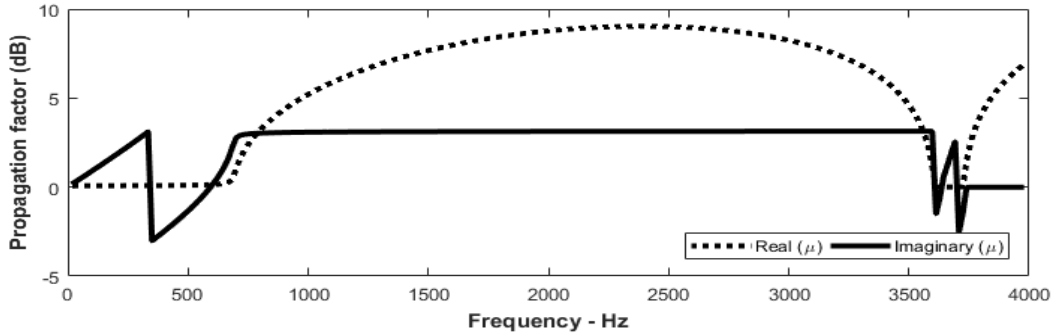

Figure 5.23 –Propagation Factor- Configuration I [$N_{cell} = 3$]

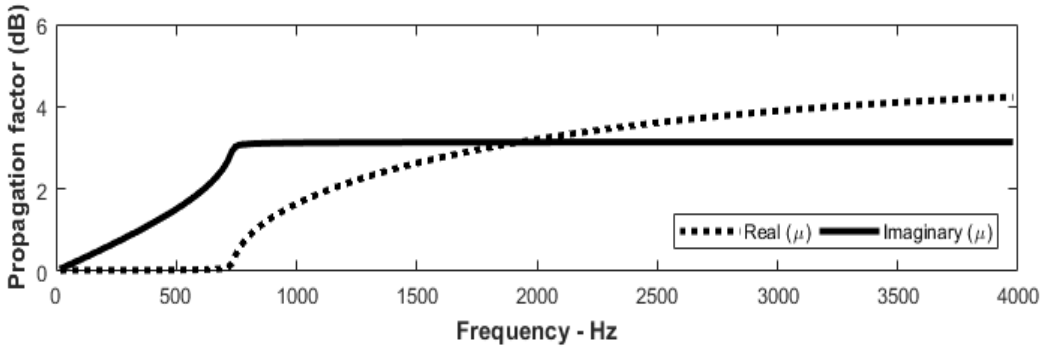

Figure 5.24 –Propagation Factor- Configuration II [$N_{cell} = 3$]

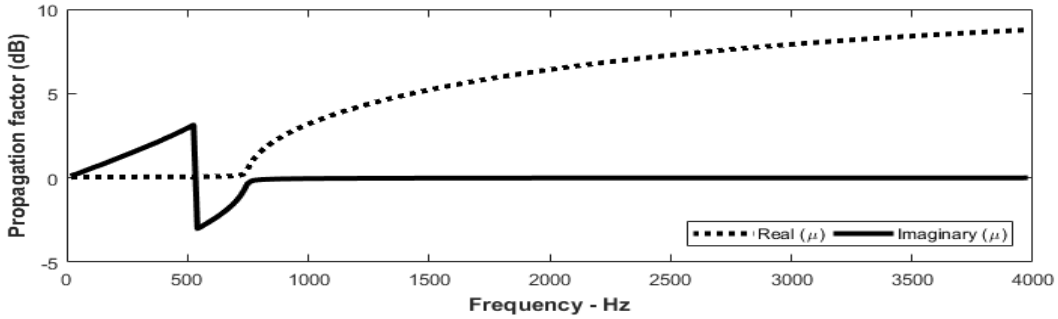

Figure 5.25 –Propagation Factor- Configuration III [$N_{cell} = 3$]

Figure 5.26 through 5.28 show the comparison of Propagation Factor for Configurations I, II and III with increased periodic cells from 1 to 3. A clear observation from these figures are that, the imaginary part varies from 0 to π and vice versa at the frequency band in which the real part is zero. Also, the imaginary part is constant with values of π or 0 when the frequency bands in which the real part is positive.

Frequency less than 270 Hz for configuration I (black solid line), the attenuation parameter $\alpha = 0$, i.e. the system has no apparent damping. This results in complete propagation of the waves or a "pass band". But a frequency greater than 270 Hz, the attenuation parameter $\alpha \neq 0$, i.e. the system has an apparent damping that results in attenuating the propagation of waves in a manner equivalent to the presence of actual damping. This occurs over a broad frequency range which is called a "stop band". Under these conditions, the system behaves as a "low pass filter".

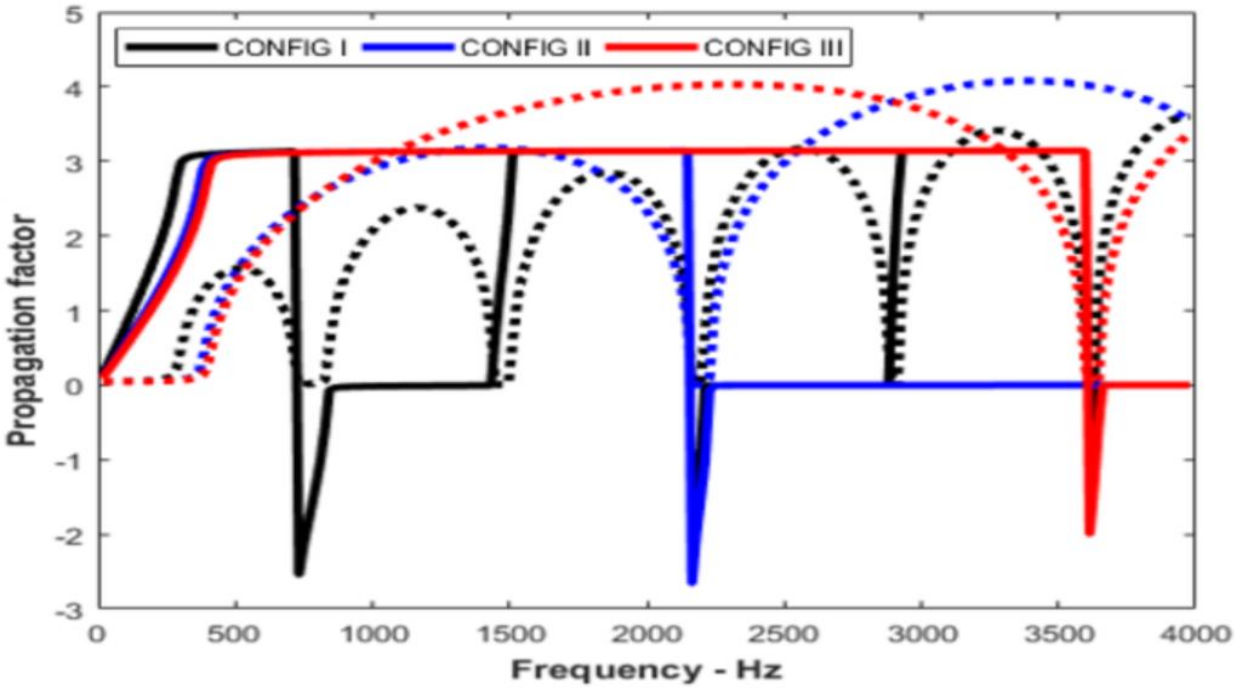

Figure 5.26 –Comparison of Propagation Factor- Configuration I, II and III [$N_{cell} = 1$]

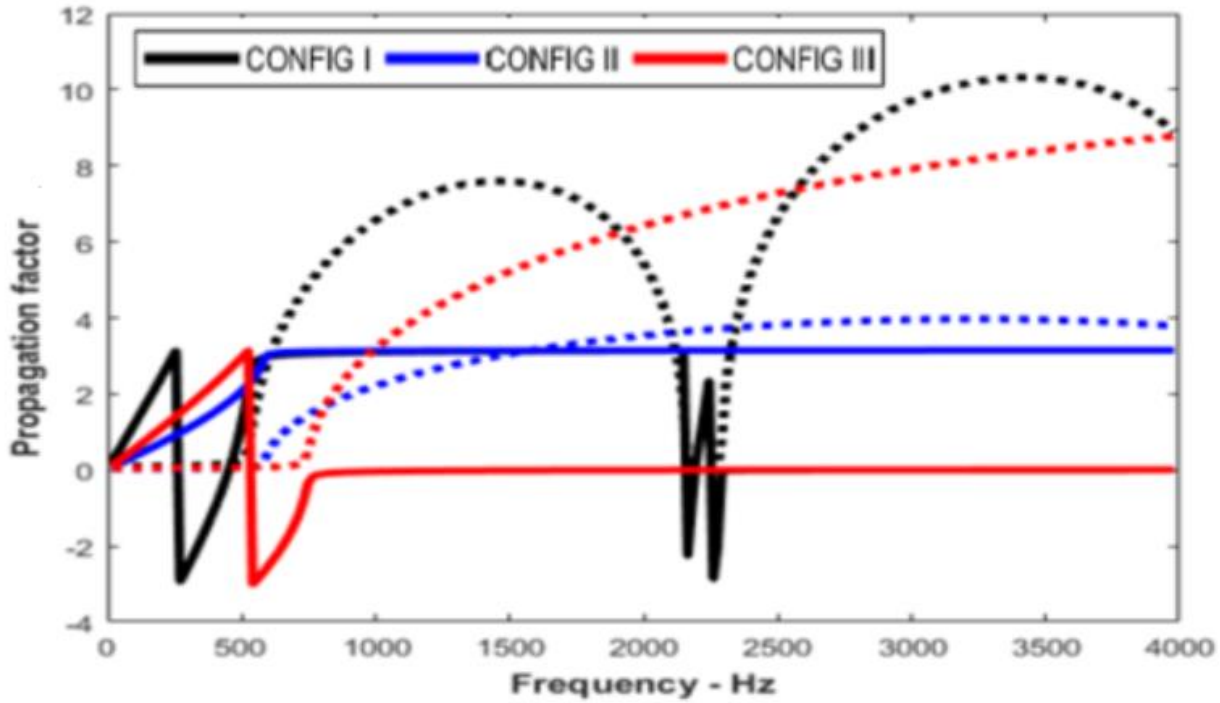

Figure 5.27 –Comparison of Propagation Factor- Configuration I, II and III [$N_{cell} = 2$]

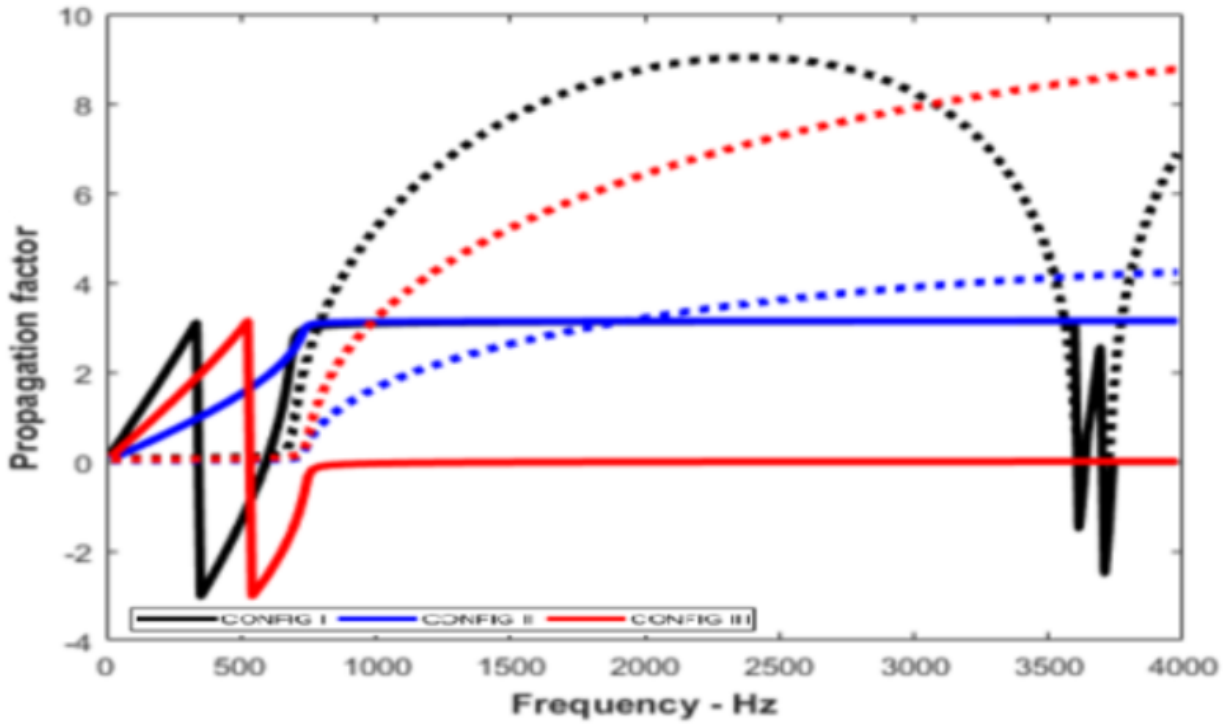

Figure 5.28 –Comparison of Propagation Factor- Configuration I, II and III [$N_{cell} = 3$]

Figures 5.29 through 5.37 is a plot of the frequency response of the unit cell. In this plot, we note that the response of the cell becomes less than unity (0 dB) for higher frequencies.

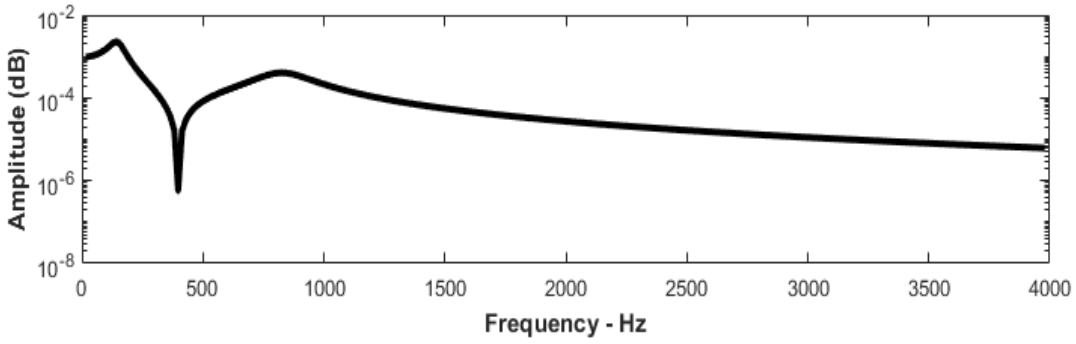

Figure 5.29 – Frequency Response of a single Cell for Configuration I [$N_{cell} = 1$]

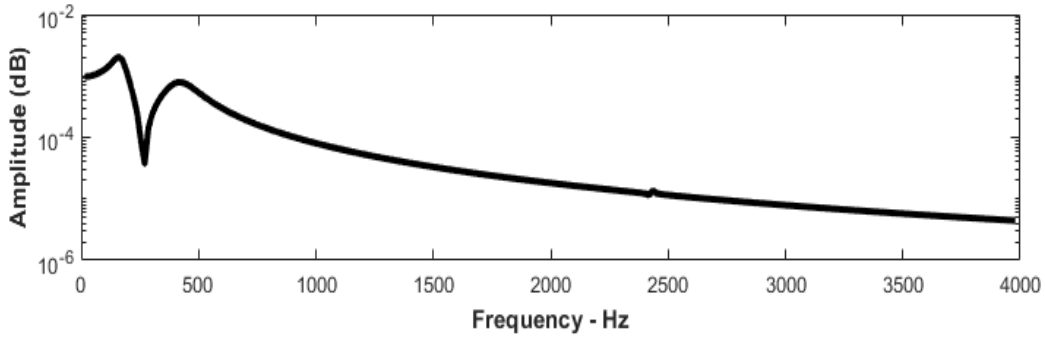

Figure 5.30 – Frequency Response of a single Cell for Configuration II [$N_{cell} = 1$]

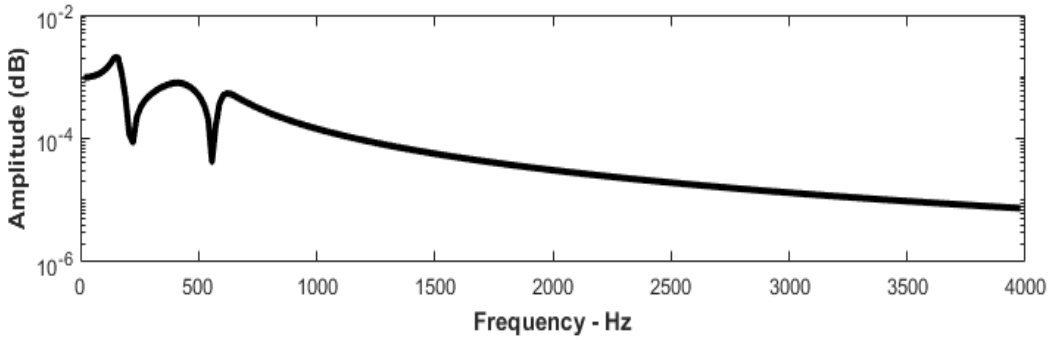

Figure 5.31 – Frequency Response of a single Cell for Configuration III [$N_{cell} = 1$]

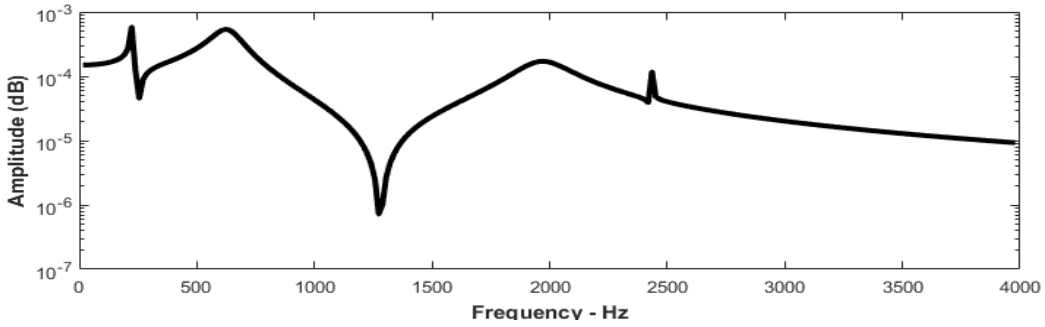

Figure 5.32 – Frequency Response for Configuration I [$N_{cell} = 2$]

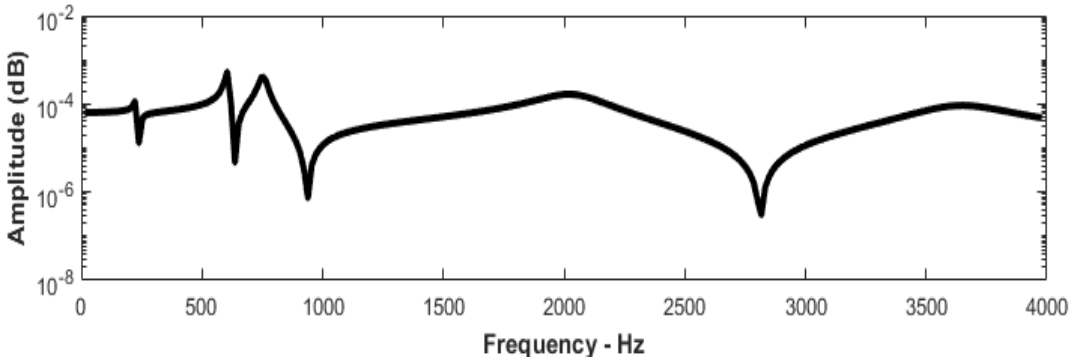

Figure 5.33 – Frequency Response for Configuration II [$N_{cell} = 2$]

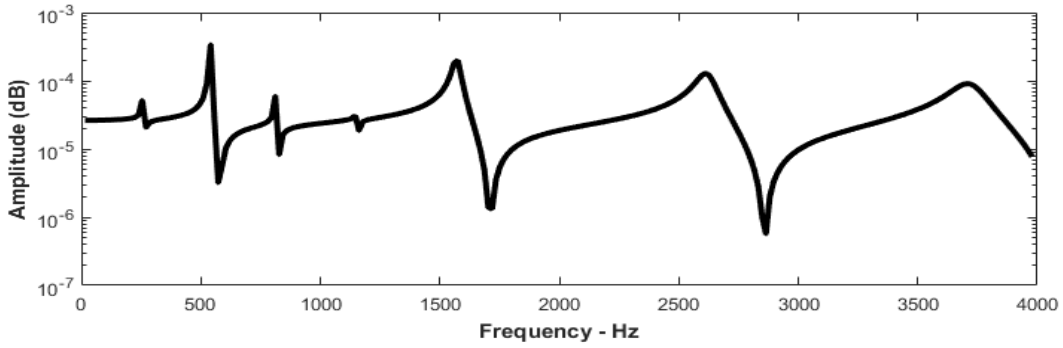

Figure 5.34 – Frequency Response for Configuration III [$N_{cell} = 2$]

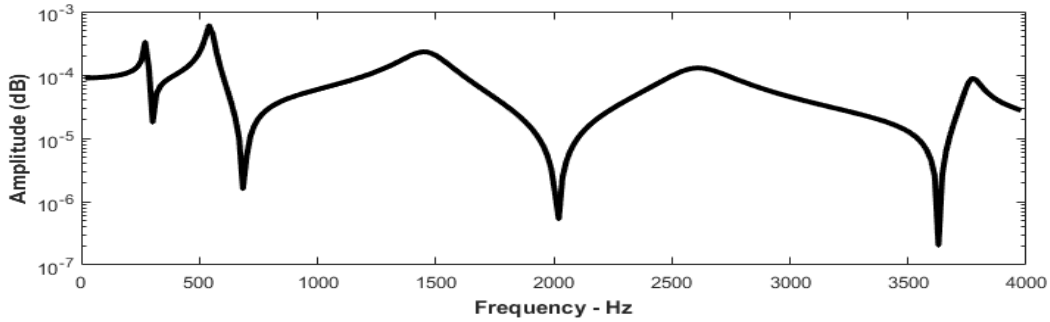

Figure 5.35 – Frequency Response for Configuration I [$N_{cell} = 3$]

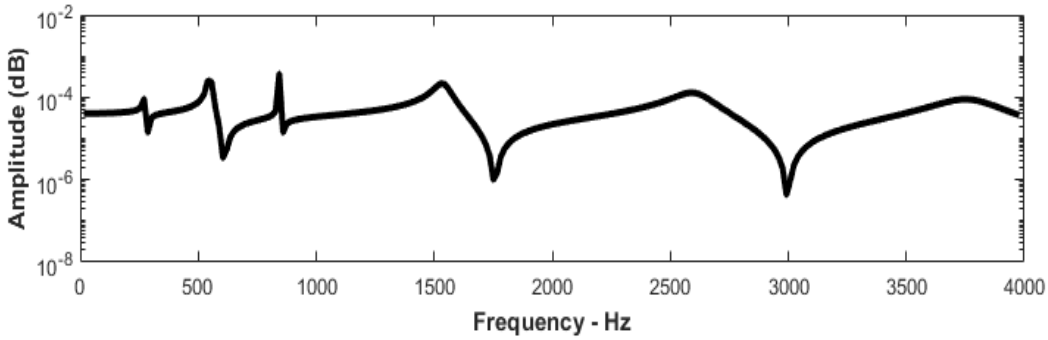

Figure 5.36 – Frequency Response for Configuration II [$N_{cell} = 3$]

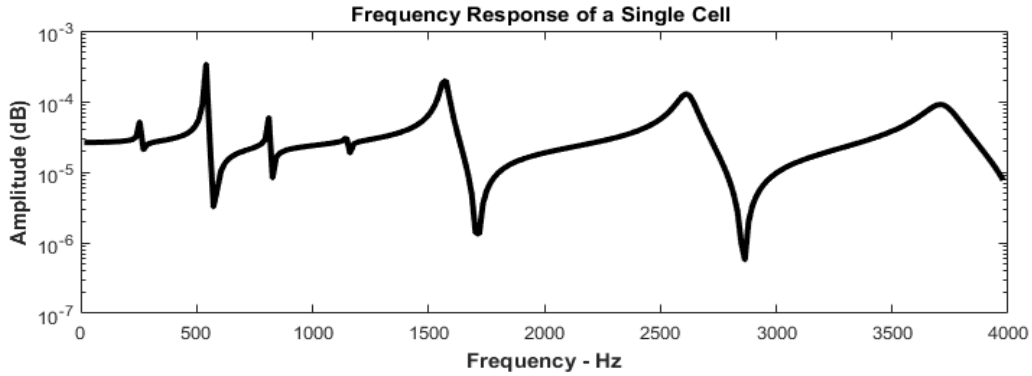

Figure 5.37 – Frequency Response for Configuration III [$N_{cell} = 3$]

Figures 5.38 through 5.40 show the comparison of Frequency Response for Configurations I, II and III with increased periodic cells from 1 to 3. From figure 5.56, It is clear that, the amplitude is decreasing to a factor of 2 as we increase polyurea and aluminum layer with same number of periodic cells and after that the increase is not much significant. On the other hand, frequency is increasing as we are increasing the number of periodic cells from 1 to 3. The natural frequencies of different configurations lie within the pass bands of the periodic rod.

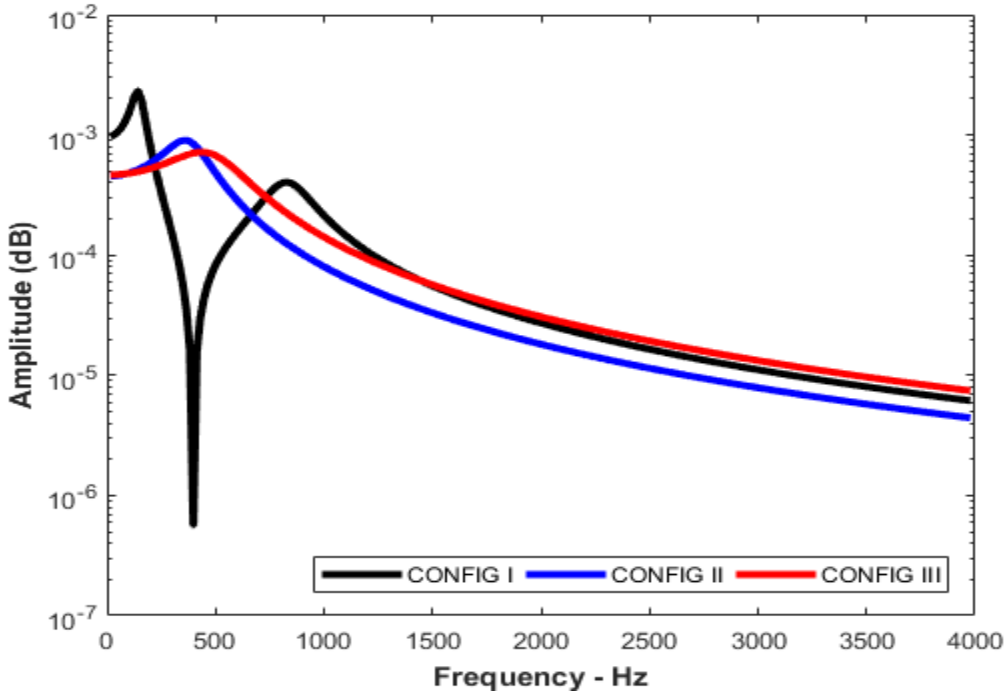

Figure 5.38 –Comparison of Frequency Response for Configuration I, II and III [$N_{cell} = 1$]

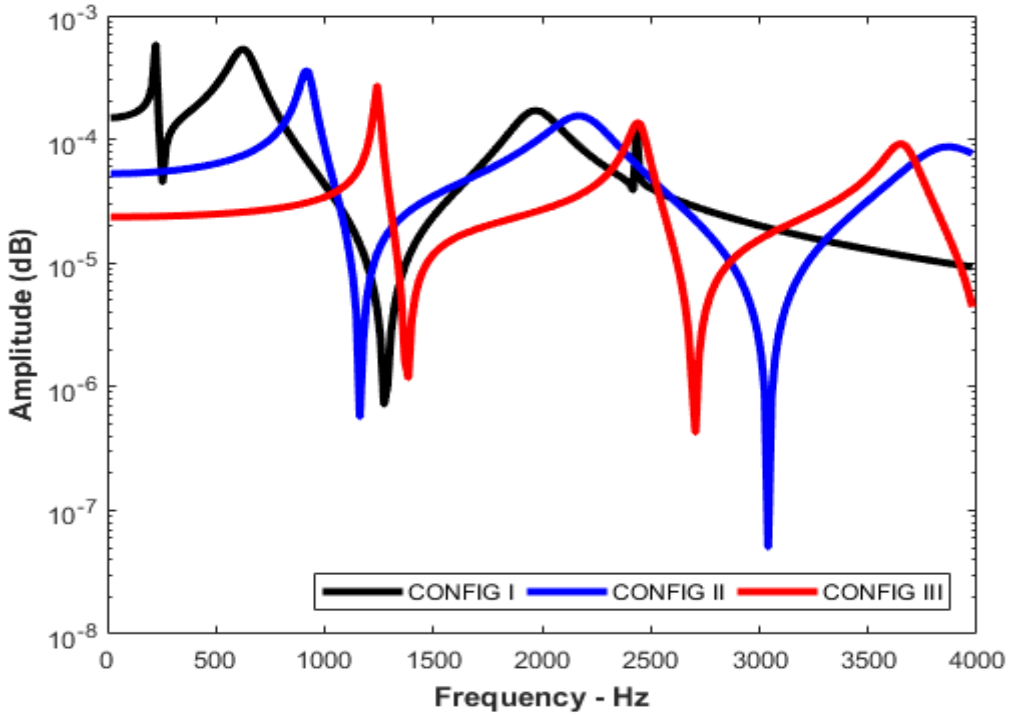

Figure 5.39 –Comparison of Frequency Response for Configuration I, II and III [$N_{cell} = 2$]

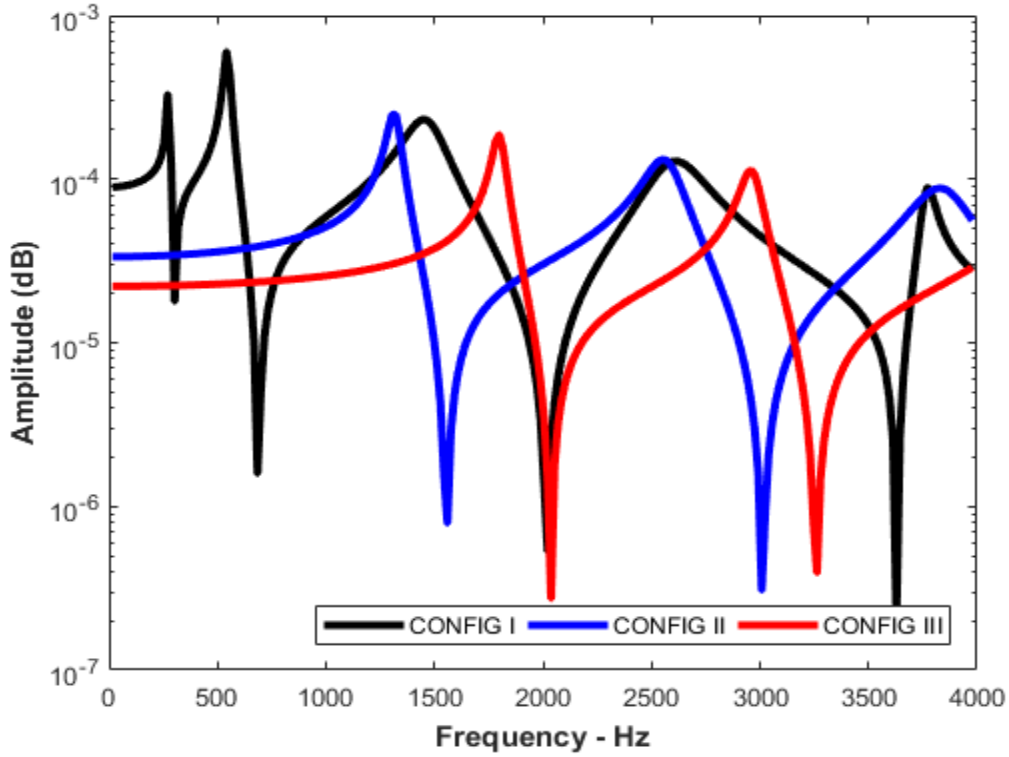

Figure 5.40 –Comparison of Frequency Response for Configuration I, II and III [$N_{cell} = 3$]

Time response of a unit cell is shown in Figure 5.41, where we can see the displacement is slowly becoming zero once the impact load hits the Incident bar by the Striker bar.

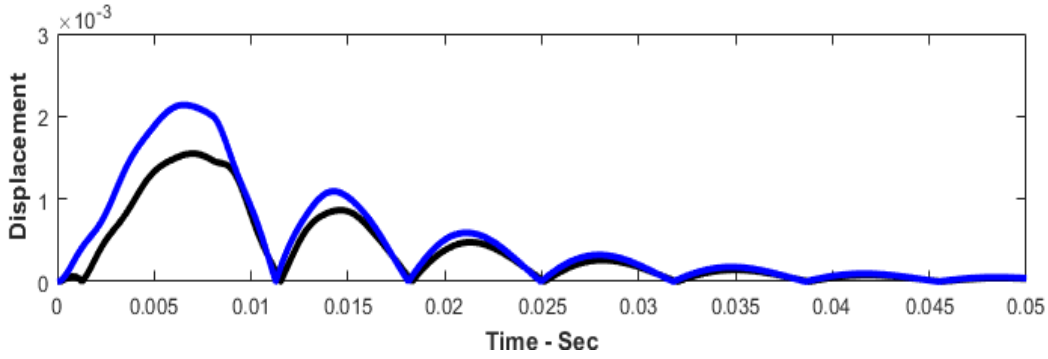

Figure 5.41 – Time Response of a single Cell for Configuration I [$N_{cell} = 1$]

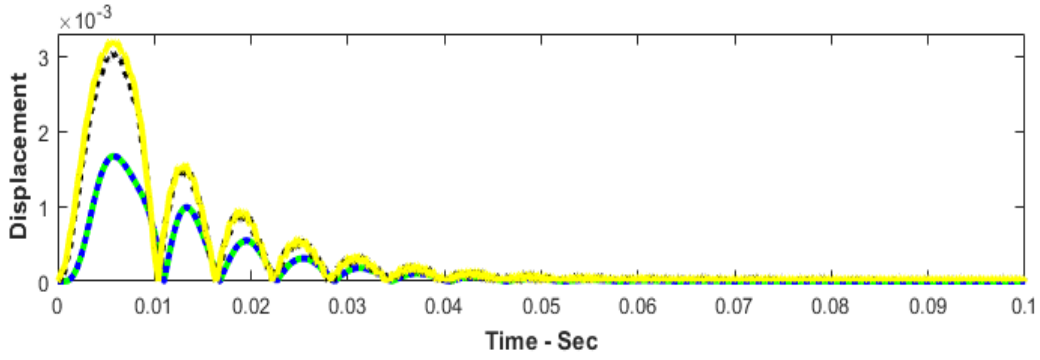

Figure 5.42 – Time Response of a single Cell for Configuration II [$N_{cell} = 1$]

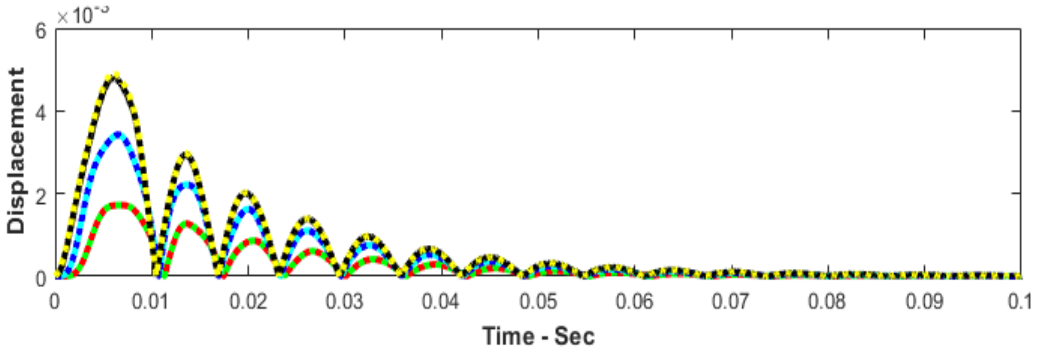

Figure 5.43 – Time Response of a single Cell for Configuration III [$N_{cell} = 1$]

The displacement is decreasing to the order of 2 and fast approaching zero as we increased the periodic cell units from 1 to 3 as evident from Figures 5.42, 5.43 and 5.44 through 5.49.

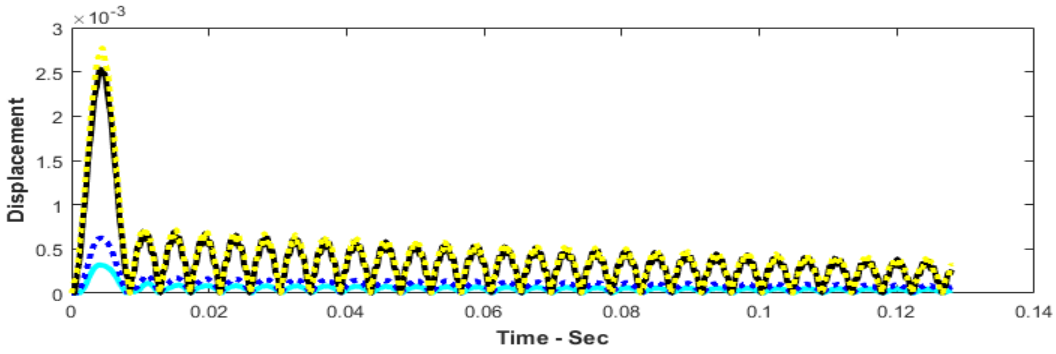

Figure 5.44 – Time Response for Configuration I $[N_{cell} = 2]$

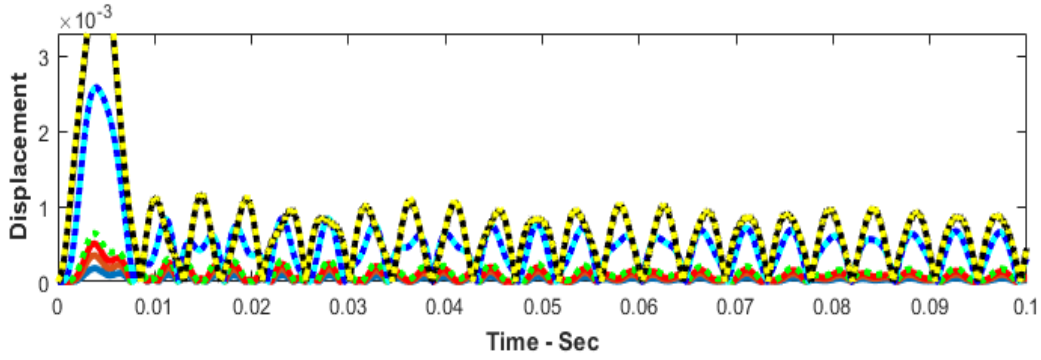

Figure 5.45 – Time Response for Configuration II $[N_{cell} = 2]$

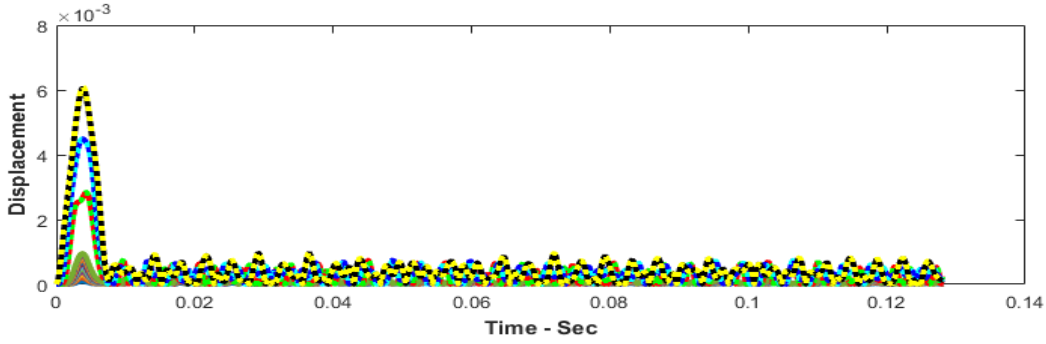

Figure 5.46 – Time Response for Configuration III $[N_{cell} = 2]$

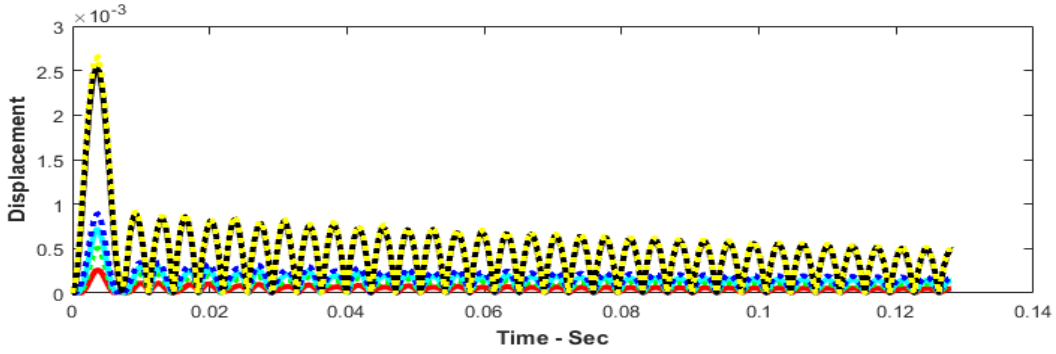

Figure 5.47 – Time Response for Configuration I [$N_{cell} = 3$]

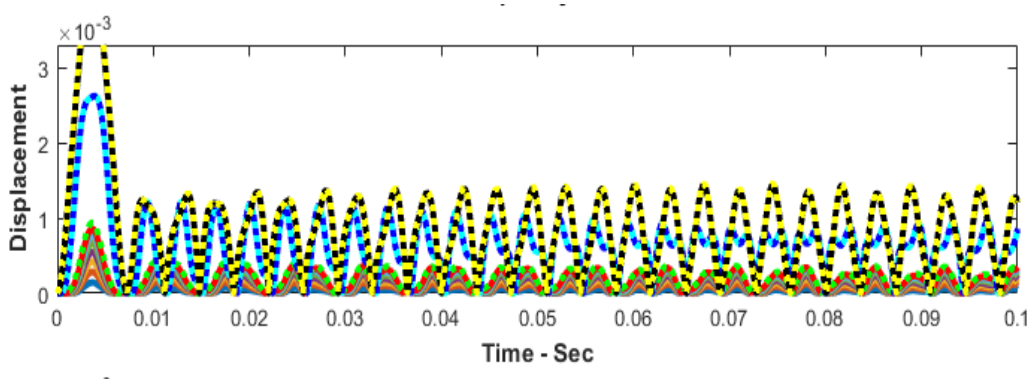

Figure 5.48 – Time Response for Configuration II [$N_{cell} = 3$]

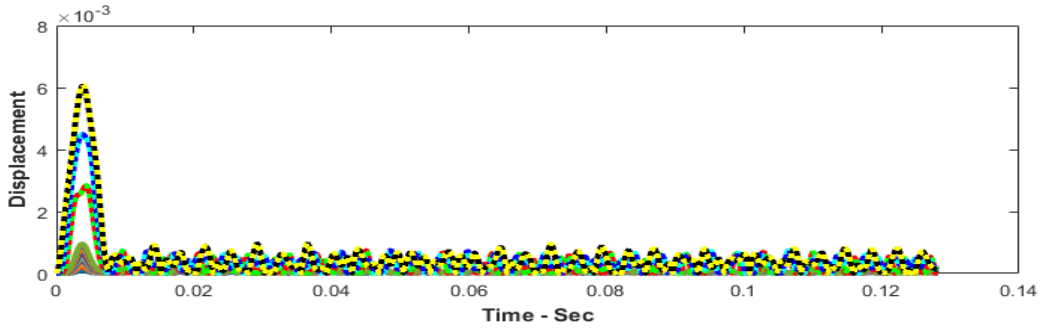

Figure 5.49 – Time Response for Configuration III [$N_{cell} = 3$]

Figures 5.50 through 5.58 are drawn which shows the strain response between two adjacent nodes. Only a single strain gage was used for configuration I with $\boldsymbol{N_{cell} = 1}$ and two strain gages were used for the rest of the configurations I, II and III with $\boldsymbol{N_{cell} = 1}$, $\boldsymbol{N_{cell} = 2}$ and $\boldsymbol{N_{cell} = 3}$. The time domain strain signals of the two gages were obtained and transformed to the frequency domain using the Fast Fourier Transform to yield the strain response.

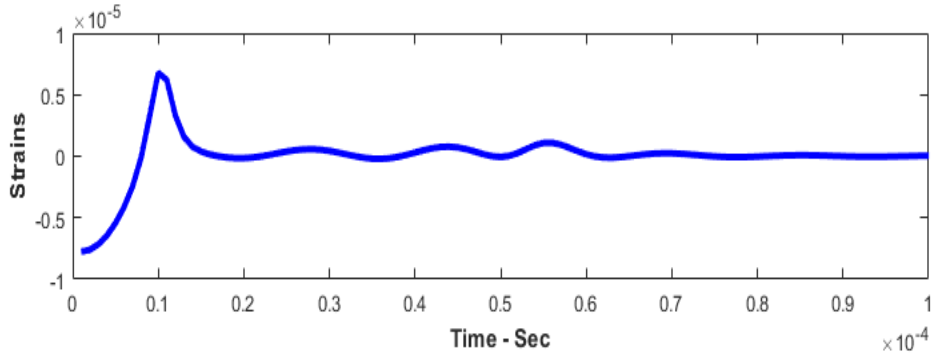

Figure 5.50 – Strain Response of a single Cell for Configuration I $[\boldsymbol{N_{cell} = 1}]$

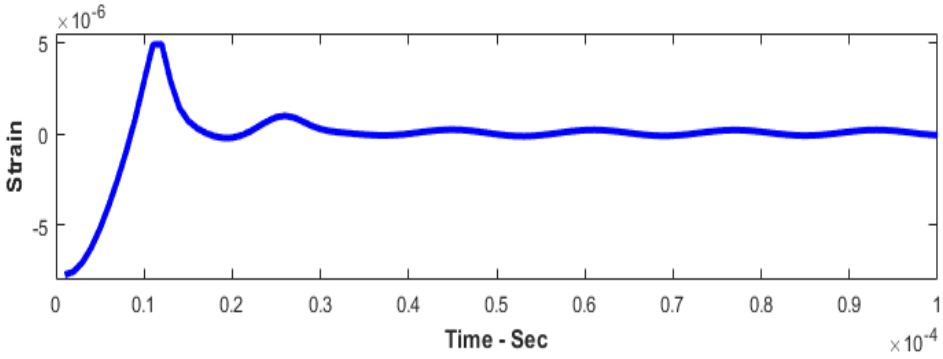

Figure 5.51 – Strain Response of a single Cell for Configuration II $[\boldsymbol{N_{cell} = 1}]$

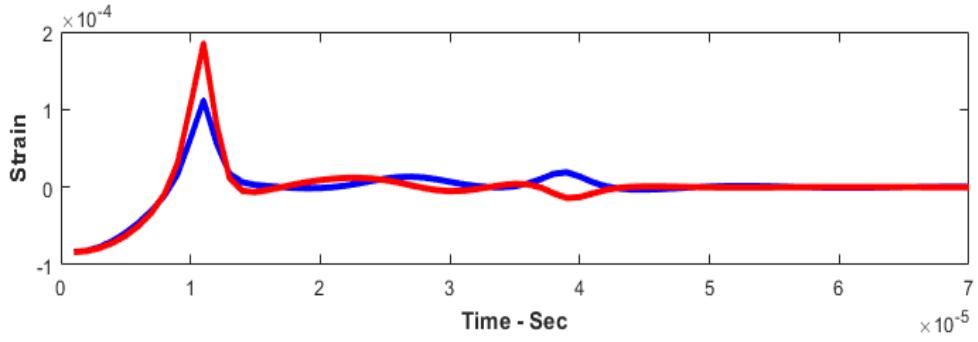

Figure 5.52 – Strain Response of a single Cell for Configuration III [$N_{cell} = 1$]

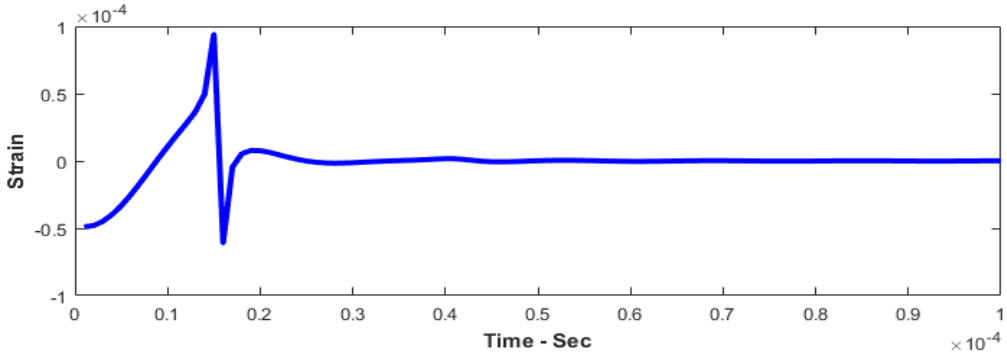

Figure 5.53 – Strain Response for Configuration I [$N_{cell} = 2$]

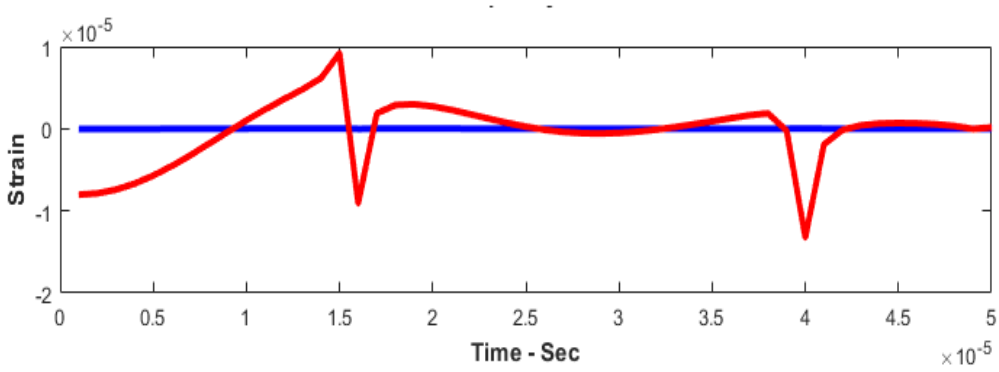

Figure 5.54 – Strain Response for Configuration II [$N_{cell} = 2$]

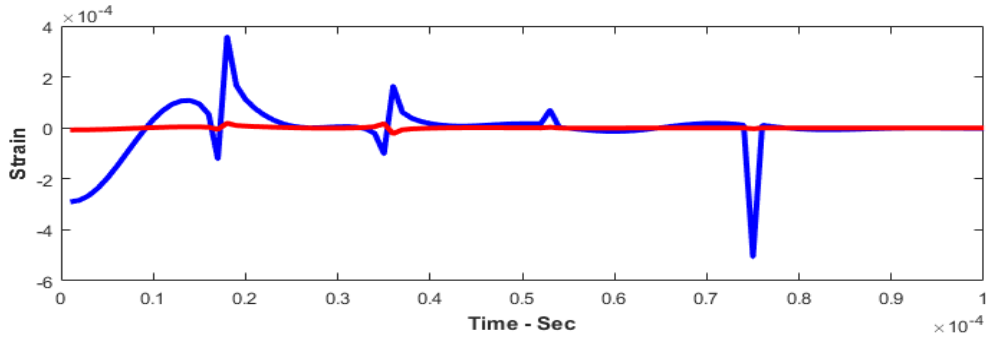

Figure 5.55 – Strain Response for Configuration III [$N_{cell} = 2$]

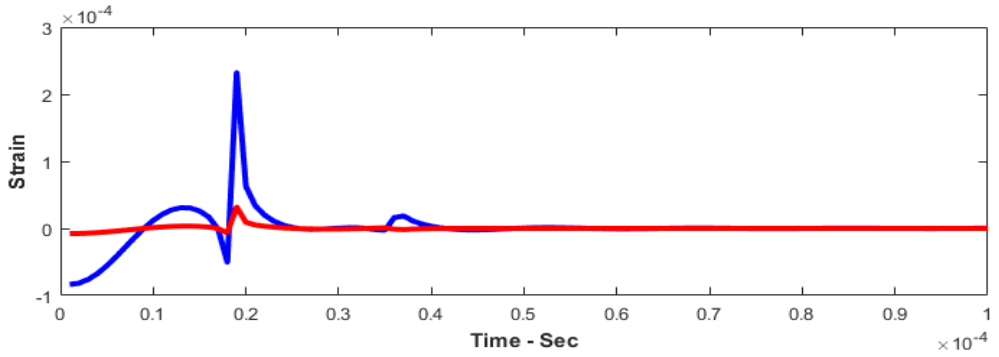

Figure 5.56 – Strain Response for Configuration I [$N_{cell} = 3$]

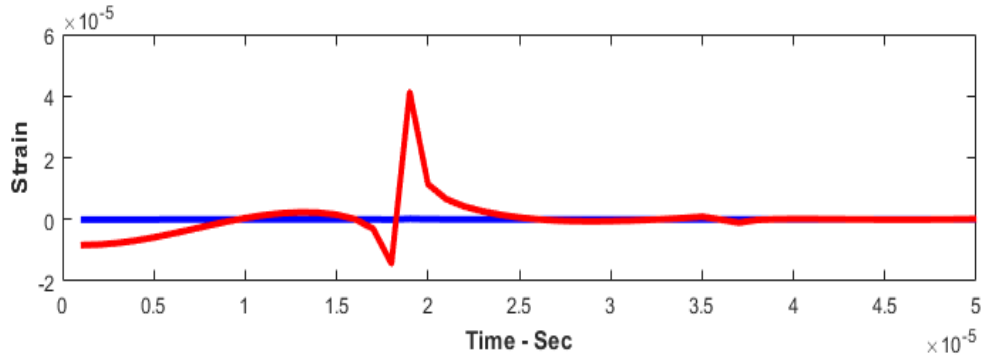

Figure 5.57 – Strain Response for Configuration II [$N_{cell} = 3$]

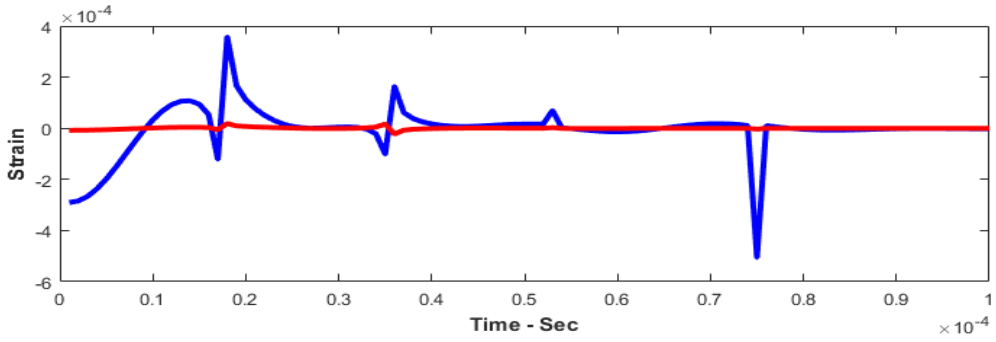

Figure 5.58 – Strain Response for Configuration III [$N_{cell} = 3$]

5.5. SUMMARY

This chapter has presented the theory of periodic structures in an attempt to determine the pass and stop band characteristics of these structures using the transfer matrix approach and Bloch wave theory. The approach is applied to various configurations of the periodic polyurea composites to demonstrate the effectiveness and filtering capabilities of the proposed configurations in mitigating the effect of blast waves on the wave propagation characteristics. This analysis shows that wave scattering and dispersion are phenomena due to the periodical arrangement of the structure and material properties.

Chapter 6

CONTRIBUTIONS, CONCLUSIONS AND FUTURE WORK

6.1. Major Contributions of the Dissertation

This dissertation has presented the concept of polyurea composites with periodic inserts that have built-in sources of local resonance along with their performance characteristics.

The comprehensive presentation of the periodic polyurea composites through mathematical modeling, experimental realization and evaluation demonstrates the effectiveness of these composites in mitigating the effect of high strain rate loading. Such effectiveness is attributed to the use of properly stacked layers of polyurea and metallic inserts that are designed in a periodic manner. An analytical approach consists of extracting the variation of propagation constants with excitation frequency was modeled by solving a classical eigenvalue problem with dynamic stiffness matrices of different polyurea composite configurations.

The developed theoretical finite element models which are integrated with the "Golla-Hughes-McTavish" approach enable the predictions of the response both in the time and frequency domains. Furthermore, the implemented approach enables the predictions of the band gap mapping characteristics of periodic polyurea composites when coupled with Bloch wave propagation theory. Such a comprehensive model will enable us to characterize mechanical dynamic behavior and to apply a valid design criteria of different viscoelastic composite structures. This is considered the major contribution of this dissertation.

6.2. Conclusions

This dissertation presented a comprehensive theoretical and experimental study of the characterization of various configurations of polyurea composites under high strain loading by using Split Hopkinson Pressure Bar (*SHPB*). These characteristics are predicted theoretically by developing a comprehensive finite element model using the Golla-Hughes-Mctavish (*GHM*) approach in order to describe the damping behavior of the polyurea in the time domain. The predictions of the *FEM* model are validated against the predictions of the commercial software package *ANSYS*. Further validations are carried out against experimental characterization of prototypes of configurations of the polyurea composites by using the Split Hopkinson Pressure Bar (*SHPB*) technique.

Close agreements are established between the theoretical predictions and the obtained experimental results.

In Chapter 1, step by step development of the Split Hopkinson Pressure Bar technique including critical review of the experimental technique in chronological order was presented. In addition to the different experimental techniques, effects of specimen dimensions and geometry as well as wave propagation were also discussed.

Literature reviews related to polyurea and its dynamic characterization including rate-dependent stress-strain behavior of polyurea, use of sensitive piezoelectric strain gauges, introduction of power law to describe non-linear stress-strain behavior, effects of pore size to wall thickness and random distribution of polyurea pores, use of laser-generated stress waves, and behavior of polyurea coated composite aluminum plates under high velocity projectile impact were also presented.

In Chapter 2, general dynamic behavior of viscoelastic materials like creep and stress relaxation were discussed and equations describing these properties were summarized.

In Chapter 3, the motivation behind the development of the finite element modeling (*FEM*) is discussed which is based on using the Golla-Hughes-Mctavish (*GHM*) approach to model the viscoelastic behavior of the polyurea. The developed *FEM* method is employed to simulate the dynamics of the SHPB to enable the computation of the incident and transmitted wave strains. These strains are employed to extract the stresses and strains experienced by the polyurea composites.

In Chapter 4, the experimental characterization of the polyurea composites are determined by using the Split Hopkinson Pressure Bar (*SHPB*). The experimental results are utilized to validate the predictions of the developed theoretical *FEM* and *ANSYS*. Close agreements are observed between the experiments and the predictions of the *FEM* and *ANSYS*.

In Chapter 5, the developed *FEM* model is extended and applied to periodic polyurea composite structures. The analytical results and the comprehensive parametric study demonstrate the influence of unit cell size and thickness of the polyurea composite layers in controlling the dynamics of wave propagation in rods. In addition, the obtained results provide a guideline for designing viscoelastic composites that are capable of filtering out selected excitation frequency ranges and the bandwidth of the gaps through proper adjustments of the number of unit cells and different composite configurations.

6.3. Recommendations for Future Studies

Despite the fact that this dissertation has presented a theoretical and experimental study of the fundamentals and the underlying phenomena governing the operation of Split Hopkinson Pressure Bar (*SHPB*) to characterize the dynamic behavior of Polyurea, it has opened also the door

for few more problems that can be considered as a natural extension to the presented study. For example, this dissertation has been limited to the study of basic structural elements such as rods. Therefore, a natural extension of this work is to consider using more complex structures like beams, plates and shales and use different polymeric incident and transmitted bars to characterize different viscoelastic materials. This will enable the study of dynamic behavior of viscoelastic material in higher strain rate scale inside automobiles, helicopters, aircraft, and other types of structures.

The present study has been limited to structure which is excited with a step load. An extension of this work can deal with structures which are subjected to sinusoidal excitation. Active periodic structures can also be used with tunable characteristics by introducing impedance mismatch. Future work also requires experimental validation of the periodic structures for realistic application of vibration isolation devices and parts in aerospace and automotive industries.

6.4. SUMMARY

This chapter summarizes the major contributions of this dissertation, conclusions on each chapters and recommendations for future work which may be carried out to further characterize the effects of impact loads on strain rates with different viscoelastic materials.

References

[1] B. Hopkinson, 1914, “A method of measuring the pressure produced in the detonation of high explosives or by the impact of bullets”, *Philosophical Transactions of the Royal Society of London. Series A,* Vol. 213, pp. 437-456.

[2] J. W. Landon and H. Quinney, 1923, “Experiments with the Hopkinson pressure bar”, *Philosophical Transactions of the Royal Society of London. Series A,* Containing Papers of a Mathematical or Physical Character, 103, pp. 622-643.

[3] R. Davies, 1948, “A critical study of the Hopkinson pressure bar”, *Philosophical Transactions of the Royal Society of London. Series A, Mathematical and Physical Sciences,* Vol. 240, pp. 375-457.

[4] H. Kolsky, 1949, “An investigation of the mechanical properties of materials at very high rates of strain”, *Proceedings of the Physical Society. Section B,* Vol. 62, pp. 676-700.

[5] K. Dharan and F. Hauser, 1970, “Determination of Stress-Strain characteristics at very high strain rates”, *Experimental Mechanics,* Vol. 10, Issue 9, pp. 370–376

[6] B. A. Gama *et al*., 2004, “Hopkinson bar experimental technique: A critical review”, *Appl. Mech Rev,* Vol. 57, No. 4, pp. 223-249.

[7] L. Pochhammer, 1876, “Uber Fortplanzungsgeschwindigkeiten kleiner Schwingungen in einem unbergrenzten isotropen Kreiszylinder”, *J. Reine Angew. Math.* Vol. 81, 324 (German).

[8] E. Woldesenbet and J. Vinson, 1997, “Effect of specimen geometry in high-strain rate testing of graphite/epoxy composites”, *Collection of Technical Papers AIAA/ASME/ASCE/AHS/ASC Structures, Structural Dynamics,* v2, pp. 927-934

[9] E. Davies and S. Hunter, 1963, "The dynamic compression testing of solids by the method of the split Hopkinson pressure bar", *Journal of the Mechanics and Physics of Solids*, Volume 11, Issue 3, pp. 155-179.

[10] C. Frantz, P. Follansbee, and T. Wright 1984, "Experimental Techniques with the Hopkinson Pressure Bar", *High Energy Fabrication, The American Society of Mechanical Engineers*, New York, pp. 229-236.

[11] C. Chree, 1889, "The equations of an isotropic elastic solid in polar and cylindrical coordinates, their solution and applications", *Trans Cambridge Philos. Soc*, 14, pp. 251–369.

[12] A. Love, 1944, "A treatise on the mathematical theory of elasticity", *Dover Publications*, New York, pp. 428

[13] D. Bancroft, 1941, "The velocity of Longitudinal Waves in Cylindrical Bars", *Physical Review*, Vol.59, No.59, pp. 588-593

[14] D. Gong and X. Wu, 1996, "An empirical method for correcting dispersion in pressure bar measurements of impact stresses", *Measurement Science and Technology,* V.7 No.9, pp. 1227-1232

[15] D. Gorham and X. Wu, 1997, "An empirical method of dispersion correction in the compressive Hopkinson bar test", *Journal de Physique IV Colloque*, V.7, pp. C3-223-228.

[16] J. Yi, M. Boyce, G. Lee and E. Balizer, 2006, "Large deformation rate-dependent stress–strain behavior of polyurea and polyurethanes", *Polymer*, Vol. 47, Issue 1, pp. 319-329.

[17] J. Shim and D. Mohr, 2009, "Using split Hopkinson pressure bars to perform large strain compression tests on polyurea at low, intermediate and high strain rates", *International Journal of Impact Engg*, Vol. 36, Issue 9, pp. 1116-1127.

[18] T. Johnson, S. Sarva, and S. Socrate, 2010, "Comparison of Low Impedance Split-Hopkinson Pressure Bar Techniques in the Characterization of Polyurea", *Experimental Mechanics*, Vol. 50, Issue 7, pp. 931-940.

[19] N. Naik, P. Shankar, K. Venkateswara, G. Ravikumar, J. Pothnis, and H. Arya, 2011, "High strain rate mechanical behavior of epoxy under compressive loading: Experimental and modeling studies", *Materials Science and Engineering A*, Vol 528, Issue 3, pp. 846–854.

[20] B. Fu, H. Luo, F. Wang, G. Churu, K.T. Chu, J.C. Hanan, C. Sotiriou-Leventis, N. Leventis, and H. Lu, 2011, "High strain rate mechanical behavior of epoxy under compressive loading: Experimental and modeling studies", *Journal of Non-Crystalline Solids*, Vol 357, Issue 10, pp. 2063–2074.

[21] G. Youssef and V. Gupta, 2012, "Dynamic response of polyurea subjected to nanosecond rise-time stress waves", *Mechanics of Time Dependent Materials*, Vol. 16, Issue 3, pp. 317-328.

[22] B. Yang, L. Chunmei, and G. Huang, 2016, "A Hyper-Viscoelastic Constitutive Model for Polyurea under Uniaxial Compressive Loading", *Polymer*, Vol. 8, Issue 4, Article Number: 133.

[23] V. Joshi and C. Milby, 2012, "High strain rate behavior of polyuria compositions, Shock Compression of Condensed Matter", *PTS 1 and 2 Book Series: AIP Conference Proceedings*, Vol. 1426, edited by: Elert, ML; Buttler, WT; Borg, JP.

[24] F. Barbosa and M. Farage, 2008, "A finite element model for sandwich viscoelastic beams: Experimental and numerical assessment", *Journal of Sound and Vibration*, Vol. 317, pp. 91-111.

[25] D. Mohotti, T. Ngo, P. Mendis, and S. Raman, 2013, "Polyurea coated composite aluminum plates subjected to high velocity projectile impact", *Materials and Design*, Vol. 52, pp. 1-16.

[26] D. Mohotti, T. Ngo, S. Raman, M. Ali, and P. Mendis, 2014, "Plastic deformation of polyurea coated composite aluminum plates subjected to low velocity impact", *Materials and Design,* Vol. 56, pp. 696-713.

[27] D. Mohotti, M. Ali, T. Ngo, J. Lu, and P. Mendis, 2014, "Strain rate dependent constitutive model for predicting the material behavior of polyurea under high strain rate tensile loading", *Materials and Design*, Vol. 53, pp. 830-837.

[28] M. Amini, J. Simon, and S. Nemat-Nasser, 2010, "Numerical modeling of effect of polyurea on response of steel plates to impulsive loads in direct pressure-pulse experiments", *Mechanics of Materials*, Vol. 42, Issue 6, pp. 615-627.

[29] S. Tekalur, A. Shukla, and K. Shivakumar, 2008, "Blast resistance of polyurea based layered composite materials", *Composite Structures*, Vol.84, pp. 271-281.

[30] J. Qiao, A. Amirkhizi, K. Schaaf, S. Nemat-Nasser, and G. Wu, 2011, "Dynamic mechanical and ultrasonic properties of polyuria", *Mechanics of Materials*, Vol. 43, pp. 598-607.

[31] M. Nouh, O. Aldraihem, and A. Baz, 2015, "Wave propagation in metamaterial plates with periodic local resonances", *Journal of the Sound and Vibrations*, Vol. 341, pp. 53-73.

[32] H. Al Supie, 2016, "Vibration of Periodic Drill strings with Local Sources of Resonance", *Ph.D. Dissertation,* University of Maryland.